Simulated Absorption Lines in the Circum-Galactic Medium

Bernhard Röttgers

Garching 2017

Simulated Absorption Lines in the Circum-Galactic Medium

Bernhard Röttgers

Dissertation
an der Fakultät für Physik
der Ludwig–Maximilians–Universität
München

vorgelegt von
Bernhard Röttgers
aus Fürth

München, den 15.5.2017

Erstgutachter: Prof. Dr. Simon D. M. White
Zweitgutachter: Dr. Klaus Dolag
Tag der mündlichen Prüfung: 3. Juli 2017

Contents

List of Figures

List of Tables

Zusammenfassung / Abstract

Neuere Untersuchung der Absorptionslinien von Gas in the Halos von nahen Spiralgalaxien haben die allgegenwärtige Existenz des circum-galaktischen Mediums (CGM) offenbart. Ich nutze 12 kosmologische Zoom-Simulationen von Spiralgalaxien um den physikalischen Ursprung der Absorptionslinien im CGM zu prüfen. Die Simulationen wurden mit einem mehrphasigem Smoothed Particle Hydrodynamics (SPH) Code mit zwei-phasigem Feedback durchgeführt, der auf GADGET basiert und Sternentstehung, Metallanreicherungen und stellares Feedback berücksichtigt. Ich entwickelte PYGAD, ein neues, Python-basiertes, modulares Paket, das ein zweckmäßiges Framework und eine Vielzahl von Analysemodulen für die SPH Galaxiensimulationen stellt. Unter diesen findet sich eins für das Übertragen von SPH Größen auf räumliche Gitter and eines zur Generierung von künstlichen Absorptionsspektren aus SPH Simulationen, welche im Detail diskutiert werden. Im Allgemeinen zeigen die simulierten Galaxien radial abfallende Ly-α Äquivalentbreiten (ÄBs) von $\sim$1.1 Å bei 50 kpc bis 0.5 Å bei $\sim$250 kpc mit großer Streuung in akzeptabel Übereinstimmung mit Beobachtungen. Die simulierten Ly-α ÄBs korrelieren typischerweise nicht gut mit H I Säulendichten im CGM, da die Linien oft saturiert sind und die H I Geschwindigkeits-Struktur entlang der Sichtlinie die Absorptionslinie signifikant verbreitert. Nur Galaxien mit ungestörtem CGM zeigen eine gute Korrelation zwischen der H I Säulendichten und der ÄB Verteilungen. Wenn H I überwiegend in der Scheibenebene akkretiert wird, zeigen die Ly-α ÄBs eine Abhängigkeit vom azimutalen Winkel, die in stärker gestörten Systemen, die eine Wechselwirkung unterliegen, ausgelöscht ist. Die ÄB Profile für Mg II and O VI stimmen gut mit Beobachtungen überein. Insbesondere O VI ist besser reproduziert als in allen vorherigen Simulationen. C IV and O VI Absorptionsmerkmale werden bis zu großen Radien beobachtet und die räumliche und Geschwindigkeits-Verteilung ist deutlich verschieden zu der von H I. Ich stelle fest, dass O VI dem abströmenden heißen Gas folgt, wohingegen Mg II and H I gut dem anströmenden kalten ($\sim 10^4$ K und weniger) Gas folgt. Hier können die Messungen der niedrigeren Ionen dazu verwendet werden die intrinsische Struktur der saturierten H I Linien offenzulegen.

Modern absorption lines surveys of gas in the halos of nearby spiral galaxies have revealed the ubiquitous existence of a metal enriched ionised circum-galactic medium (CGM). I use 12 cosmological zoom simulations of spiral galaxies to fathom the physical origin of the absorption lines in the CGM. The simulations are performed with a multiphase smoothed particle hydrodynamics (SPH) code with two-phase feedback based on GADGET including star formation, metal enrichment, metal cooling, and stellar feedback. I have developed PYGAD, a new Python based modular package, that provides a convenient framework for analysing SPH galaxy simulations and a variety of analysis modules. Among them are one for binning SPH quantities onto spatial grids and one for generating mock absorption spectra from SPH simulations, which are discussed in detail. In general, the simulated galaxies show radially declining Ly-α equivalent widths (EWs) from $\sim$1.1 Å at 50 kpc to 0.5 Å at $\sim$250 kpc with large scatter in reasonable agreement with observations. The simulated Ly-α EWs typically do not correlate well with H I column densities in the CGM as the lines are often saturated and the H I velocity structure along the l.o.s. broadens the lines significantly. Only galaxies with undisturbed CGM show good correlations between the H I column densities and EW distribution. With H I accretion predominantly in the disc plane, the Ly-α EWs show a dependence with the azimuthal angle, which is erased for more disturbed systems undergoing some interaction. The EW profiles for Mg II and O VI are in good agreement with observations. In particular, O VI is better reproduced than in any previous simulation. C IV and O VI absorption features are observed to large radii and the spatial and velocity distribution is clearly different to H I. I find that O VI traces the outflowing hot gas, whereas Mg II and H I trace well the inflowing cold ($\sim 10^4$ K and less) gas. Here, the measurements of low ions can used to reveal the intrinsic structure of saturated H I lines.

Chapter 1

Introduction

1.1 Preamble

The universe houses a wealth of astonishing things. This is not confined by the myriads of wonders of our planet Earth but extends well beyond into outer space: solar flares, supernovae, planetary nebulae and supernova (SN) remnants—the Crab Nebula probably being the most famous—, giant molecular clouds such as the Orion nebula, and more. It is often claimed that the endeavours to understand its nature would destroy its beauty. I, however, go along with Richard Feynman who pointed out that mathematical beauty of physics actually adds an entire new dimension of new wonders to what the human eye can see.

And indeed did physics not only allow technology to evolve to the point where mankind was able to build huge, precise telescopes and shoot them hundreds of kilometres off Earth without destroying them—in fact we are even able to repair them there—and then provide us with such astonishing pictures as the Hubble Space Telescope (HST) does. Physics also can put these things into perspective: it revealed how powerful the explosion of star actually is, that it can outshine entire galaxies that are build out of many billions (10^9) and trillions (10^{12}) such stars, how the debris of a stars violent death is the birth place of new stars. It found the still not fully understood monsters of super-massive black holes (SMBH) in the centres of galaxies that can even outshine the powerful SNe by orders of magnitudes, when they swallow large amounts of gas (and stars) and turn into 'active galactic nuclei' (AGNs). Physics gives beautiful mathematical models in form of Albert Einstein's General Relativity (GR) that explains by the hard to grasp curvatures of space-time how that can happen. This theory also let us reach back to the Big Bang, the birth not only of the universe but also space and time itself.

GR also laid the foundations to understand cosmological structure formation. Despite the universe being astonishingly uniform on very large scales, tiny quantum fluctuations, ripples in space-time, gave rise to basically all of today's structure. The largest structures are galaxy (super)clusters followed by the second largest structure, the galaxies themselves. These resemble some of the above mentioned astonishing wonders of nature that delight expert as layman alike. And despite decades of research and the condition that we most likely know all relevant processes that are relevant for the formation of galaxies, we still only have only a basic understanding of how they form and for some processes we still do not know whether they are actually are important or not (cosmic rays and its effect on galactic outflows is one of them).

This work has these enormous beauties of galaxies as their central objects of interest. I want to add my humble part to understand their laws of formation and their nature. It is clear that I can only add small parts to the this big puzzle of the many different fields of physics that take part in this cosmic dance. However, the diversity of this problem is what makes it so intriguing and challenging.

1.2 Recognising Galaxies as Such

The word 'galaxy' derives from the greek word 'galaxias' ($\gamma\alpha\lambda\alpha\xi\acute{\iota}\alpha\varsigma$), which means 'milky', a reference to the Milky Way. Early on it was speculated that this diffuse band in the sky might consist out of many distance stars. The first one might be the Greek philosopher Democritus (450 - 370 BC), followed by a few others. For the lack of proof, however, most thought it was nebulous until about 2000 years later. It was in 1610, when Galileo Galilei pointed one of the first telescopes to the milky band and actually discovered that it is consists out of many individual stars (Galilei, 1610).

At this point it was not yet known that the our beautiful Galaxy is just one out of many. Other galaxies can be seen by the naked eye. The most easily seen ones are the Large Magellanic Cloud (LMC) and the Andromeda Galaxy, which are documented to be seen in the tenth century by Abd al-Rahman al-Sufi (see Kepple, 1998). They were not yet identified as distinct galaxies, though. A good century later, Thomas Wright (1750) speculated that these and other nebulae might be separate galaxies. However, it took another 150 years until the first evidence was provided that spiral nebulae are indeed far outside our own Galaxy and are to fast rotating to be small object in the Milky Way.

The recognition of the nebulae as galaxies started with Vesto Slipher, when he made spectroscopic studies of the brightest spirals and found that they have too large Doppler shifts to be small object in the Milky Way and most are moving rapidly away

Figure 1.1: A full sky panoramic view of the Milky Way. The Large Magellanic Cloud (LMC) and the Small Magellanic Cloud (SMC) are seen in the lower right of the image and they are visible to the unaided eye in the southern hemisphere. A bit below the Milky Way and about a fifth of the width from the left, the Andromeda Galaxy is visible as a small bright spot (cf. Fig. 1.2).
Image credit: ESO/S. Brunier.
Image URL: `https://www.eso.org/public/images/eso0932a/`

from us (what later will become known as the Hubble flow) (Slipher, 1913, 1915). A few years later, Heber Curtis observed the nova (Latin for 'new', referring to a new star) 'S Andromedae' and noticed that it and those in other nebulae were, on average, 10 magnitudes fainter than those that were observed elsewhere, in our own Galaxy. From this data he could estimate the distance of Andromeda to be about 150 kpc (Curtis, 1988)—about a factor of 5 too small, but in the right order of magnitude. These observations culminated in the so-called Great Debate between Harlow Shapley and Heber Curtis on 26 April 1920 about the size of the universe and the nature of the spiral nebulae, i.e. whether they are indeed separate galaxies or not.

Ernst Öpik (1922) added another distance determination of the Andromeda Nebula to the one from Heber Curtis supporting the theory that it is a separate galaxy. Edwin Hubble then was able to resolve the outer parts of some spiral nebulae into collections of individual stars with a new, 2.5 meter large telescope on Mt. Wilson. This enabled him to make distance measures using Cepheids, a type of variable stars,

and, hence, determine the distance of these nebulae (Hubble, 1926, 1929a,b). They are too far away to be part of the Milky Way. It was finally settled that not only we live in a huge conglomeration of stars, called our Galaxy, the Milky Way, but that there are many of these galaxies in the universe.

It was also the same work by (Hubble, 1929a) that found the linear relation of galaxies' distance to its velocity. The proportionality constant of that relation, the Hubble constant (at redshift zero) H_0 as it will be called later, was measured to be about 500 km/s/Mpc. Today it is measured more precisely to roughly a tenth of this first value (67.74 ± 0.46 km/s/Mpc by the Planck Collaboration et al., 2016), but it was this early measure (together with Einstein's theory of General Relativity) that laid the foundation to modern cosmology.

So, despite that our own Galaxy as well as some others such as the Andromeda Galaxy and the LMC has been seen from mankind thousands of years ago, the scientific establishment of the concept of galaxies is not even 100 years old. In this sense, the science of galaxies and, hence, also about their formation is a young science. We still are at the beginning of a full understanding of galaxy formation.

1.3 Defining Galaxies

In the early days of galaxy research there was not much necessity to precisely define what a galaxy is. The famous catalogue of Charles Messier only contains 110 diffuse or nebulous objects. Not all of them are galaxies, some are planetary nebulae, supernova remnants, or other nebulae within the Milky Way, some are stellar clusters (also within the Milky Way), and just some are actually galaxies. These 'island universes', as galaxies also were called in the early days, classified themselves as (1) being outside the Milky Way and (2) by their milky appearance, in contrast to 'clusters' of stars in the Milky Way that appear much more grainy due their resolved individual stars.

As technology proceeded and with the onset of automated surveys the number of known galaxies and stellar clusters exploded and today we know millions of galaxies. Stellar clusters were also found outside the Milky Way in its halo as well as around other galaxies, requiring a more precise definition. Galaxies happen to exist at various sizes, but nevertheless at first astrophysicists typically classified stellar clusters and galaxies—both gravitationally bound systems of stars—simply by their size. Galaxies have typical sizes of a few hundreds of parsecs to tens of kilo-parsecs and star clusters have typical sizes of only several parsecs. However, there are also objects found in the intermediate range of sizes. There are so-called dwarf galaxies that can be smaller (in terms of mass, luminosity, and spatial extent) than some large globular clusters.

Up to today no official formal definition of a galaxy exists. However, consensus is that (the still not directly detected) dark matter draws the line between the two categories. Simply speaking, galaxies have dynamically significant amounts of dark matter—in fact, their rotation curves are historically one of the first indication for the existence of dark matter—and globular clusters do not. Or more formally with the words of Willman & Strader (2012): *"A galaxy is a gravitationally bound collection of stars whose properties cannot be explained by a combination of baryons and Newton's laws of gravity."* This definition tries not to name the widely accepted but not directly proven concept of dark matter. Even this definition is not perfect as, for instance, close encounters in globular clusters would require General Relativity to be modelled accurately, however, globular clusters are not considered galaxies just because of a close star-star encounter.

1.4 Galaxy Properties

1.4.1 Classifying Galaxies and the Hubble Sequence

The definition that galaxies are gravitationally bound collections of stars that contain a dynamically significant fraction of dark matter is about as close we can get. A reason for the difficulty to arrive at a working definition is also the large variety in which galaxies exist. A very early classification scheme from Hubble (1926), developed at the time when it became clear that some of the nebulae seen are 'island universes' / galaxies, is still in use today. It is called the Hubble sequence or Hubble tuning fork, shown in Fig. 1.3.

The Hubble sequence distinguishes a few broad classes based on the optical morphology of the galaxies: elliptical (E), lenticular (S0), and spiral (S) galaxies. Galaxies that do not fit into any of these three classes are named irregular (Irr). The spirals (and lenticular galaxies) are further divided into those that have a stellar 'bar' in their center (SB) and those without one (just an S, no B). The ellipticals and spirals are finally subdivided more fine-grained. Ellipticals are denoted with a capital E followed by an integer $n = [10 \times e]$ measuring their tenfold ellipticity $e = 1 - a/b$, where a and b are the lengths of the major and minor axis, respectively. As observationally the flattest systems have about $e = 0.7$, there are eight classes: E0 through E7. The spiral galaxies are subdivided into classes Sa through Sc (and some newer classifications also use Sd) ranging from tightly wound smooth spiral arms and a large, bright central bulge to loosely wound, fragmentary arms and a small, faint or even absent bulge.

Although the classification by Hubble is purely based on optical appearance of

the projected galaxies and is somewhat subjective—bugle size and the appearance of the arms, for instance, do not always go conjointly—, it is still widely used. That probably is because many other physical properties correlate well with the sequence. For instance, the gas fraction increases from left (E0) to right (S(B)c/d, cf. Fig. 1.3) as well as do the galaxies change from red to blue.

Not all galaxies fit well into the Hubble tuning fork or are put into the somewhat broad class of irregulars (which was actually not part of Edwin Hubble's original classification): there are galaxies that a far from dynamical equilibrium such as galaxies that undergoing a merger with others such as the peculiar Antennae galaxies (NGC 4038 and NGC 4039); some discy galaxies have rings (such as 'Hoag's Object') or consist of solely a ring (e.g. Arp 147 / IC 298); and some are ellipticals but exhibit prominent gaseous discs (such as Centaurus A / NGC 5128) and/or 'jets' (M87) that are typically not seen in the optical spectrum, though. This is why there are not only alternative classification schemes, naming the one due to de Vaucouleurs (1974) here, but galaxies are also often classified by some other properties such as whether they are mergers, show active galactic nuclei (AGNs), spectral features (e.g. Lyman-break galaxies), or the amount of recent star formation (starburst galaxies).

Still, the Hubble sequence is the most widely used classification. It is often adjusted or extended, though (for a modern scheme see e.g. Cappellari, 2016). Among the most common extensions is 'cD' for the brightest cluster galaxies (BCG) with diffuse outskirts and a leading 'd' for dwarf galaxies as in 'dIrr' and 'dE' for dwarf irregulars and dwarf ellipticals, respectively, or 'dS' in the rare dwarf spirals. Dwarfs are galaxies with small absolute magnitude, i.e. about $\mathcal{M}_B \gtrsim -18$. Furthermore, there is also the class of dwarf spheroidals (dSph) for which no clear distinction to dwarf ellipticals exists, but dSph's are typically more round and have even lower luminosity ($\mathcal{M}_B \gtrsim -14$) than the dwarf ellipticals.

1.4.2 Galaxy Statistics

Even though the dwarfs are, as their name suggests, dim and small galaxies, they still outnumber other galaxy types by about an order of magnitude. The relative number densities of the various types, normalised to that of spiral galaxies, are given in Tab. 1.1 as taken from Mo et al. (2010). As they are so numerous and often merge with each other or are eaten by bigger galaxies, they probably play a relevant role in galaxy formation.

As a function of the galaxies' luminosities—a quantity that is directly observable in contrast to their mass—on can describe the number density of galaxies well by the Schechter (1976) luminosity function (the form of which can theoretically be well

Galaxy type	Rel. number density
Spirals	1
Lenticulars	0.1
Ellipticals	0.2
Dwarfs	10
Peculiar	0.05
Starbursts	0.1

Table 1.1: Relative number densities of galaxies in the local universe (i.e. today), an excerpt from Mo et al. (2010).

motivated: see Press & Schechter, 1974):

$$\phi(L) = \frac{\mathrm{d}n(L)}{\mathrm{d}L} = \frac{\phi^*}{L^*}\left(\frac{L}{L^*}\right)^{\alpha} \exp\left(-\frac{L}{L^*}\right) \tag{1.1}$$

Modern observations measure values like $\alpha = -1.2$, $\phi^* = 5 \times 10^{-3}\,\mathrm{Mpc}^{-3}$, and $L^* = 3 \times 10^{11}\,L_\odot$ in B-band (e.g. Faber et al. (2007), Norberg et al. (2002)).

1.4.3 A Typical Galaxy

The median luminosity L_{med} for galaxies is $L_{\mathrm{med}} \simeq 0.48\,L^* \approx 10^{11}\,L_\odot$. Here, the median luminosity is defined as the luminosity for which half of the galaxy luminosity density is from galaxies brighter than L_{med} and the other half from dimmer ones (i.e. $\int_0^{L_{\mathrm{med}}} L\,\phi(L)\,\mathrm{d}L = \int_{L_{\mathrm{med}}}^{\infty} L\,\phi(L)\,\mathrm{d}L$). Although the Milky Way's mass and luminosity are not well known, this is roughly its luminosity (Karachentsev et al., 2004, Licquia & Newman, 2013). As it is also a spiral galaxy and as most stellar mass in the Universe is in spiral galaxies (cf. also Tab. 1.1), one can consider the Milky Way as a typical galaxy even though properties of galaxies vary by orders of magnitudes.

Another important properties of galaxies are, apart from their morphology, luminosity, and mass, for instance, their metallicities in the stars and the gas. These reveal hints about their age as metals were not produced in the primordial nucleosynthesis (apart from small amounts of Lithium) but in stars, which in turn then release them into the inter-stellar medium (ISM) by stellar winds and at the end of their life in planetary nebulae or super novae (SNe). The metals can also be transported further out by galactic winds (probably mostly driven by SNe, but also AGNs and maybe also by cosmic rays see e.g. Naab & Ostriker, 2016), tidal stripping, and/or ram pressure stripping. In the gas metals can reduce cooling times a lot by metal line cooling (Ferland et al., 1998, Wiersma et al., 2009).

The solar abundances are relatively precisely measured. Hence, we typically measure element abundances relative to the solar metallicity, denoted $[X] := \log 10(X/X_{\rm solar})$ for an element X, and also often speak of an overall metallicity for all elements, Z. From data from the Sloan Digital Sky Survey (SDSS) Ivezić et al. (2008) infer a metallicity of $-0.8 \lesssim [Fe/H] \lesssim -0.5$ for most stars in the Milky Way's disc component and $[Fe/H] \simeq -1.5$ with a scatter of ~ 0.3 for stars in its halo. The gas typically has higher metallicities due continuous enrichment by the stars but also varies a lot by phase and has large observational uncertainties, however, is typically measured around solar metallicity and above (see e.g. Cardelli & Federman, 1997). This is also where the Milky Way would be located on the so-called mass-metallicity relation of galaxies, that correlates star-forming galaxy stellar masses with their gas phase metallicity (see e.g. Tremonti et al., 2004).

1.5 Brief Overview of Galaxy Formation

We control the stage on which it is happening relatively well: the large scale structure formation is thought to be understood in the framework of Lambda cold dark matter (ΛCDM) cosmologies. After the Big Band about 13.8 billion years ago the universe cooled by expansion from an almost uniform state. Very small perturbation in the distribution of matter, that can be measured in the cosmic microwave background (CMB) to high precision nowadays (e.g. by the Nine-year Wilkinson Microwave Anisotropy Probe (WMAP9) as presented in Bennett et al., 2013 or by the Planck mission Planck Collaboration et al., 2016) and are thought to be quantum fluctuations 'frozen' during a short inflationary period right after the Big Bang, were amplified by gravity over time and formed halos.

As $\sim$84% of all the matter in the universe is dark matter, which does not interact electro-magnetically (hence, called dark) but gravitationally in the ΛCDM models, and the highly nonlinear effects of baryon physics have little effect on large scales, we can derive large scale structure well when only considering gravity and the expansion of the universe (covered by the Friedman (1999) equations). The aforementioned perturbations in the density field do not only collapse into many bound structures, but these also merge with each other over time. The merging starts at the smallest scales first and the progressively extends to larger structures. This picture is known as the 'hierarchical structure formation' developed (by e.g. Peebles, 1980).

On top of the 'cosmic web' of density structures lives the baryonic matter, which is not able to change the very large-scale structure much. However, for galaxies the baryon physics is relevant and in fact necessary to arrive at the typical scales, which was recognised early on by White & Rees (1978) and Fall & Efstathiou (1980). The

baryons, in contrast to dark matter, can cool and condense even further than the dark matter. If they conserve their angular momentum whilst cooling and collapsing, they must end in up in flat, rotating discs. In these dense structures, the gas can fragment and collapse to even higher densities until the collapse is stopped because nuclear fusion is ignited—stars are born and we have build a galaxy. These cannot only grow by monolithic collapse but also merge together with the dark matter halos, that still dominate the gravity as there is about five times as much as baryonic matter. Hence, the galaxies also take part in the hierarchical structure formation.

The problem with perfect conservation of the angular momentum, however, is that the discs then rotate too fast and and modelled discs also had much smaller scale lengths than what is observed. This problem became known as the 'angular momentum catastrophe'. It was soon seen that this simple picture would—as successful as it is—also result in an overproduction of stars and too concentrated galaxies: a long standing problem for which the term 'over-cooling problem' was coined. Gas cooling by its own is too efficient in the sense that it would produce too many stars, if there would not be some sort of feedback which can inhibit star formation (as suggested by e.g. Dekel & Silk (1986), Larson (1974)). The dark matter halo mass function rises steeply in form an exponential, $\propto M^{-1.9}$, towards small mass objects (Reed et al., 2007). If a constant fraction of the baryons would be locked into stars, e.g. 17% of the mass the dark matter, i.e. all baryons, the luminosity function of galaxies would not look like the Schechter (1976) function as presented above. Although that measures luminosities, the mass-to-light ratios can, by far, not vary enough to resolve the tension.

It is widely believed, and also shown with some success that stellar feedback from SNe plays a main role in suppressing the star formation in light halos and for the more massive ones (above $\sim 10^{11}\,M_\odot$ in stellar mass) feedback from AGNs enters the scene (see e.g.Croton et al., 2006). Over the last years, large simulations of cosmological periodic boxes could finally recreate the stellar mass function from $10^8 - 10^9\,M_\odot$ to $10^{12} - 10^{13}\,M_\odot$ reasonably well (e.g. Schaye et al., 2015, Vogelsberger et al., 2014) by implementation of effective SNe feedback and AGN feedback (see e.g. Naab & Ostriker (2016), Somerville & Davé (2015)). One noteworthy example, that does not include AGNs explicitly but an empirical heating model without specifying the heating source, is that by Davé et al. (2013, 2016). They, however, do not deny the role of AGNs, but name them as a likely candidate for the physical source.

It is not only the mass functions that caused huge problems, but also the galaxy morphologies. In particular, it was for long hard to generate 'realistically' looking spiral galaxies in cosmological galaxy formation simulations with physical models. The galaxy did not grow to the observed sizes and lost significant amounts of angular

momentum from gas to dark matter. This problem became known as the 'angular momentum catastrophe' (see e.g. Navarro & Benz, 1991, Navarro et al., 1995, Weil et al., 1998). It has not been until a few years ago that simulations could successfully overcome the problem and generate reasonable discs (e.g. Agertz et al., 2011, Guedes et al., 2011, Piontek & Steinmetz, 2011, Scannapieco et al., 2009) by strong enough feedback such that the gas did not form stars early on, but could be expelled several times to gain more angular momentum by cosmic torques (Übler et al., 2014).

This repetitive ejection of gas by stellar or AGN feedback in form of galactic winds or galactic 'fountains' into the halo and its later re-accretion onto the galaxy is part of the so-called *baryon cycle* (see Fig. 1.4). (In-between these ejections and re-accretions the gas can possibly form stars that eventually expel their envelope as a planetary nebula or explode as a SN, if heavy enough.) This baryon cycle is understood to be a main source for the gas that builds the circum-galactic medium (CGM), defined as the medium associated with a galaxy, but not part of the galaxy itself, i.e. not in form of stars or the ISM, and in contrast to the inter-galactic medium (IGM) that is just in-between the galaxies without being associated with any galaxy.

The Cosmic Origin Spectrograph (COS), installed onboard the Hubble Space Telescope (HST) in 2009, provided evidence on the idea that the CGM is also largely fed by galactic winds as it has not only shown that the CGM is ubiquitous and can hold more baryons than the galaxy stars and gas (Werk et al., 2014), but also that it has high metallicities (e.g. Prochaska et al., 2017).

1.6 What is Missing? And Where to Go?

Despite the progress outlined there are still big challenges to tackle in galaxy formation (for a recent review see e.g. Naab & Ostriker, 2016). Much of the progress is built on simulations from which one can match many of the observation reasonably well. However, they often employ vastly different models and implications for the physics happening beyond the resolution scale, referred to as 'sub-grid models'. It is questionable how much we can learn from them, if the actual mechanism going in vary so much from model to model. Furthermore, the models can reproduce galaxy statistics, however, fail to generate the same results from the same initial conditions as shown by Scannapieco et al. (2012).

In principle there are several ways to improve on this situation: a) taking different paths than simulations to understand galaxy formation, b) improve the building stones (like stellar models) individually before implementing them into big simulations, or c) match observation more precisely and/or additional quantities. We should take all the paths at the same time, but here we concentrate on improving the sim-

ulations that have proven so powerful by option c). As observations themselves are often not well constrained, the most promising way is to match more quantities at the same time. If galaxy formation is not an emergent phenomenon, we should be able to exclude some of the present-day models.

We need to pin down the mechanism of the different kinds of feedback that regulate galaxy formation on many different levels: heating the ISM and driving galactic outflows; by this preventing star-formation and enriching the CGM with metals that in turn can accelerate the cooling times therein; AGN driven heating and jets; and, finally, we still do not know the quantitative role of magnetic fields and cosmic rays.

This thesis aims to add a small piece to the large puzzle by improving our understanding of the nature of CGM: how it is shaped by galactic outflows, how we can identify the in- and outflows, and what we can learn by absorption observations, which are virtually the only source of direct information of the CGM.

Figure 1.2: A photograph of the Andromeda Galaxy or M31, the galaxy with the biggest apparent size in the night sky. This image combines almost 5 hours of exposure in different channels of the visible spectrum, including 2 hours for the H_α line, with an amateur telescope. The galaxy can still be seen by the naked eye in good conditions as a faint diffuse spot in the Andromeda constellation, though. Above M31, right at the edge of the disc its satellite galaxy M32 is located. Below the Andromeda galaxy, one can see M110, another satellite galaxy.
Image credit: Adam Evans.
Image URL: `https://www.flickr.com/photos/astroporn/4999978603/`.

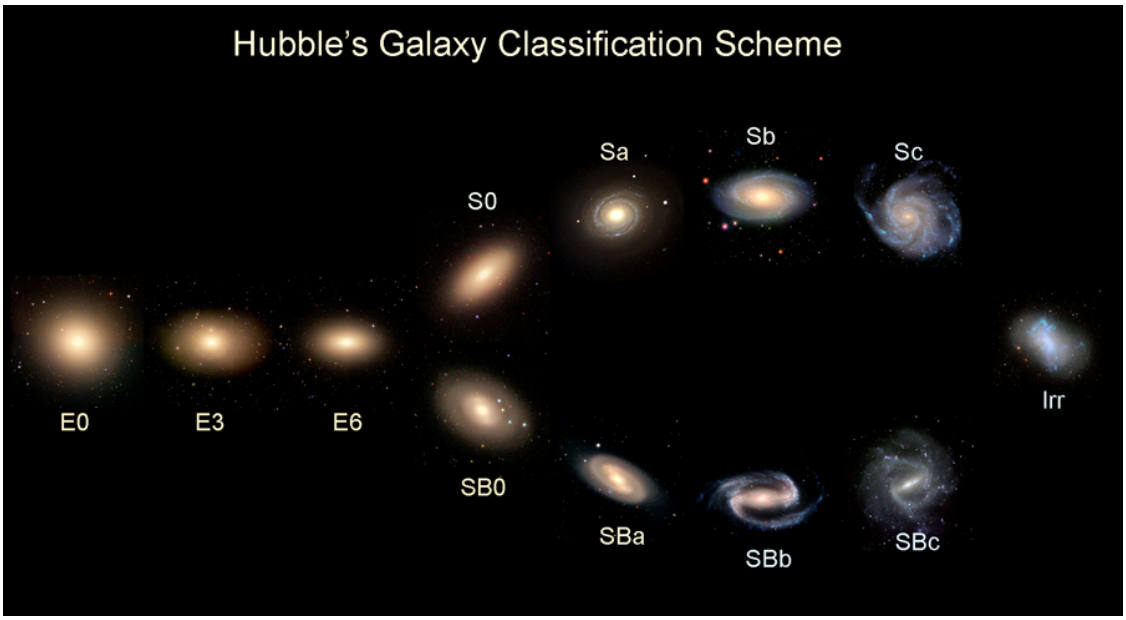

Figure 1.3: The Hubble Sequence or Hubble Tuning Fork with real galaxies as examples for the classes.
Image credit: Galaxy Zoo project.
Image URL: `https://blog.galaxyzoo.org/2010/05/12/types-of-galaxies/`.

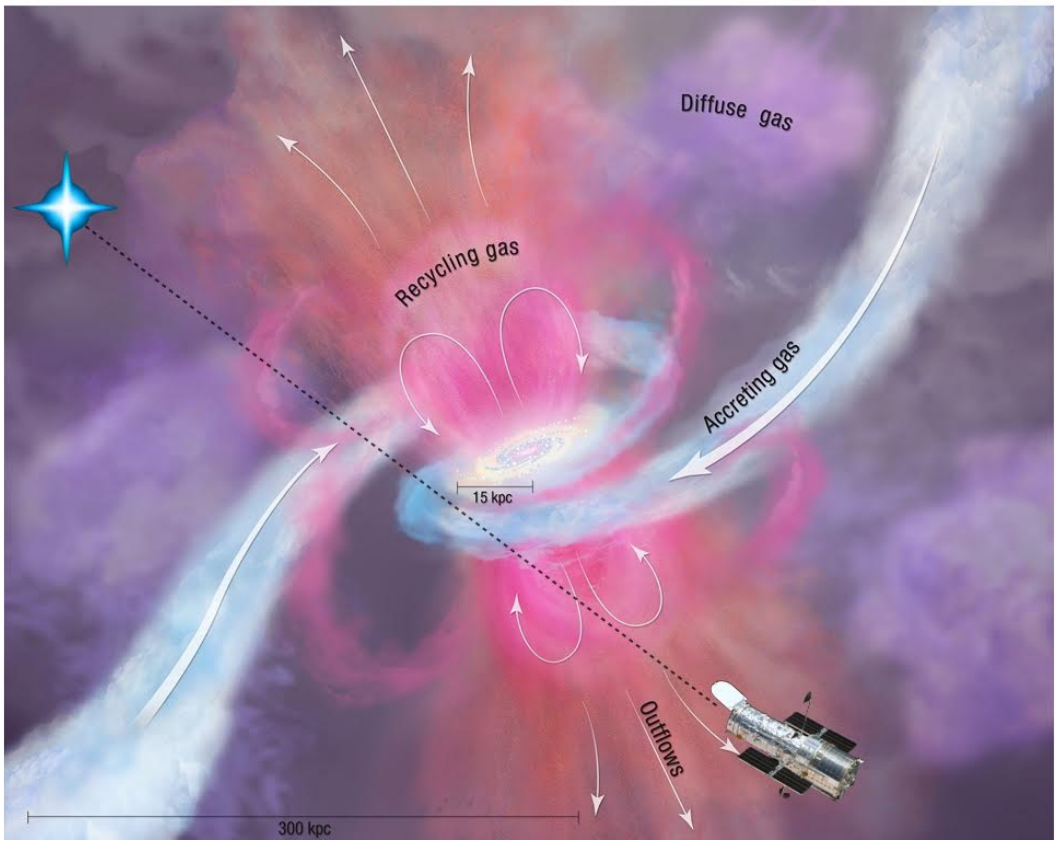

Figure 1.4: A schematic depiction of the accretion of gas onto a spiral galaxy, the ejection of gas by feedback into the circum-galactic medium (CGM) and the eventual re-accretion of the gas. The blue-white star on the left actually represents a QSO (i.e. a galaxy) which light is partly absorbed by the gas in the CGM along its path (dotted line) towards the Cosmic Origins Spectrograph (COS) onboard the Hubble Space Telescope (HST).
Image credit: Space Telescope Science Institute (by Anne Field).

Chapter 2

Metals and Absorption in the Halo

The CGM can be interpreted as a reservoir for matter from which galaxies can grow and into which all the galactic outflows go to. In any case, it contains more baryonic mass than the galaxy in form of stars and ISM gas (see Fig. 2.1). It is also believed to contain most of the baryons at all epochs (see e.g. Davé et al., 2001). Hence, it is of great interest not only to understand the complex processes in the galaxy itself but also the medium its growth is fuelled by and that takes all the expelled gas. The problem with the CGM is that it is very sparse and, hence, difficult to observe. One way we can obtain detailed information is by absorption line observations and even these are often beyond the detection limit of modern telescopes.

When there is a bright source like a quasar (QSO) in the background and we know its spectral emission, we measure the absorption of the intervening material. Because of the Hubble flow spatially distinct objects have different redshifts and can thus be distinguished in the absorption spectrum. Line transitions are not only the strongest absorption features but they also depend on several physical properties of the intervening object: column density, temperature, ionisation state, and velocity structure. This way we can learn a lot about the distribution and physical state of the CGM when absorbing light from a QSO.

Interestingly, we need to observe the CGM from other galaxies, since the CGM of our Galaxy is hard to observe as it is 'half-hidden' due to its velocity structure that is partly very similar to that of the ISM (Zheng et al., 2015).

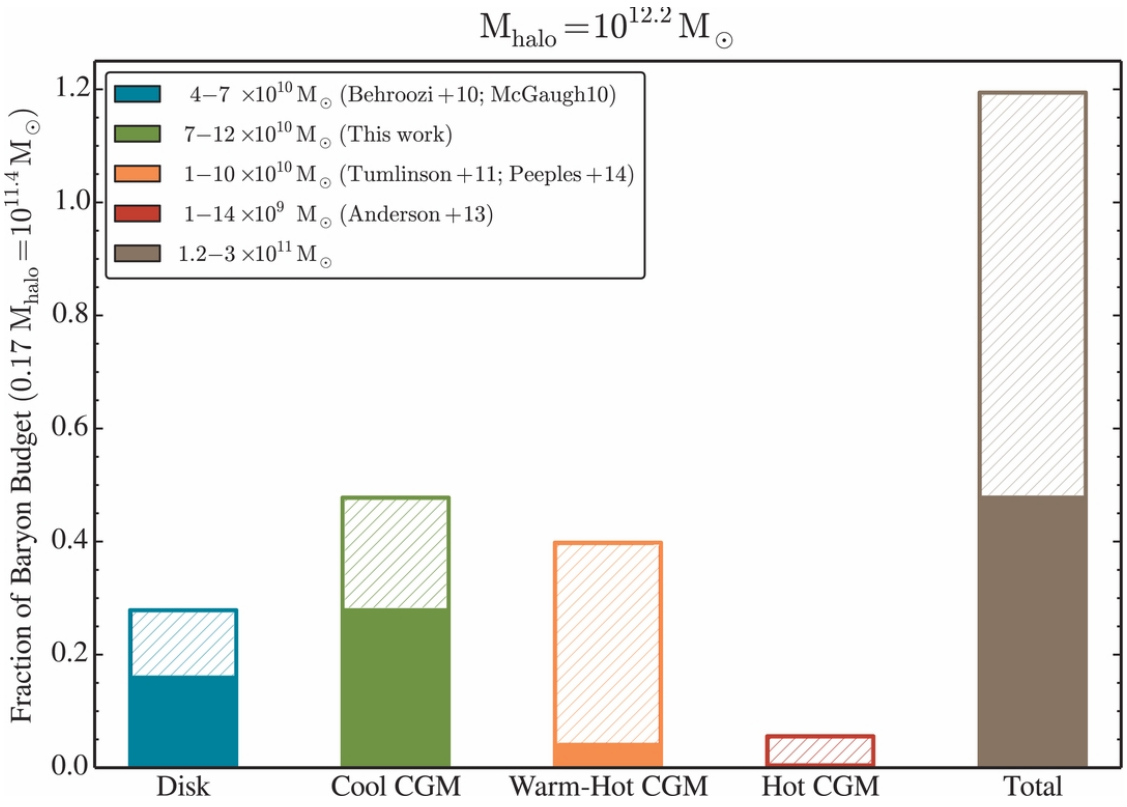

Figure 2.1: This figure from Werk et al. (2014) show the baryon mass budget an average $1.6 \times 10^{12}\, M_\odot$ halo with a L^* galaxy. Most of the mass is found to be in the CGM, most in the cool ($10^4\,\mathrm{K} \lesssim T \lesssim 10^5\,\mathrm{K}$) CGM and possible equally much in the worm-hot ($10^5\,\mathrm{K} \lesssim T \lesssim 10^7\,\mathrm{K}$, traced by O VI) CGM.

2.1 Absorption Lines

2.1.1 Lines and Ionisation Processes

The absorption lines observed by spectrograph such as the Cosmic Origins Spectrograph (COS, see e.g. Tumlinson et al., 2013) onboard the HST originate from line transitions in atoms and ions of gas between the emitting QSO and the spectrograph. When a photon with the energy of the difference of two bound states of an electron lifts this electron to the higher state, it is no longer part of the radiation that reaches the observer. In fact, the electron can and typically will fall back down to the lower energy level and emit an photon of the same wavelength; that, however, is emitted into a random direction, effectively attenuating the flux at the given wavelength.

Example spectra (as a function of relative velocity relative to the associated galaxy that causes the observed redshift) from COS are shown in Fig. 2.2.

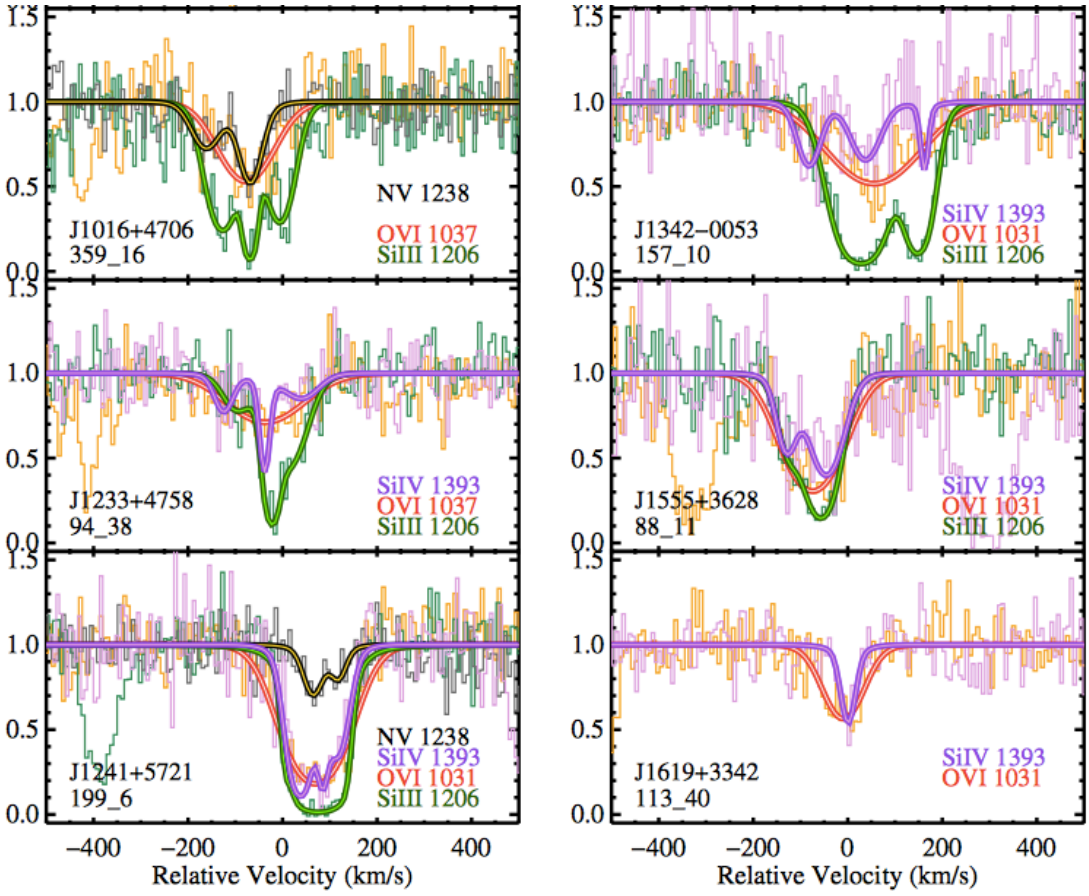

Figure 2.2: Some example absorption spectra measured by the COS as presented in Werk et al. (2016). The measured normalised spectra including the noise are plotted by the thin lines; the thick lines of the same color are the Voigt profiles fits to the spectra.

As the energy differences are unique to element and ion, therefore one can deduce the abundance of the different elements and their ionisation states. In principal there are several ways to ionise atoms; in the CGM three processes could be of significance: photoionisation, collisional ionisation, and recombination. The latter, of course, is actually the reverse process where a free electron recombines with the ion. That still changes the ionisation states, though. Collisional ionisation happens when an atom or ion collides with another particle (e.g. another atom) and the kinetic energy 'kicks'

an electron out of its bound state. The collisional ionisation is largely dependent on the temperature as the thermal motion has to provide enough energy to overcome the ionisation potential. Photoionisation, finally, is when a photon with more enough energy than the ionisation potential collides with an atom or ion and its energy is used to unbind an electron. The main radiation field of question in the CGM is the ultraviolet (UV) and X-ray background radiation in the universe, it might also be local radiation from stars or AGN, though.

2.1.2 Lyman-α Absorption

The strongest line that can be observed is the Lyman-α (Ly_α) absorption line. This is the transition of the Hydrogen atom where the electron is lifted from the $1s$ orbital to the $2p$ orbital with a (rest-frame) wavelength of 1215.67 Å. It is so strong not only because of its large oscillator strength ($f = 0.4164$) but also because most matter exists in the form of hydrogen and, therefore, H I is one of the most abundant species (atoms / ions) with absorption lines at all epochs (at $z \simeq 3$ about 5% of all matter is in the form of H I: Storrie-Lombardi et al., 1996). Together with the fact that its wavelength falls into ranges of many telescopes for most redshifts, it is a well studied line.

2.1.3 The Lyman-α Forest

It was in 1970 Roger Lynds (1971) discovered (and named) the first time the 'Lyman-α forest'. These are the multiple absorption lines at smaller wavelengths (because of the redshift from the Hubble flow) than the Ly_α emission line of the QSO (for an example spectrum see Fig. 2.3). Essentially all matter at the various redshifts has some neutral atomic hydrogen fraction and absorbs via the Ly_α. By the frequency and density of the absorbers along the line of sight (l.o.s.) it is thus possible to determine the H I density distribution and test cosmology theories after inferring the total baryonic mass budget (see e.g. Weinberg et al., 1997). At around a redshift of six the Ly_α absorption increases drastically (see e.g. Fan et al., 2006). This it associated with the end of the re-ionisation epoch. The line profiles, finally, can draw constraints on the properties of the individual absorbing objects.

2.1.4 Classification of Lyman-α Absorbers

Depending on the strength of the (sufficiently prominent) absorbers, one typically classifies them into three categories:

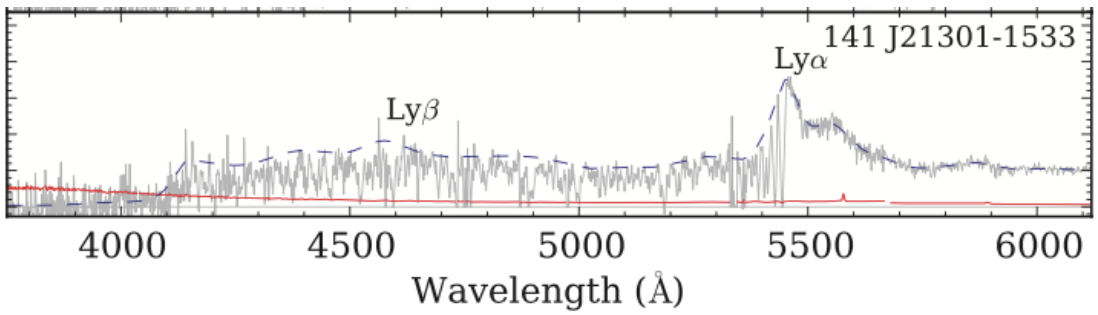

Figure 2.3: A QSO emission spectrum as presented in Crighton et al. (2011). The gray line is the spectrum itself, the blue dashed line the continuum spectrum of the QSO from which intermitting structure absorbs, and the red line is the 1σ error in the measured spectrum. Labelled are the Lyman-α and -β emission lines of the QSO, the many absorption lines left of the Lyman-α emission line are mainly Lyman-α absorption lines (amongst other hydrogen lines and metal lines) from H I at lower redshift than the QSO that build the Lyman-α forest.

- **damped Lyman-α absorption systems (DLAs):** these are somewhat arbitrarily defined as Lyman-α absorbers that have $N_{\mathrm{HI}} > 2 \times 10^{20}\,\mathrm{cm}^{-2}$. These, however, always show so-called 'damping wings', i.e. extended wings originating from the intrinsic line width (see subsection 4.4.2).

- **sub-DLAs:** defined by column densities of $10^{19}\,\mathrm{cm}^{-2} < N_{\mathrm{HI}} < 2 \times 10^{20}\,\mathrm{cm}^{-2}$. Hence, these are not quite as strong absorbers as DLAs (hence the 'sub') but already show weak damping wings.

- **Lyman-limit systems (LLSs):** absorbers that are optically thick in the Lyman limit, i.e. at rest-frame wavelengths below 912 Å, that are associated with the Ly_α line, which generally implies column densities of $N_{\mathrm{HI}} \gtrsim 10^{17}\,\mathrm{cm}^{-2}$. Generally speaking, these are stronger Ly_α absorbers that are not yet sub-DLAs.

- **Lyman-α forest:** these are all the weaker lines from absorbers with column densities and LLSs and (sub-)DLAs are typically not included when speaking of the forest of the many narrow lines blueward from the Ly_α emission line of the QSO.

Strictly speaking, all absorbers with sufficient strength to be optically thick (optical depth $\tau > 1$) in the Lyman limit are LLSs, including the DLAs and sub-DLAs.

Early on, it was postulated by Lanzetta et al. (1991), Prochaska & Wolfe (1998), Wolfe (1988), Wolfe et al. (1995) that DLAs are rotating H I discs, probably progenitors of todays spiral galaxies, as the DLA line profiles are consistent with these rotating discs. This picture was also supported by later Si II observations by, for instance, Prochaska & Wolfe (1997). However, Nulsen et al. (1998) have also shown that the lines shapes of DLAs can be explained by outflows from dwarfs as well (see also Haehnelt et al., 1998). In addition, dwarf galaxies are also thought to contribute significantly to the column densities of neutral atomic hydrogen as argued by e.g. Noterdaeme et al. (2012).

2.1.5 H I in the CGM

The upper end of the spectrum of the Lyman-α absorbers, i.e. DLAs, are associatied with (proto-)galaxies and their in- and outflows; at the other end of the spectrum, weak absorption in the Lyman-α forest ($N_{\rm HI} \lesssim 10^{14}\,{\rm cm}^{-2}$) are believed to originate from the inter-galactic medium (IGM) as they do not cluster around galaxies (Chen & Mulchaey, 2009, Prochaska et al., 2011). The remaining intermediate strength absorbers (LLSs to sub-DLAs) associated with brighter galaxies nearby, implying that these are living in their (extended) halos. A key result supporting this fact was that sight lines with smaller impact parameters to galaxies had more Ly$_\alpha$ absorption and are associated with galaxies (e.g. Lanzetta et al., 1995, Wilman et al., 2007), a relation that is typically fit with an exponential profile (Borthakur et al., 2015).

There is of evidence that H I is not uniformly distributed in the halo. Observations show that the absorbers are cloudlets with a small volume filling factor ($\sim 3-5\%$), smaller sizes (paths along the l.o.s. of $\lesssim 30\,{\rm kpc}$), and small masses ($10-10^8\,M_\odot$) (Stocke et al., 2013). There is also theoretical argument for that these small cloudlets may stay unmixed in the CGM (Schaye et al., 2007) and Stern et al. (2016) have shown that a hierarchical structure with constant $T \simeq 10^4\,{\rm K}$ (as debatable as this assumption is) explains the coverings fractions of H I; much better than the single-phase of two-phase models that are typically assumed when analysing observational data.

Although the spatial distribution is constrained as discussed above, there are many open questions about the properties of the absorbers in the halo. For instance, the relative importance of ram-pressure stripping, tidal stripping, and galactic-scale winds. Also, inflowing and outflowing gas might be correlated with the galaxy type. However, Tumlinson et al. (2013) find only a small dependence of the H I absorption on the type of the closes bright galaxy. Furthermore, Borthakur et al. (2015) find that the Ly$_\alpha$ absorption is better correlated with H I content than star-formation

rate (SFR).

It is assumed that there are some clouds associated with infall and some with outflow. As outflowing gas would presumably be more metal enriched, as it is coming from stars which produce the metals after all, one might expect a bimodality in metallicities. Hafen et al. (2016) find such a bimodality in LLSs metallicities, albeit a small one. Outflows are also typically found perpendicular to the disc plane, that should introduce an angular dependence of the absorption features. It is still unclear whether such a dependence exists, although some find a weak one such as Borthakur et al. (2015).

2.2 Metals

I already touched that metals can provide vital information on the origin and state of the absorbing gas. First, we get more information about the ionisation state of the gas when having more different ion lines. Second, H I lines are often saturated which makes it much harder to derive column densities and temperatures, but the metal lines are typically not saturated (though harder to detect). And third, one can derive metallicities. As metals are generated in stars, this provides information on the recycling and feedback processes. A complication—and at the same time advantage—is that different metal ions also trace different phases of the gas, i.e. different densities and temperatures (see e.g. Rahmati et al., 2016).

Generally, most metals are expelled far out of the galaxy with only about 25% remaining in the galaxy (Peeples et al., 2014). In simulations they are found to be expelled way beyond the virial radius (see e.g. Oppenheimer et al., 2016 for simulations or Stocke et al., 2006 for observations). In fact, metal enrichment in the CGM seems to happen from the outside inwards (see e.g. Oppenheimer et al., 2010), because at later times the potential wells get deeper and the densities larger, stopping the outflows earlier. This nature of the CGM (and IGM) enrichment results in most of the metal mass residing beyond the virial radius (for oxygen see Oppenheimer et al., 2010).

2.2.1 The WHIM and the Missing Baryon Problem

The warm-hot phase of the IGM and CGM is called the 'warm-hot intergalactic medium' (WHIM). It typically is defined as gas with temperatures of $10^5\,\mathrm{K} < T \lesssim 10^7\,\mathrm{K}$ residing outside galaxies. It seems to be a reservoir for significant amounts of metals and baryons in the universe. Newer research condenses on the idea that actually most of the baryons are to be found in the WHIM (Cen & Ostriker, 1999,

Davé et al., 2001, 2010, Wang et al., 2017, Werk et al., 2014). This would close on the so issue of the 'missing baryons', although the exact amount of mass in the WHIM is no yet well constrained, neither observationally (e.g. Werk et al., 2014) nor by simulations (e.g. Wang et al., 2017).

The just mentioned missing baryon problem is that if one does an inventory on all the observed baryons in the older universe ($z \gtrsim 2$) one ends up with just about half of what is expected from cosmology. This is probably because (warm-)hot gas is hard to trace if it is thin as it is then primarily emitting in X-ray wavelengths below the corresponding detection limits. The WHIM still can be traced by O VI (with fractions peaking at $\sim 10^{5.5}$ K) (e.g. Danforth & Shull, 2008), though some (Oppenheimer & Davé, 2009, Prochaska et al., 2011) claim it is not a good tracer (cf. also Fig 2.4). In this context, it is also interesting to note that observations seem to underestimate the cosmic ion abundances (Oppenheimer et al., 2012, Suresh et al., 2015).

2.2.2 Metal Line Absorption Characteristics

Due to cosmic abundances, line strengths, ionisation potentials, and detection limitations the ions that are most often detected, next to H I, are Mg II, C IV, and O VI. These ions tend to trace very different gas phases (cf. Fig 2.4 and e.g. Rahmati et al., 2016). Not only that the metals naturally trace more metal rich gas (than H I) but the different ionisation states require different ionisation energies and, hence, temperatures, densities and/or radiation fields. And this is indeed recognised in the observations (e.g. Danforth & Shull, 2008, Stocke et al., 2006, Tripp et al., 2008, Werk et al., 2016 for H I and O VI) and now also supported by one simulation from Churchill et al. (2015).

For instance, higher ions tend to trace hotther and thinner gas (see e.g. Oppenheimer et al., 2010) and, thus, they tend to trace older metals as well. Ford et al. (2016) find them also to extend further out than low ions, but they seem to be hard to detect and are not found (Liang & Chen, 2014). One could speculate that is connected to small covering fractions if the metals as Simcoe et al. (2006) and Schaye et al. (2007) postulate that small cloudlets may stay unmixed in the CGM (cf. also Maller & Bullock, 2004, Schaye, 2001), however, Schaye et al. (2007) claim that the clouds are short-lived.

O VI Driven Findings

As the above listed findings about the cloudlets already suggests, it is likely that the medium in the virialised halos of low-redshift galaxies is multi-phase. This is

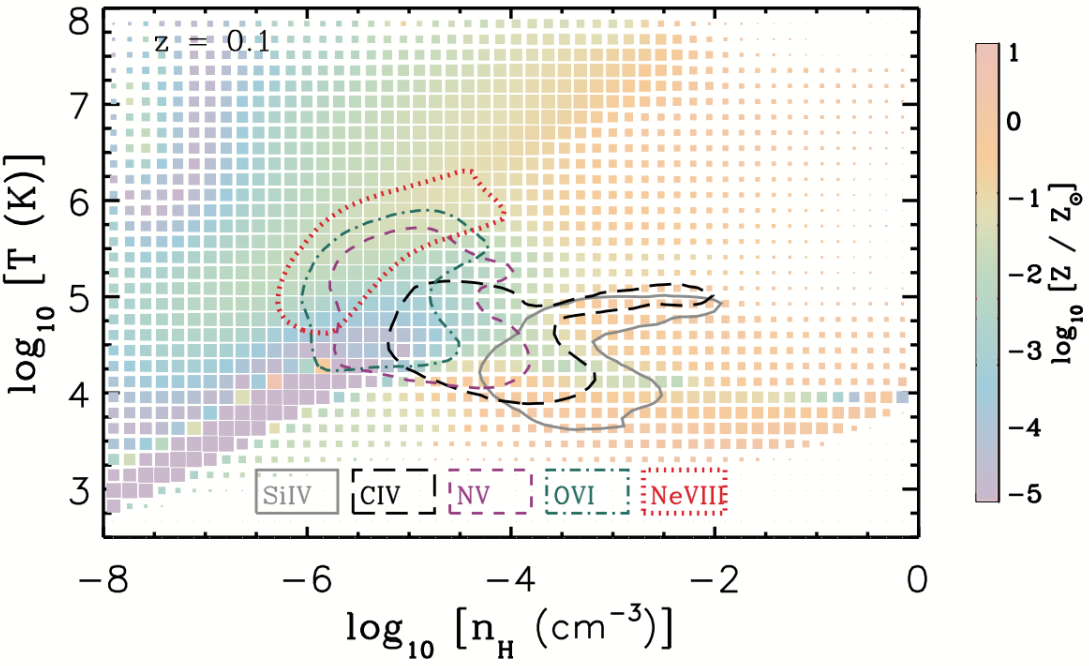

Figure 2.4: The squares show the temperature-density distribution of all gas in the universe of the EAGLE simulation and are proportional to the logarithm of the mass in each bin. Colour encodes the median metallicity. The contours, finally, enclose 80% of the mass of the indicated ions.
The figure is taken from Rahmati et al. (2016).

also supported by C IV and O VI observation from Mo & Miralda-Escude (1996) and Maller & Bullock (2004). These can better be explained by a multi-phase CGM. Even modern simulations still struggle to resemble an appropriate structure (see Hummels et al., 2013).

It is not only the structure that is missing (maybe due to still insufficient resolution in the CGM: see e.g. Oppenheimer et al., 2012) it is also the O VI column densities that are hard to match with observations. Typically, simulations underestimate them by $\sim$0.7 dex (see e.g. Ford et al., 2016, Gutcke et al., 2017, Hummels et al., 2013, Suresh et al., 2015). Next to the multi-phase structure, the differences are typically attributed to inaccurate temperatures in the CGM and/or the wrong feedback / wind models, sometimes also to non-equilibrium cooling (e.g. Cen & Fang, 2006). Oppenheimer & Davé (2009), Oppenheimer et al. (2012) suggest that it is in fact sub-resolution (this again could be connected to insufficient resolution) tur-

bulence that causes the difference between simulations and observations in terms of O VI equivalent widths (EWs). Thom & Chen (2008) also find that non-thermal broadening dominates for their O VI observations.

There are many unclear properties in both simulations and observations. To reduce these, one can try to correlate absorptions to galaxy properties that might disentangle mechanisms for the causes of high or low absorption. A logical consequence of the accumulation of metals in the CGM, the column densities for metal ions should generally increase over time. And for O VI lines with $EW > 0.4$ Å Sargent et al. (1989) indeed found decreasing amount of absorption with redshift.

Observationally there was also a link found between O VI column densities and specific star formation rate (sSFR) (e.g. Tumlinson et al., 2011) for which Oppenheimer et al. (2016), however, claim that it merely reflects characteristics in the temperatures and ionisation states in the halo rather ran being a causal one, where the star formation drives metal enriched outflows. This is not too surprising, though, as the time-scales at which metals are transported out to $\sim$100 kpc is gigayears and over this time the star formation has likely changed.

Stocke et al. (2006) find that in order to explain the wide spread (out to several hundred kpc from the nearest galaxy) O VI absorption dim galaxies ($L < 0.1L^*$) must contribute as well. It might be, that these far galaxies are not associated with the absorption lines as Thom et al. (2011) argue that a velocity closeness (in line-of-sight distance) is probably not sufficient to associate absorption galaxies. On the other end of the spectrum, massive and luminous galaxy contribute significantly to the cosmic O VI absorption, too. These might be even more relevant with strong AGN heating as was found in the Illustris simulations (Suresh et al., 2015). Rahmati et al. (2016), however, find little dependence on AGN feedback in the EAGLE simulations.

Mg II at the Lower End of Ionisation

So far, I have put the focus on O VI, which is preferentially found at high temperatures ($\log_{10}(T\,[\mathrm{K}]) \gtrsim 5$) due to its large ionisation energy. Shifting to Mg II now, one might assume that is much more correlated to H I absorption. Steidel (1995) and Bordoloi et al. (2011) even claim that it is more associated with galaxies than H I. Although typically fit with an exponential Nielsen et al. (2013b) parametrise the correlation between Mg II EWs and impact parameter ρ by a log-linear fit ($\log_{10}(EW_{\mathrm{MgII}}\,[\text{Å}]) = -0.015 \cdot \rho/(1\,\mathrm{kpc}) + 0.27$ (see Fig. 2.5), implying that the EWs fall down even more steeply at larger impact parameters ($\rho \gtrsim 30\,\mathrm{kpc}$). This is also in consonance with Tripp & Bowen (2005) claiming that there is no dependence on the impact parameter for their considered sample with impact pa-

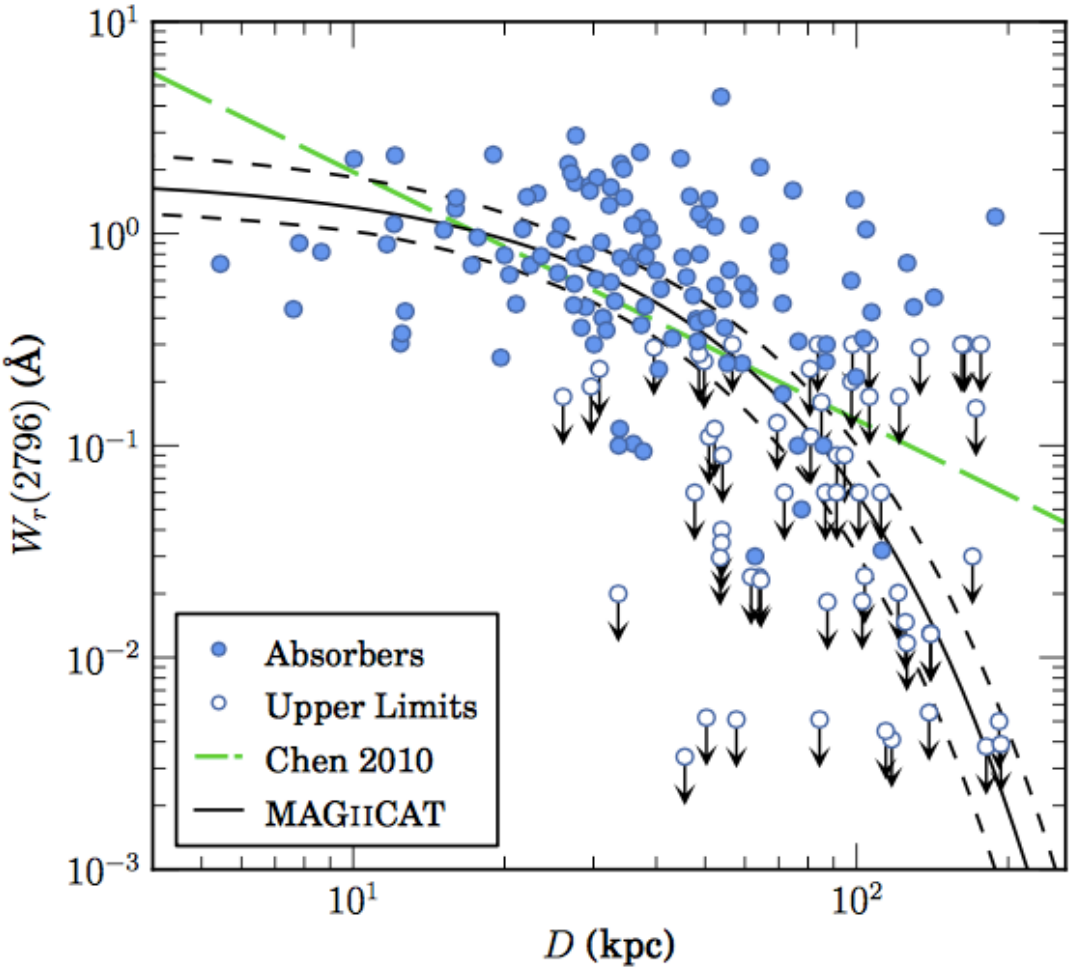

Figure 2.5: The measured Mg II rest-frame EWs from the 'Mg II Absorber-Galaxy Catalog' (MAGIICAT, Nielsen et al., 2013a) versus impact parameter D with a log-linear fit by Nielsen et al. (2013b) to the data: $\log_{10}(EW_{\mathrm{MgII}}\,[\text{Å}]) = -0.015 \cdot \rho/(1\,\mathrm{kpc}) + 0.27$ (the black solid line labeled with MAGIICAT).

rameters of less than $\sim 60\,\mathrm{kpc}$. There might actually be a two-fold population of Mg II absorbers: one evolving with redshift, the other not, power-law for stronger lines ($> 0.3\,\text{Å}$) (Nestor et al., 2005).

A correlation with galaxy parameters similar to what was found for O VI is harder to find. So do Churchill et al. (1996) not find any correlation with galaxy properties (see also Steidel, 1995). Newer observations by (Bordoloi et al., 2011), however, find that blue galaxies have more Mg II absorption, similar to what is found for O VI. It should be noted, though, that the covering fractions of Mg II are small even for small impact parameters of $\sim 30\,\mathrm{kpc}$ (Bowen et al., 1995).

The covering fractions might be small, however, several groups (see e.g. Bordoloi et al., 2011, Bouché et al., 2012, Kacprzak et al., 2012, Nielsen et al., 2015) find that the positions where there is Mg II absorption are not uniformly distributed in terms of the azimuthal angle. Furthermore, they find this dependence to be driven by those that show more absorptions, namely the blue galaxies, associated with star formation (Bouché et al., 2012). The bimodal angular distribution is associated with outflows along the minor axis and inflows along the major axis. This might separate Mg II from H I and O VI as these probably have no(t a so strong) angular dependence (Mathes et al., 2014, Nielsen et al., 2017), but the evidence is not clear at the moment (see e.g. Gutcke et al., 2017, Kacprzak et al., 2015).

C IV and Other Ions

In terms of ionisation energy and, hence, also in terms of temperature and density, they lie far apart. C IV is intermediately ionised and lies 'in-between' Mg II and O VI (cf. also Fig 2.4). This is not just a theoretical result but Danforth & Shull (2008), for instance, find C IV observationally to correlate poorly with H I (an even lower ion than Mg II) and O VI. Thus C IV (and other ions) can add valuable information about the gas properties to those obtained by H I, Mg II, and O VI.

C IV is also found to be in short-lived (Schaye et al., 2007), small clouds that still can produce a covering factor of almost unity out to more than ~ 40 kpc as Mo & Miralda-Escude (1996) argue. C IV might also reside in the contact phase of the clouds and the diffuse hot phase (Mo & Miralda-Escude, 1996). These 'intermediate' phases can put even stronger constrains on the simulation models than just the high and low ions.

2.2.3 Constrains on Feedback Models

As mentioned the matching of not only the established quantities but also absorption features to observations can help to narrow down the large number of different galaxy

formation models to those that describe nature accurately. Indeed, Oppenheimer & Davé (2006) found that enrichment in C IV and the comparison with observation gave strong constrains on their tested models for galactic wind / feedback (see also Oppenheimer et al., 2012). Liang & Chen (2014) also say that galaxy and CGM properties are 'complementary' in terms of feedback models (for their RAMSES suite), meaning that they could only get either of them in concordance with observations.

Also the angular dependences—if they exist—encode information about the outflows, which in turn are shaped by feedback and the density structures in the CGM. Additionally, feedback partly determines the temperatures in the CGM (outflows from SNe mainly heat by shocks, AGNs however might change the halo temperatures also a lot, see e.g. Suresh et al., 2015) and, hence, the ionisation states.

Observationally it is critical to understand them in order to derive total element abundances and metallicities. Still, it is not clear, which ionisation processes dominate in the CGM. Some groups claim that photo-ionisation alone is sufficient (e.g. Thom & Chen, 2008, Werk et al., 2014), others find both, photo-ionisation and collisional ionisation to be important (Ford et al., 2016, Wakker & Savage, 2009, Werk et al., 2016).

2.3 Compendium

So overall the absorption features in the CGM are probably a good discriminant on narrowing down the vast variety of sub-resolution models in todays galaxy formation simulations to the correct ones. It is not unlikely that resolving the multi-phase structure in the CGM is a crucial point along with the right feedback prescriptions. In the following I am presenting a formation model based on the one used by Aumer et al. (2013) and a Python library called PYGAD for analysing smoothed-particle hydrodynamic galaxy formation simulations carried out by some incarnation of the GADGET code (last described by Springel, 2005) such as the one used here. In particular this library contains a module to create mock absorption spectra from the simulations, which is discussed in more detail as it is crucial to precisely understand how the absorption lines arise from the CGM gas. This module is finally applied to the simulation I carried out and the results are compared with observations.

Chapter 3

A Multiphase Galaxy Formation Model

3.1 The Choice of the Galaxy Formation Code

3.1.1 Options

I will generate mock absorption spectra from simulations and compare them observations. Moreover, I will be able to precisely deduce how and from which gas the absorption features arise, which is crucial in understanding and interpreting the QSO absorption observations. In order to have a competitive code, I build on an existing implementation. In terms of the hydrodynamics, the foundation of the baryon physics in galaxy formation simulations, there are three different fundamental approaches: smoothed particle hydrodynamics (SPH), adaptive mesh refinement (AMR) grid codes, and newer methods such as moving mesh codes (as in AREPO, see Springel, 2011) or other mesh-free code than SPH (such as GIZMO, see Hopkins, 2014 and Hopkins, 2015).

SPH is an old player in galaxy formation and it reaches back to Gingold & Monaghan (1977) and Lucy (1977) (for a more recent overview see e.g. Price, 2012 or Hopkins, 2013), who develop this method explicitly for astrophysical problems. The problem to overcome in the field is the huge dynamic range in densities that can span many orders of magnitude from gas in voids with over-densities of $\sim 0.1 \simeq 10^{-29}\,\mathrm{g/cm^3}$ (at redshift zero) to those in the ISM of $0.1 - 1\,\mathrm{g/cm^3}$ and more (the high densities typically are not resolved in the simulations). As each particle in SPH has constant mass[1], the (spatial) resolution automatically scales with the densities.

[1]This condition is usually not (quite) true as gas particles receive mass from stellar feedback.

A further big advantage of this method is that it has Lagrangian nature (as shown by Springel & Hernquist, 2002), implying that it intrinsically conserves mass (obviously), entropy, linear and angular momentum.

However, SPH has problems capturing fluid mixing, especially in shocks, in the Kelvin-Helmholtz instability, and in contact discontinuities, and sub-sonic regimes (e.g. Agertz et al., 2007, Bauer & Springel, 2012, Marri & White, 2003, Morris, 1996, Price & Federrath, 2010). However, many modern variants of the original SPH method have alleviated the problems (e.g. Abel, 2011, Hu et al., 2014, Monaghan, 1997, Price, 2008, Read & Hayfield, 2012, Read et al., 2010, Wadsley et al., 2008).

Eulerian grid codes intrinsically perform better in these problematic situations for SPH even though they tend to over-mix, especially when the resolution is limited (for comparison of SPH and grid methods see Agertz et al., 2007). With fixed grids, they would either completely under-resolve regions of interest—such as galaxies—or by far not performant enough to be applicable in astrophysical situations. When they adaptively increase (or decrease) resolution in situation where, e.g. the density increases or shocks appear, they are called AMR codes and are also a reasonable tool for galaxy formation. Their disadvantages, however, are that they have the aforementioned over-mixing and they are not Lagrangian and, hence, conserve the key quantities mass, entropy, linear and angular momentum worse than SPH codes.

3.1.2 Multiphase SPH

The more recent[2] approaches used in AREPO, GIZMO, and alike combine advantages of both worlds (good convergence, proper capture of shocks, and being Lagrangian) but are probably too new that we know other problems they might have. Hence, the choice of a Lagrangian SPH code is a reasonable one and this work builds on the code used by Aumer et al. (2013), one of the many incarnations of GADGET-3 (last described for public version 2 in Springel, 2005).

The basis of my code, i.e. the one used by Aumer et al. (2013), is a modified version of the code used by Scannapieco et al. (2005, 2006), which in turn built on the multiphase code by Marri & White (2003). This is a unique feature of the code, that especially tries to capture the complex structure in the ISM, but might also be advantageous in the multiphase CGM. The model furthermore includes a self-consistent tracking of the 12 most abundant elements, metal line cooling, star formation, stellar metal production and feedback into a hot and a cold gas phase from SNe type Ia and type II as well as asymptotic giant branch (AGB) stars, and a spatially homogeneous, redshift-dependent UV-background (Haardt & Madau, 2001).

[2]These are generally not so new, but have not arrived in galaxy formation until recently.

With this implementation it is possible to successfully produce realistic present day properties and evolution histories of the spiral galaxy population (see Aumer et al., 2013, 2014, Übler et al., 2014).

In the following of this chapter I describe the code in general, its unique feature of a proper multiphase hydrodynamic treatment, and the improvements I added to the version by Aumer et al. (2013).

3.2 Multiphase Hydrodynamics

From observations (and simulations) we know that the inter-stellar gas has a complex structure with different phases, from hot with large volume-filling factors to cold and dense gas, which should be represented in galaxy formation simulations (see e.g. Naab & Ostriker, 2016). In present-day cosmological simulations it is problematic to self-consistently resolve this phase structure at spatial resolutions of several hundred parsecs and mass resolution in the thousands of solar masses[3]. We know, however, that the surrounding gas of a SN greatly influences what effects it has on the ISM gas (see e.g. Gatto et al., 2015, Walch et al., 2015).

To address this problem, the model treats the gas as a multiphase medium with a continuum of co-existing phases (see Marri & White, 2003). It lets two SPH particles i and j decouple into separate phases, if the following two conditions apply (Aumer et al., 2013):

$$\max\left(\frac{A_i}{A_j}, \frac{A_j}{A_i}\right) > 50 \tag{3.1}$$

$$-\mu_{ij} < c_{ij}. \tag{3.2}$$

Here $A_{i,j}$ are the entropic functions of the particles (see Springel & Hernquist, 2002), $\mu_{ij} := (\vec{v}_i - \vec{v}_j) \cdot \frac{\vec{r}_i - \vec{r}_j}{|\vec{r}_i - \vec{r}_j|}$ is the relative velocity of the particles along their vector of separation, and c_{ij} is the pair-averaged sound-speed. Two SPH-particles decouple if their entropies (actually their entropic functions[4]) are very different unless they approach faster than with the local sound speed.

The velocity restriction (Eq. 3.2) is required to capture shocks properly (Marri & White, 2003), where different entropy gases interact. This multiphase treatment results in a continuum of phases from cold to hot and the results are not very sensitive

[3]Note that the resolution of a simulation is on the order of the mass within a SPH smoothing kernel, i.e. about one or two orders of magnitude larger than the typical gas particle masses

[4]The entropic function A is defined by $P =: A(s)\rho^\gamma$, where P is the pressure, s is the specific entropy, ρ is the density, and γ is the adiabatic index.

to the exact ratio in equation (3.1) and has the advantage that one has not to artificially impose phase transition at chosen temperatures or alike. The model has also been shown to allow for a more realistic modelling of energy and metal injection from stars to the distinct components of the ISM.

3.3 Two-Phase Stellar Feedback

The model considers thermal and kinetic feedback from SNe type Ia and type II, and winds from AGB stars, as well as radiative feedback from massive stars. In this section I describe how the feedback is handled, and the modifications to Aumer et al. (2013). I also briefly describe the additional radiative feedback from O and B stars.

3.3.1 'Hot' and Cold Phase

The effects of all of these feedback types, except the radiation pressure, are distributed between hot and cold gas. For this purpose, it is distinguished between a two phase in addition two the multiphase hydrodynamics as also done by Aumer et al. (2013):

- **Cold (dense) phase:** $T < 8 \times 10^4\,K$ and $n > 4 \times 10^{-5}\,\mathrm{cm}^{-3}$.
- **Hot phase:** all the remaining gas. Note that despite its name, it can contain low density gas with $T < 8 \times 10^4\,K$!

Here we had to introduce a somewhat arbitrary temperature and density cut in opposition to the multiphase hydrodynamics, that however can be motivated by the findings that SNe go off in differently dense—unresolved in galaxy formation simulations—gas with very different effects on the ISM (see e.g. Gatto et al. (2015), Katz (1992), Walch et al. (2015)). The density limit was reduced by Aumer et al. (2013) by a factor of $\sim$100 compared to Scannapieco et al. (2006) as they found that a higher value can have a destructive effect on extended, low-density gas disks due to energetic feedback and we kept the values.

Motivated by the fact that in the neighbourhood of a stellar particle, or within a SPH kernel that will contain about $2.4 \times 10^7 M_\odot$ in the standard simulations, there will always be some unresolved hot and some cold dense gas, the feedback energy, mass, and momentum is distributed between these two phases in which the effects are so different as mentioned above. Unfortunately the exact ratios in nature are not known, however, Aumer et al. (2013) found that the choice of fifty-fifty yields reasonable galaxies in terms of the common measures such as the stellar mass-halo mass relation.

3.3.2 Promotion / Delayed Heating

Feedback from SNe and AGB stars heats the surrounding gas and thereby also the cold phase. As the resolution of the gas is low in terms of properly resolving the small-scale dynamics of a SN and especially the disruption of the unresolved small cold clouds, we delay the thermal feedback until it becomes sufficient to actually heat the gas particle. This allows to break up cold dense clumps of gas and, hence, lowers the cooling rates and the star formation efficiency.

In particular, when a given cold gas particle (as defined above) receives thermal energy from stars, it will not necessarily be added instantaneously as it is done for hot gas particles (also as defined above), but only if this energy is enough to actually heat the cold particle to be hot. Here, 'hot' is defined as follows (cf. also Aumer et al. (2013)): first it is searched for neighbours that decouple (cf. section 3.2) from the particle in question of promotion and their average entropy is calculated. If there are less than five such neighbours, it is set to be the entropy corresponding to the temperature and density defining the separation between the hot and cold phases as defined in subsection 3.3.1. This value also acts as a lower boundary on the average of the hot neighbours.

If now the particle in consideration can reach this threshold density set by the neighbouring hot particles by adding the available thermal energy, this energy will be added. Otherwise, the energy is stored in a reservoir attached to the particle that does not influence its hydrodynamical behaviour until the energy is the reservoir is sufficient to promote the particle. By this scheme it is ensured that a promotion of a cold particle will always be moved it into the local hot phase.

3.3.3 Thermal and Kinetic Feedback from SNe and AGB Stars

We have three kinds a stellar feedback next to the radiative one from massive stars: SNe of type Ia, of type II, and from AGB stars. For the SNe, there is a thermal and a kinetic component, for the AGB feedback there is a kinetic component only, which both are distributed to the ten next hot and ten next cold neighbours (as defined in subsection 3.3.1).

Feedback from SNe

The energy that each SN ejects into the surrounding ISM is typically $\sim 10^{51}$ erg. The code distributes the SN energy into a kinetic and a thermal part. The kinetic part is determined by a momentum transfer of $\Delta p = \Delta m \, v_{\mathrm{eject}}$ by the initial SN ejecta and the outflow velocity is fixed to $v_{\mathrm{eject}} = 3000 \ \mathrm{km\,s^{-1}}$. According to Aumer et al.

(2013) this corresponds to an average kinetic energy of $\sim 1.5 \times 10^{51}$ erg considering the choice of the initial mass function (IMF)—the one proposed by Kroupa (2001)—and SN type II mass interval. However, the actual kinetic energy depends much on the initial relative velocities of the receiving gas particles and typical velocity changes are $20-30\,\mathrm{km/s}$ but can reach more than $100\,\mathrm{km/s}$ (as stated in Aumer et al., 2013). This assumes an inelastic collision of the ejecta and the gas particles (see sketch in Fig. 3.1).

Specifically, each of the 10 nearest hot and cold neighbours of a stellar particle with SNe receives equal parts the total momentum Δp pointing radially away from the stellar particle. If the kinetic energy input is less than 10^{51} erg per SN[5], we add the difference in thermal energy. For the hot particles this thermal energy is added immediately and for the cold particles it is either also added immediately or put into a reservoir until enough energy is accumulated to promote the particle to the hot phase (cf. subsection 3.3.2 about the rules of promotion).

Feedback from AGB Stars

For AGB stars the procedure is very similar. However, they release much less energy and have much smaller velocities. In the version used by Scannapieco et al. (2005, 2006) and Aumer et al. (2013), the AGB mass yields were ejected together with the SNe type Ia and, hence, with a high velocity of 3000 $\mathrm{km\,s^{-1}}$. I decoupled the AGB winds from the SNe type Ia feedback and gave them a velocity of $30\,\mathrm{km/s}$, much closer to the actual values (see e.g. Woitke, 2006), with no additional thermal energy feedback. The reduced the energy input by AGB winds did not change the results significantly (e.g. compare Fig. 3.2). In fact, the galaxies become a little smaller in better agreement with observations than in Aumer et al. (2013).

3.3.4 Radiation Pressure

Based on Hopkins et al. (2011) the stellar populations deposit a momentum of

$$\dot{p}_{\mathrm{rp}} = (1 + \tau_{\mathrm{IR}}) \frac{L_{\mathrm{UV}}}{c} \tag{3.3}$$

to the 10 nearest neighbours as a continuous force acting over the first 30 Myr in the lifecycle of a stellar particle. Here L_{UV} is the ultra-violet luminosity, c is the speed

[5]Note that the change in kinetic energy can even be negative as the gas particle can be slowed down!

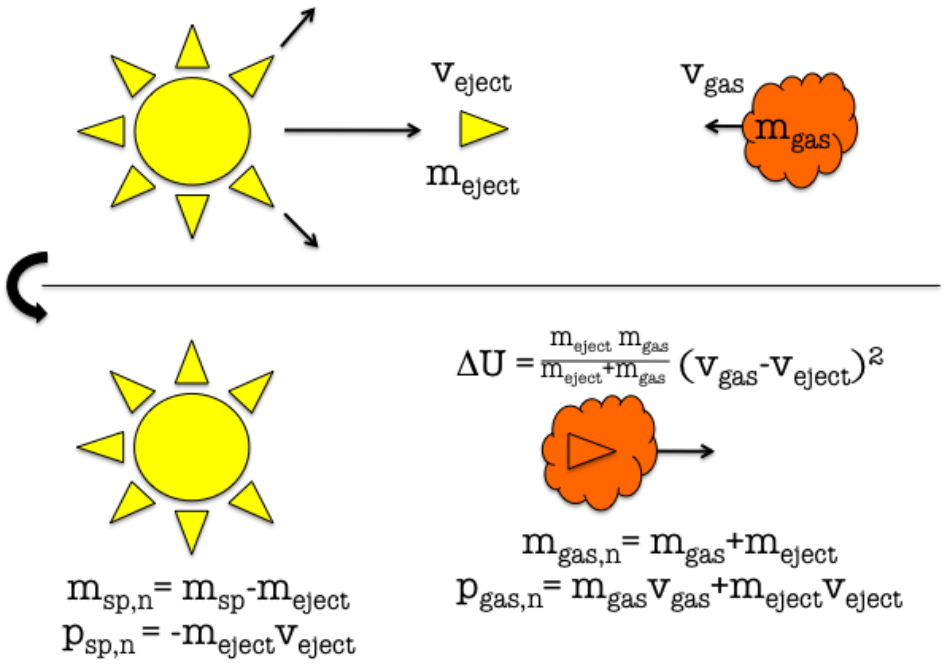

Figure 3.1: A schematic sketch of the momentum transfer ($\Delta p = m_{\rm eject}\, v_{\rm eject}$) and energy input ($\Delta U$) from a stellar particle (yellow ball) to a neighbouring gas particle (orange cloud).

of light, and τ_{IR} is the infrared optical depth. The latter is modelled by

$$\tau_{\mathrm{IR}} = \tau_0 \cdot \max\left(1, \frac{\rho h}{\rho_{\mathrm{sf}} h_{\mathrm{IR}}}\right) \cdot \left(\frac{Z}{Z_\odot}\right) \cdot \min\left(\left(\frac{\sigma}{\sigma_0}\right)^3, 4\right) \tag{3.4}$$

i.e. scaling with the local metallicity Z, the particle's surface density approximated by its density ρ times its smoothing length h (limited at the star-forming surface density), and the surrounding velocity dispersion σ cubed. The parameters used are $\tau_0 = 25$ and $\sigma_0 = 40\,\mathrm{km\,s^{-1}}$. Additionally, the factor of $(\sigma/\sigma_0)^3$ is limited to 4, in order to avoid overly strong forces. This relatively strong radiation pressure feedback helps dispersing dense star forming regions and results in formation histories and final stellar masses in agreement with observations (cf. Fig. 1 of Aumer et al., 2013).

3.4 Star Formation

Gas particles are converted into star particles stochastically such that on average they have a star formation rate of

$$\mathrm{SFR} = \eta \frac{\rho_{\mathrm{gas}}}{t_{\mathrm{dyn}}} \quad \left(\propto \rho_{\mathrm{gas}}^{1.5}\right). \tag{3.5}$$

Here ρ_{gas} is the gas density and $t_{\mathrm{dyn}} \equiv (4\pi G \rho_{\mathrm{gas}})^{-1/2}$ is the local dynamical time for the gas particle. This results in a Kennicutt-Schmidt like relation (Kennicutt, 1998, Schmidt, 1959) locally—as observed over many orders of magnitude—and the star formation efficiency η is set to a typical value of 0.04 (Aumer et al., 2013).

However, gas is tested for star formation only if the density fulfils the following conditions Aumer et al. (2013):

$$n > n_{\mathrm{th}} \simeq 3\,\mathrm{cm^{-3}} \tag{3.6}$$

$$\frac{\rho}{\langle\rho\rangle} > 2000, \tag{3.7}$$

where $\langle\rho\rangle$ is the cosmic mean density and n is the number density of the gas. ($3\,\mathrm{cm^{-3}}$ corresponds to roughly $10^{-1} M_\odot/\mathrm{pc}^3$ or $5 \times 10^{-24}\,\mathrm{g/cm^3}$.) This is in order to avoid sparse star formation in regions of thin gas or too early in the cosmic timeline.

3.5 Metals

Metals are important for cooling (Wiersma et al., 2009) and, hence, heavily influence the condensation of gas into galaxies. Moreover, their ions are the absorbers of QSO

radiation in the CGM and, hence, are determining (together with temperatures and the radiation field) the absorption lines. These are the two main reasons why the simulations need to follow metal production, the distribution of metals, and their effects on cooling. My model self-consistently follows, in addition to Hydrogen and Helium, nine of the most abundant metals in the universe: carbon, nitrogen, oxygen, neon, magnesium, silicon, sulfur, calcium and iron; adding up to eleven elements in total.

3.5.1 Metal Enrichment

Metals are produced in stars and are returned back to the gas by SNe of all types and by winds from AGB stars, too. Therefore, the simulation model enriches the surrounding gas with metals along with the thermal and kinetic feedback from stars. As each stellar particle represents a stellar population with a Kroupa (2001) IMF with limits of $0.1\,M_\odot$ and $100\,M_\odot$, one can calculate the yields for each element and each feedback event.

The SNe type II yields are metallicity-dependent following Chieffi & Limongi (2004), but with the iron yield halved as proposed by Portinari et al. (1998). The element production by SNe Ia follows the W7 model of Iwamoto et al. (1999), with a declining rate by the inverse of the stellar population age sampled in time steps of 50 Myr. I account for the mass recycling by AGB stars, with the same time sampling as for SNe Ia, by using the metal yields of Karakas (2010). In contrast to Aumer et al. (2013) I do not add the mass return of AGN stars to that of the SNe type Ia but assume an outflow velocity of 30 km/s as discussed above. The metal yields, however, are not changed.

Like the kinetic and thermal feedback the metals from AGBs and SNe is injected into both of the two gas phases (hot and cold), 50% into each phase as also done for the Hydrogen and Helium mass of the ejecta. The gas particles then keep track of the masses of each of the eleven followed elements.

3.5.2 Metal Line Cooling

As shown by Wiersma et al. (2009), the cooling rates by metal lines with the correct element abundances are crucial to make correct predictions in galaxy formation simulations. These already become important at sub-solar metallicities and thus at almost all epochs. The model has implemented the cooling rates for optically thin gas in ionisation equilibrium. This includes the redshift dependent UV background of Haardt & Madau (2001) making the cooling rates dependent on redshift, density,

temperature, and chemical composition.

3.5.3 Metal Diffusion

The model also follows metal diffusion due to turbulent gas mixing below the resolution scale, avoiding largely fluctuating metallicities within a single kernel (that contains 32 neighbouring particles), and thus also avoiding vastly different cooling rates for particles in a kernel.

For the purpose of implementing metal diffusion one needs a SPH formulation of the diffusion equation: $\frac{\mathrm{d}c}{\mathrm{d}t} = \frac{1}{\rho}\vec{\nabla} \cdot (D\vec{\nabla}c)$ for some concentration c and its diffusion coefficient D. I do not simply use a discretised SPH formulation, but follow Greif et al. (2009), who argued for a version integrated over the small discrete time step Δt of the simulation. In order to conserve (metal) mass I use the same equation for the metal mass $\mu_i = c_i m_i$ of particle i as Aumer et al. (2013):

$$\Delta\mu_i = \sum_j \mu_{i\to j} \tag{3.8}$$

$$= \sum_j \left(\frac{1}{2} m_i \left(1 - e^{A\Delta t}\right) \frac{1}{A} K_{ij}(c_i - c_j) \right), \tag{3.9}$$

where the sum goes over all SPH neighbours j of particle i, m_i is the i-th particle's mass, $A \equiv \sum_j K_{ij}$, and

$$K_{ij} = \frac{m_j}{\rho_i \rho_j} \frac{4 D_i D_j}{D_i + D_j} \frac{\vec{r}_{ij} \cdot \vec{\nabla}_i W_{ij}}{r_{ij}^2}. \tag{3.10}$$

Here $\rho_{i,j}$ are the particles' densities, W_{ij} is the kernel of particle i at the position of particle j, and $\vec{r}_{ij}$ is the separation vector of the two particles.

Finally, I need to choose the diffusion coefficients D_i. I do not use the coefficient as in Greif et al. (2009), but the diffusion coefficient as proposed by Shen et al. (2010), which does not introduce diffusion in purely rotational or compressive flows due to the use of the trace-free tensor S_{kl} (see their paper for details):

$$D_i = 0.05 \rho_i |S_{kl}| h_i^2, \tag{3.11}$$

where h_i is the smoothing length of particle i. Aumer et al. (2013) found that this coefficient also yields better agreement with observational data such as the mass-metallicity relation when applied in cosmological galaxy formation simulations than the one proposed by Greif et al. (2009).

3.6 The Simulation Sample

With the described model I simulated a suite of zoomed-in cosmological simulations of 12 different halos in a box of 100^3 cMpc^3. The parent dark-matter simulation is the same as the one described in Oser et al. (2010). It was run with a flat ΛCDM cosmology with $H_0 = 72\,\mathrm{km\,s^{-1}\,Mpc^{-1}}$, $\Omega_\Lambda = 0.74$, $\Omega_{\mathrm{matter}} = 0.26$, $\Omega_{\mathrm{baryon}} = 0.044$, $\sigma_8 = 0.77$, and $n_s = 0.95$. These are the values from the 3-year results from WMAP (Spergel et al., 2007).

For the zoom-in simulations I use the same initial conditions (ICs) and the same naming convention as Oser et al. (2010) and Aumer et al. (2013). I restrict myself to ICs with halos with present day M_{200} masses in the range of $4\times10^{11}\,M_\odot - 3\times10^{12}\,M_\odot$. This corresponds to stellar masses in the range from $7.5\times10^9\,M_\odot$ to $1.2\times10^{11}\,M_\odot$ in agreement with abundance matching results (Behroozi et al., 2013, Kravtsov et al., 2014, Moster et al., 2013, cf. Fig. 3.2).

With the minor changes to the original code of Aumer et al. (2013), the key properties of the galaxies do not change significantly. As an example I show the stellar mass-halo mass relation at $z = 0$ (see Fig. 3.2). Except for halo M0977 all central galaxies fall well into the region for stellar masses expected from abundance matching results. M0977 is in a late major merger stage and its stellar mass is about to double from $8\times10^9\,M_\odot$ to $1.4\times10^{10}\,M_\odot$. As my halo finder (cf. chapter 4) considers the two halos to already being merged and its mass is already gone up. Once the merger is complete, the temporary tension is relaxed.

The galaxies in the most massive halos ($> 2\times10^{12}\,M_\odot$) of my ensemble have a tendency towards higher stellar masses, which might be attributed to the absence of super-massive black holes (SMBH) and the feedback of AGNs in my simulations (see e.g. Naab & Ostriker, 2016, Somerville & Davé, 2015).

The galaxies have large dynamical stellar disc masses as listed in Table 3.1, ranging from about a third up to more than 80%. Among these values, Table 3.1 lists other key features of the galaxies at redshift zero such as the HI disc size, The calculation of these quantities is discussed in section 4.3 and subsection 4.3.3. As an example of my simulations I show the structure of halo M0858 in Fig. 3.3, the halo which I will often refer to as an example for the discussion of details of my analysis.

As gas fractions presumeably play an important role for getting the feedback and especially the CGM close to real galaxies, I compare the H I fraction in my galaxies with observations. Catinella et al. (2010) provide a fit to observations and found a relation bewteen the H I mass and stellar mass. My simulated galaxies have slightly higher H I masses but are still well within the scatter around the median (cf. 3.4).

For this work I perform simulations at three different spatial resolutions which

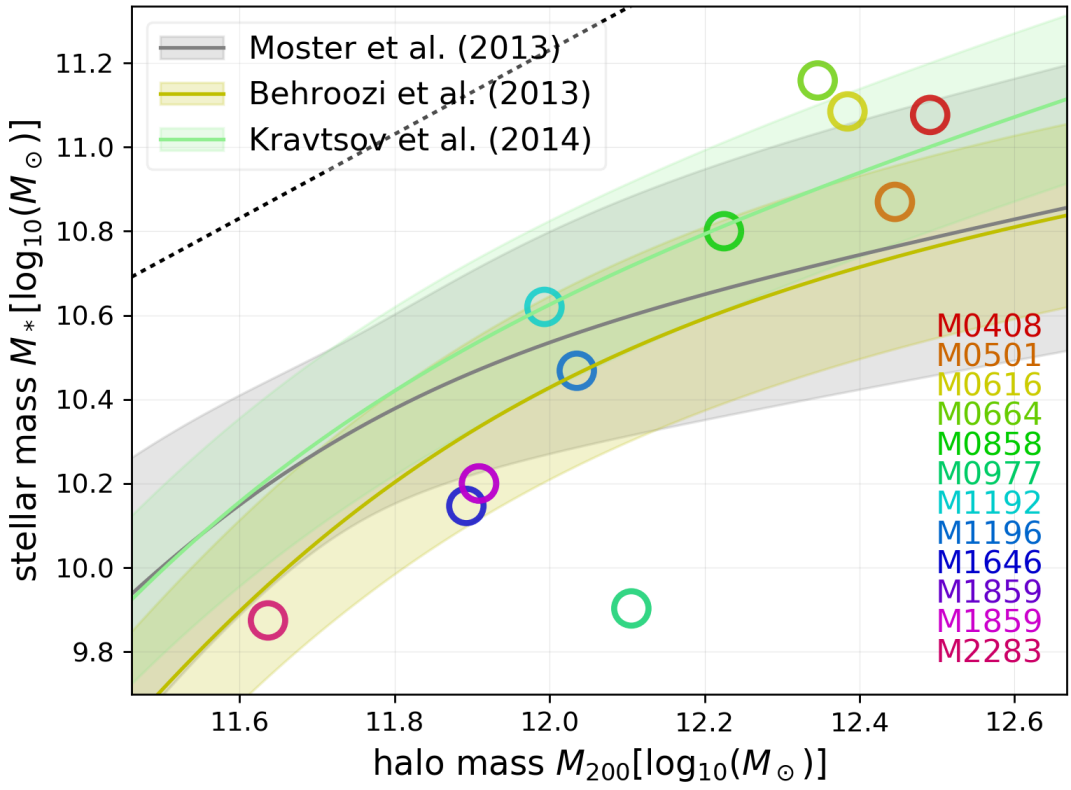

Figure 3.2: The stellar mass–halo mass relation for the simulated halos at redshift zero. For reference, the abundance matching results from Behroozi et al., 2013, Kravtsov et al., 2014, Moster et al., 2013 are shown. With the exception of M0977, which is undergoing a major merger at $z = 0$, all central galaxies agree with abundance matching constrains. At higher halo masses the simulated stellar masses are high, possibly due to missing black hole feedback. The dashed black line indicates the cosmic baryon fraction of the given halo.

halo ID	R_{200} [kpc]	M_{200} [$M_\odot$]	M_* [$M_\odot$]	gas fraction	$M_{\rm HI}$ [$M_\odot$]	$R_{\rm HI}$ [kpc]	gas metallicity	stellar D-to-T ratio	late merger history
M0408	295	3.10×10^{12}	1.19×10^{11}	21.6%	2.12×10^{10}	25.0	2.36 $Z_\odot$	59.7%	smaller, $z \approx 0.3$
M0501	285	2.79×10^{12}	7.41×10^{10}	16.7%	1.01×10^{10}	62.0	1.94 $Z_\odot$	50.1%	large, $z \approx 0.9$
M0616	272	2.42×10^{12}	1.22×10^{11}	20.7%	1.78×10^{10}	17.0	3.02 $Z_\odot$	52.9%	smaller, $z \approx 0.05$
(M0664)	264	2.22×10^{12}	1.44×10^{11}	7.2%	4.50×10^{9}	10.0	2.72 $Z_\odot$	34.2%	ongoing major
M0858	241	1.68×10^{12}	6.31×10^{10}	22.4%	1.15×10^{10}	17.0	2.16 $Z_\odot$	46.0%	small fly-by, $z \approx 0.1$
(M0977)	220	1.27×10^{12}	8.00×10^{9}	55.9%	6.94×10^{9}	45.0	0.50 $Z_\odot$	45.1%	ongoing major
M1192	201	9.85×10^{11}	4.17×10^{10}	22.2%	8.06×10^{9}	20.0	2.01 $Z_\odot$	51.9%	smaller, $z \approx 0.2$
M1196	208	1.08×10^{12}	2.94×10^{10}	26.9%	7.55×10^{9}	25.0	1.43 $Z_\odot$	31.1%	large, $z \approx 0.4$
(M1646)	186	7.81×10^{11}	1.40×10^{10}	43.8%	7.47×10^{9}	20.0	1.04 $Z_\odot$	72.0%	small fly-by, $z \approx 0.1$
M1859	189	8.11×10^{11}	1.59×10^{10}	36.4%	6.40×10^{9}	25.0	1.05 $Z_\odot$	45.7%	small, $z \gtrsim 0.5$
(M2283)	153	4.33×10^{11}	7.49×10^{9}	32.8%	2.27×10^{9}	11.0	0.81 $Z_\odot$	82.1%	ongoing major

Table 3.1: Overview of the simulated halos at redshift $z = 0$ used for this study. The numbering is taken from Oser et al. (2010, 2012) and is identical to Aumer et al. (2013). R_{200} is the radius around the galaxy where the spherical over-density drops below $200\,\rho_{\rm crit}$ and M_{200} is the mass within that sphere. M_* is the stellar mass within 10% of R_{200}. Gas fractions ($M_{\rm gas}/M_{\rm baryons}$), gas metallicities, and disk to total ratios (D/T, cf. section 4.3) are also taken within that radius. Galaxies with ongoing mergers are in parentheses and are excluded from my analysis.

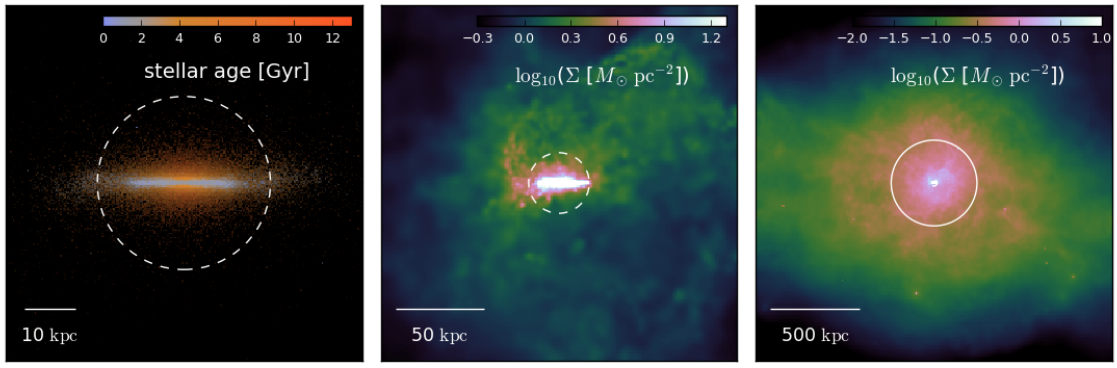

Figure 3.3: Morphological impression of galaxy M0858. In the left panel I show (edge-on) the stellar V-band luminosities, colour coded by the mean (V-band weighted) stellar ages. The galaxy has a thin and young stellar disk. The middle panel displays the gas column density distribution in and around the galaxy. In the right panel I show the gas distribution beyond the galaxies' virial radius. The respective spatial scales are given in the lower left corner of the panels. The dashed circles indicate the HI disc size, $R_{\rm HI}$, and the solid circle indicates R_{200}.

level	softening length [cpc/h_0]		particle masses [$M_\odot$]	
	baryons	dark matter	baryons	dark matter
2x	400	900	5.9×10^6	2.9×10^7
4x	200	450	7.4×10^5	3.6×10^6
8x	100	225	9.2×10^4	4.5×10^5

Table 3.2: Overview of the different resolutions levels in the zoom region. The masses are initial masses, since gas particles can later accumulate mass from stellar feedback and metal diffusion.

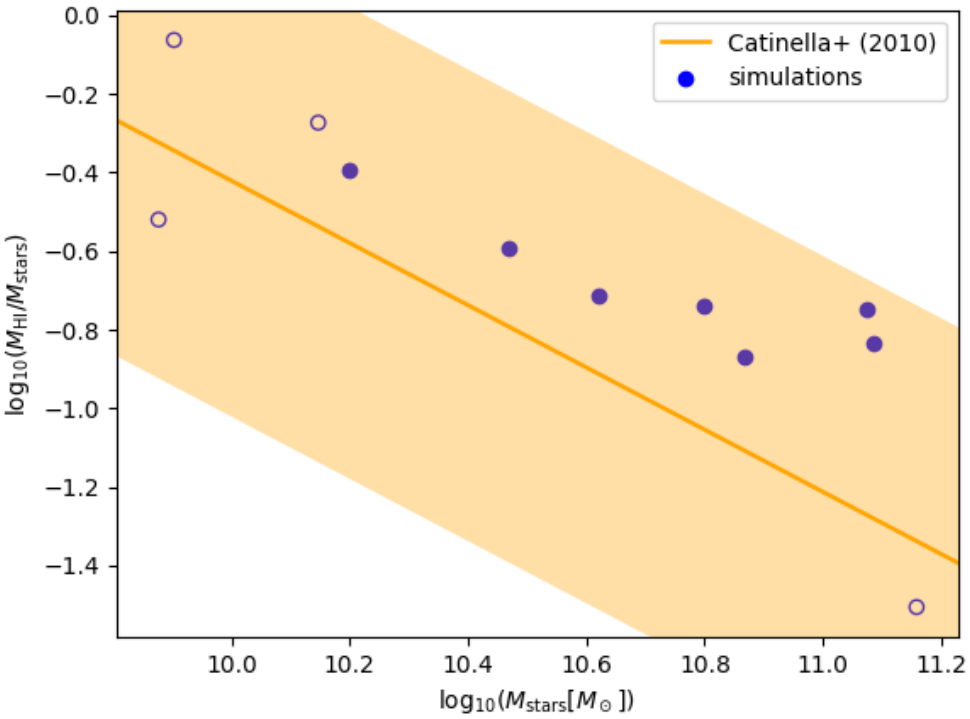

Figure 3.4: The H I fractions as a function of stellar mass in my simulation ensemble. Open circles mark galaxy with merger features. The orange line with the band indicating the scatter (root mean sqaure) was derived from observations by Catinella et al. (2010)

are referred to as '2x', '4x', and '8x' (see Table 3.2). If not stated otherwise, I use the intermediate resolution (4x). Here the (initial) gas particle mass is $7.4 \times 10^5 M_\odot$ and the gravitational softening length is $200\,\mathrm{cpc}/h_0$, which corresponds to 144 pc at redshift 0. The other resolution levels are used for convergence studies.

Chapter 4

The Analysing Framework and PYGAD

Due to the lack of publicly available, powerful analysis libraries for SPH galaxy simulations[1], I have written a new one, called PYGAD Röttgers (2017). Here, I will briefly describe the gist of PYGAD, describe the standard analysis pipeline used for the simulations, and discuss the absorption spectra generation module of PYGAD in more detail.

4.1 Motivation

The reuse of code is an important concept in programming. It does not only reduce the amount of work, but also reduces the probability for bugs significantly, because there is less code in which bugs can occur and the same code is used more often and in more different conditions—ever more if it is public as it then it used even more often. That makes it more likely to find possible bugs. Writing such code with a well documented user interface and robust, easy-to-use functionality, however, requires severe time investment, that only pays off in the long term.

Furthermore, a smart framework allows to exclude easy mistakes like wrong unit conversions. PYGAD decorates data with units, properly tracking them during calculation to avoid such a problem. PYGAD also allows for easy masking of simulation snapshots to sub-snapshots of interest, e.g. just the hot gas in the CGM, and all functionality of the library can also be applied to that sub-snapshot only. This way,

[1] A noteworthy available code is PYNBODY, which, however, does not work well with GADGET simulations.

one can save time in programming by using PYGAD, sparing it for scientific questions.

4.2 Binning and Plotting

The binning routines of the library—which are the basis for the creation of maps—entirely account for the SPH smoothing and furthermore ensure that integral quantities are conserved during the binning (for instance, if density is binned onto a grid the total mass is conserved). The main problems that occur, if the smoothed quantities are binned in a naive way by simply evaluating the kernel at the grid cell centres, are the following two: 1) the smoothing lengths might be so small that no grid cell centres overlap with the kernel, or 2) the discrete integral, i.e. the sum over the kernel values at the grid cell centres times the grid cell volumes, is inaccurate and does not yield unity (note that the kernel is normalised to one).

The challenge is to avoid these problems and at the same time loose as little information as possible. Mathematically one could simply make the grid more fine-grained. That is, however, not feasible as the size of a grid cell would have to be much smaller than the smallest smoothing length and the smoothing lengths in galaxy simulations vary over many order of magnitudes down to small scales of $\sim 0.1\,\mathrm{kpc}$ in my simulations (Fig. 4.1 show the rather typical distribution of smoothing lengths in the halo of M0858). With at least 10 grid cells along a smoothing length and a total grid size of 100 kpc, that would require a grid side length (assuming a regular grid) of 10^4 grid cells or 10^{12} grid cells in total. Besides numerical issues, that would results in extremely large runtimes.

There have been used several different approaches to this problem: from simply ignoring the smoothing and handling the SPH particles as point masses, over codes that extend the smoothing lengths such that it is larger than the grid cell size (see e.g. Buneman, 1973, Hockney & Eastwood, 1981), to even more sophisticated one such as SPLASH by Price (2011), which integrates numerically along several lines of sights, with the option to require the SPH interpolation of unity to be one: $\sum_j \frac{m_j}{\rho_j} \cdot 1 \cdot W(|\vec{r} - \vec{r}_j|, h) \approx 1$. Here the sum is over all particles j with mass m_j, density ρ_j, and position $\vec{r}_j$, the kernel W, and the smoothing length(s) h. Another available code, SPLOTCH, by Dolag et al. (2008) even uses ray-tracing to generate maps from galaxy simulations. I, however, want to be able to bin any SPH quantity into 2D and 3D (regular) grids, which can be used for further calculations as well as for plotting.

The method I developed for PYGAD normalises to the discrete integral (i.e. the

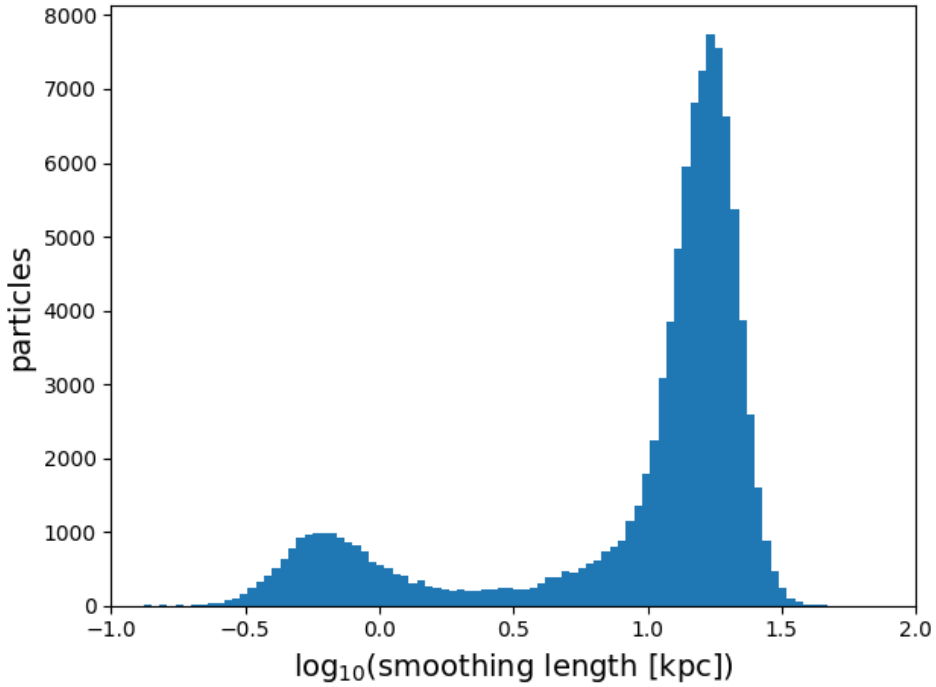

Figure 4.1: The distribution of smoothing lengths in the halo (i.e. of particles with radii $< R_{200}$) of M0858. The relative size of the two peaks can change a lot for different halos, but their position does not.

sum) over the grid cell k of the kernel W of each particle j to unity:

$$S_j := \sum_k \Delta V^{(k)} W(\vec{r}^{(k)} - \vec{r}_j, h_j) \stackrel{!}{=} 1, \tag{4.1}$$

where $\Delta V^{(k)}$ is the volume of the grid cell k and $\vec{r}^{(k)}$ its centre position. This uses the so-called scatter approach by using the smoothing length h_j of the particles j. The grid cell value $\tilde{A}^{(k)}$, i.e. the value in one 3D bin of the grid, for some field A is

$$\tilde{A}^{(k)}\Big|_{S_j \neq 0} := \sum_{j, S_j \neq 0} \Delta V_j \, S_j^{-1} \, A_j \, W(\vec{r}^{(k)} - \vec{r}_j, h_j), \tag{4.2}$$

where A_j is the field value of the particle, $\vec{r}_j$ its position, h_j the particle's smoothing length, and ΔV_j the volume associated with the particle (this is m_j/ρ_j in the classical formulations of SPH, for different formulations see Hopkins, 2013). The expression is the classical SPH smoothed quantity at the grid cell's centre, except for the normalisation factor S_j. This normalisation factor approaches unity as the grid cell sizes go (well behaved) to zero due to the normalisation of the kernel: $\int \mathrm{d}\vec{r} W(\vec{r}, h) = 1$.

If a sum S_j is zero, the kernel's compact support does not include any grid cell centres and $\tilde{A}^{(k)}$ is not defined (the particles 'fall through the grid'). Such particles are excluded from the above sum and added to the grid separately. Intending to conserve the integrals, I add the particles j with $S_j = 0$ by

$$\tilde{A}^{(k)}\Big|_{S_j=0} := \sum_{\substack{j \\ S_j \neq 0}} \frac{\Delta V_j}{\Delta V^{(k)}} \, A_j \tag{4.3}$$

to the grid cell k closest to the particle j. It now is a simple task left to the reader to proof that the sum over the grid of the cell values $\tilde{A}^{(k)} \equiv \tilde{A}^{(k)}\Big|_{S_j \neq 0} + \tilde{A}^{(k)}\Big|_{S_j=0}$ times the grid cells' volume (a discretised integral) is equal to the integral over the classical SPH smoothed field $A(\vec{r})$:

$$\int \mathrm{d}\vec{r} \, A(\vec{r}) \equiv \int \mathrm{d}\vec{r} \sum_j \Delta V_j \, A_j \, W(\vec{r} - \vec{r}_j, h_j) \tag{4.4}$$

$$= \sum_j \Delta V_j \, A_j \stackrel{!}{=} \sum_k \Delta V^{(k)} \, \tilde{A}^{(k)}. \tag{4.5}$$

A demonstration of the goodness of the conservation of the integrals is shown in Fig. 4.2 on the example of the density distribution in halo M0408 over a grid

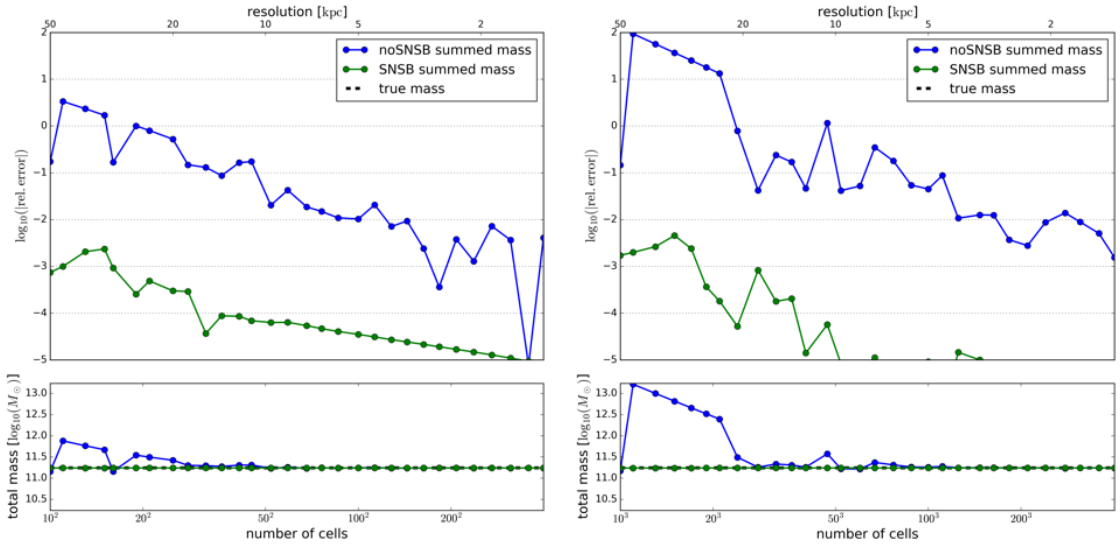

Figure 4.2: The SPH mass density was binned onto a 3D grid (right plot) as well as into a projected 2D grid (left plot) with and without the normalised binning routines of PYGAD and the integral over these grids, the total mass, was compared to the true values (obtained by a sum over all particles). The upper plots show the relative errors in the mass for the two methods and the bottom plots the obtained masses. The grid is 500 kpc on a side and spans over the zoomed-in halo M0408.

spanning $(500\,\mathrm{kpc})^3$ around the zoomed-in halo. Note that without the normalisation with more than $200^3 = 8 \times 10^6$ grid cells an error of more than 1% can occur in the integrated quantity and with 50^3 grid cells an order unity error occurs! The PYGAD's normalised version has errors that are three to four orders of magnitude smaller.

As the conservation might not be sensible for some quantities or under certain circumstances, it can be turned off in PYGAD. The grid extensions can be chosen freely in PYGAD and it is not necessary to bin over the entire simulation domain. Moreover an optimised 'projected' version is provided, that is equivalent to summing the 3D grid along one axis. This 2D binning routine was written not only for convenience but also because it is more memory efficient and also typically two orders of magnitudes faster. This function is also utilised in the map plotting routines of PYGAD.

Regarding the plotting, I want to note explicitly that bad choices in the colour map can skew the impression the viewer gets from the actual quantitative map. Choosing a non-distorting colour map involves the physiology of human colour per-

ception, which is not straight forward. It is probably because of that that naively chosen, distorting colour maps (two typical ones are called 'jet' and 'rainbow') became widely used and persist to be used even though they create false features (for further information see e.g. Borland & Ii, 2007). In PYGAD I was careful to avoid such colour maps[2].

4.3 Analysis of the Simulations

4.3.1 The Halo and the Galaxy

In a first step of analysing the simulations, I identify the main halos and its largest galaxy of the high-resolution part of the zoom simulations with a simple friends-of-friends (FoF) finder, that is also part of PYGAD as all routines described in the following. The simulation snapshots are then centred on the main galaxies of these halos, using a shrinking sphere method (Power et al., 2003) on the stars, and calculate the spherical over-density mass M_{200} and radius R_{200}, i.e. the radius where the average density falls below 200 times the average density of the universe. All baryons within 10% of R_{200} are defined as galaxies (c.f. Oser et al., 2010).

For rotating the systems to the edge-on projection I use the eigenvectors of the 'reduced inertia tensor' (Bailin & Steinmetz, 2005, Gerhard, 1983) of the galaxies, which are typically dominated by the stars as the mean gas fraction is close to 20% (cf. Tab. 3.1). The z-axis is then aligned with the minor axis and the x-axis along the major axis of the galaxies.

I determine the dynamical disc fractions using the 'circularity parameter' $\epsilon := j_z/j_{\mathrm{circ}}(E)$ as defined in Abadi et al. (2003) for each star particle. Here j_z is the z-component (along the minor axis) of the angular momentum of a given particle and $j_{\mathrm{circ}}(E)$ is the angular momentum of a particle with the same energy E of the given particle on a circular orbit. The disc component is defined by all particles with $\epsilon > 0.85$ (i.e. particles on almost circular orbits), which have a modulus of the z-coordinate that is not larger than 5 kpc (star particles in the disc plane), and $R = \sqrt{x^2 + y^2}$ of at most 50 kpc (which excluded unrelated structures).

4.3.2 Stellar luminosities

In order to calculate stellar luminosities I use the tables of Marigo et al. (2008), updated by Girardi et al. (2010) (using a Kroupa, 2001 IMF) provided online at

[2] PYGAD is based in the matplotlib library, older versions of which used such 'bad' colour maps by default. It has improved since version 2.

http://stev.oapd.inaf.it/cgi-bin/cmd. Circum-stellar dust is ignored. Each star particle in the simulations represents a single stellar population (SSP). With the use of the tables of integrated SSP magnitudes I can calculate the luminosities of various bands (U, B, V, R, I, J, H, K) as well as bolometric ones.

4.3.3 Ionisation Fractions and H I

For whatever line I want to create an absorption spectrum, most and foremost I must know the density distribution of the ion that generates the line. I also need the H I distribution in order to determine the H I disc sizes, $R_{\rm HI}$. As the simulations evolve the 11 most abundant elements self-consistently and individually, I just need to calculate the ionisation fraction of the ion of interest. I generally will do this within the approximation of an optically thin gas in ionisation equilibrium (which also was an approximation in the metal line cooling calculations Wiersma et al. (2009) and is typically sufficient for absorption lines, see Churchill et al., 2015) and account for self-shielding.

The ionisation fractions in the optically thin approximation (without self-shielding) can be calculated using CLOUDY (last described in Ferland et al., 2013) tables. To include self-shielding is a more demanding task and I will use the results of Rahmati et al. (2013) (directly for H I and in a modified way to estimate those for metal lines). I, however, do not calculate the fraction of molecular hydrogen (H_2) as I do not have the resolution to reliably predict the conditions in gas that is sufficiently dense. It is also a sub-dominant component outside the gas disc and, hence, not relevant for my work.

4.3.4 Hydrogen Self-Shielding

In the absence of self-shielding I can estimate the ionisation state of hydrogen with a pre-calculated CLOUDY table of the hydrogen ionisation rate $\Gamma_{\rm HI}$ as a function of redshift (and UVB). Since self-shielding is important, I follow the method described in Rahmati et al. (2013). They approximate the typical densities at which hydrogen starts to become self-shielding, $n_{\rm H,ss}$, as a function of the neutral hydrogen absorption cross-section for ionisation $\sigma_{\rm HI}$. Its redshift dependence is approximated by the fitting formula:

$$\sigma_{\rm HI} = 2.31 \cdot 10^{-18} + 0.96 \cdot 10^{-18} \times (1+z)^{-1.18} \tag{4.6}$$

Following Rahmati et al. (2013) I assume:

$$n_{\mathrm{H,ss}} = 6.73 \cdot 10^{-3} \left(\frac{\sigma_{\mathrm{HI}}}{2.49 \cdot 10^{-18}} \right)^{-2/3} \times \left(\frac{f_{\mathrm{baryon}}}{0.17} \right)^{-1/3} \left(\frac{\Gamma_{\mathrm{HI}}}{10^{-12}\,\mathrm{s}^{-1}} \right)^{2/3} \tag{4.7}$$

This parameter allows to calculate the fraction of the ionisation from the UV background that is not shielded by the following fitting formula from Rahmati et al. (2013):

$$\frac{\Gamma_{\mathrm{photo}}}{\Gamma_{\mathrm{UVB}}} = 0.98 \cdot \left[1 + \left(\frac{n_{\mathrm{H}}}{n_{\mathrm{H,ss}}} \right)^{1.64} \right]^{-2.28} + 0.02 \cdot \left[1 + \left(\frac{n_{\mathrm{H}}}{n_{\mathrm{H,ss}}} \right) \right]^{-0.84} \tag{4.8}$$

Accounting for collisional ionisation (Theuns et al., 1998) this finally yields a neutral hydrogen fraction of H I, $\eta := n_{\mathrm{HI}}/n_{\mathrm{H}}$ (cf. formula (A4) in Rahmati et al., 2013):

$$\eta \left[\Gamma_{\mathrm{photo}} + \Lambda_T (1-\eta) n_{\mathrm{H}} \right] = \alpha_A (1-\eta)^2 n_{\mathrm{H}}. \tag{4.9}$$

Here α_A is the Case A recombination rate[3], which is approximated by the fitting formula given by Hui & Gnedin (1997):

$$\alpha_A = \frac{\lambda^{1.503}}{\left(1 + (\lambda/0.522)^{0.47}\right)^{1.923}} \times 1.269 \cdot 10^{-13}\,\mathrm{cm}^3\,\mathrm{s}^{-1}, \tag{4.10}$$

where $\lambda \equiv 315\,614\,\mathrm{K}/T$. Λ_T in turn is approximated (Theuns et al., 1998) by

$$\Lambda_T = \frac{\sqrt{T/(1\,\mathrm{K})} \cdot \exp\left(-157\,809\,\mathrm{K}/T\right)}{1 + \sqrt{T/(10^5\,\mathrm{K})}} \times 1.17 \cdot 10^{-10}\,\mathrm{cm}^3\,\mathrm{s}^{-1}. \tag{4.11}$$

All these calculations are done for each gas particle. One might argue that densities (and temperatures) at any given position in the computational domain are only meaningful in SPH once the overlapping smoothing kernels are properly taken into account. Otherwise the values can be—and mostly are—multi-valued at a given position in space. This is the strict SPH interpretation. However, since I am dealing with

[3]For reasons why this is not Case B, see Rahmati et al. (2013).

a multiphase formulation, my gas is meant to be multi-valued at a given position in space (beyond the usual SPH noise). (In fact most modern galaxy formation codes using SPH are to some degree multiphase, because the implementations of winds and feedback rely on a handful or individual particles that behave in a special way, e.g. might entirely decouple from the surrounding gas.) As I furthermore do not have distinct phases, which I could straightforwardly handle separately and then combine the H I masses, the only consistent way is to treat each particle as all its mass has the particle's temperature and density.

I determine H I disc sizes (c.f. Tab. 3.1) as the radius at which the face-on radial surface density profile of H I falls below $1\,M_\odot\mathrm{pc}^{-2}$ (c.f. Wang et al., 2014).

4.3.5 Self-Shielding of Metals

For the metal ions, I look up the ionisation fractions in a CLOUDY table for the given UVB as a function of hydrogen density n_H and temperature T like for the H I fractions. If I want to include self-shielding, I have to do the analogous as for H I: attenuate the cosmic background radiation to do self-shielding. If I assume that the shielding at the wavelengths of the metal lines is similar to that at the wavelength of Ly_α, I can approximate the attenuation with formula (4.8). Furthermore assuming an optically thin gas, as I did throughout my work, I can use the same look-up tables as for the case without self-shielding and simply scale the look-up density of hydrogen up by the factor the radiation is attenuated, because in the optically thin limit the attenuation fraction scales linearly with the density.

4.4 Mock Absorption Line Spectra

4.4.1 Line Spectra of Homogeneous Gas

Assuming a homogeneous element of number density n, the attenuation of radiation with intensity I though a thin slice of that gas of thickness $\mathrm{d}l$ is:

$$\frac{\mathrm{d}I}{I} = -\sigma\, n\, \mathrm{d}l \tag{4.12}$$

The cross section σ dependents on the material in the slice. By integration one gets

$$I = I_0 \exp\left(-\int_\mathrm{l.o.s.} \sigma\, n\, \mathrm{d}l\right) \equiv I_0 \exp(-\tau) \tag{4.13}$$

with the definition of optical depth, $\tau \equiv \int \sigma\, n\, \mathrm{d}l$. Given a constant cross section, i.e. a constant material (and frequency), the optical depth is: $\tau = \sigma\, N$, with the number column density N.

In general the cross section is frequency dependent. In the case of a line absorption, one can write:

$$\sigma(\nu) = \sigma_0\, \phi(\nu) \tag{4.14}$$

where ϕ describes the line shape and is normalised[4], $\int_0^\infty \mathrm{d}\nu\, \phi(\nu) = 1$, and σ_0 is the overall cross section. The latter is given by:

$$\sigma_0 = f\, \sigma_{\mathrm{cl}} \tag{4.15}$$

$$\sigma_{\mathrm{cl}} := \frac{\pi e^2}{(4\pi\varepsilon_0)\, m_e c} \simeq 0.02654\,\mathrm{cm^2\,s^{-1}} \tag{4.16}$$

where f is the oscillator strength of the given line and σ_{cl} is the so-called *classical cross section.*

4.4.2 The Voigt Profile

The line shape of QSO absorption lines by a homogeneous slice of gas are a result of two effects. One is the Doppler shifts due to thermal motion of the gas particles. If an absorbing atom has some velocity relative to the source of the radiation, this radiation is red- or blue-shifted in the rest-frame of the atom and the absorption happens the corresponding frequency. This is true for the gas in its entirety that moves relatives to the emitter and for the additional movement of the atoms due to thermal motions. The Maxwell distribution of the velocities causes a Gaussian line shape of

$$\phi_{\mathrm{thermal}}(\nu) = \frac{1}{\nu_D \sqrt{\pi}}\, \exp\left(- \left(\frac{\nu - \nu_0}{\nu_D} \right)^2 \right), \tag{4.17}$$

where $\nu_D = \nu_0 \frac{v_{\mathrm{th}}}{c} = \frac{\nu_0}{c} \sqrt{\frac{2\, k_B\, T}{m_{\mathrm{ion}}}} \equiv \lambda_0^{-1}\, b$.

The other effect shaping the absorption lines is the uncertainty in the energy levels relevant for the absorption. Due to Heisenberg's uncertainty principle, the atomic energy levels are not sharply defined and a photon can excite the atom if it

[4]Note that the normalisation implies that ϕ is not unit-less, but has units of inverse frequency, i.e. time!

does not have exactly the energy of the difference of the two levels. The probability for such an event is described by the relativistic Breit-Wigner distribution, which is typically approximated (using that the line width is much smaller than the frequency of the centre) by a Lorentz distribution:

$$\phi_{\text{natural}}(\nu) = \frac{1}{4\pi^2} \frac{\Gamma}{(\nu - \nu_0)^2 + \left(\frac{\Gamma}{4\pi}\right)^2}, \tag{4.18}$$

where $\Gamma = \frac{1}{\tau} = A_{ki}$ is the inverse of the lifetime τ or the Einstein coefficient A_{ki} for the transition of the two involved energy levels k and i.

Since both effects happen at the same time and each atom with a thermal velocity following the Maxwell distribution has a natural width following the Lorentz distribution, the total line shape of an absorption line is the convolution of the Gaussian shape due to thermal broadening and the Lorentzian due to its intrinsic line shape:

$$\phi(\nu) = \left(\phi_{\text{thermal}} * \phi_{\text{natural}}\right)(\nu) \equiv \int \mathrm{d}\nu' \phi_{\text{thermal}}(\nu') \cdot \phi_{\text{natural}}(\nu - \nu'). \tag{4.19}$$

In the conditions of the CGM the temperatures are typically high enough that the thermal Doppler broadening is much larger than typical natural line widths. For instance, for Lyman-α it is $\nu_D = \frac{\nu_0}{c} \cdot b \simeq \frac{2.466 \times 10^{15}\,\text{Hz}}{c} \cdot (12.84\,\text{km/s}) \simeq 1.06 \times 10^{11}\,\text{Hz}$ at $T = 10^4\,\text{K}$ and $\Gamma \simeq 4.7 \times 10^8\,\text{Hz} \ll \nu_D$. Hence, the line shape is dominated unless the column densities are high enough that the wings of the Lorentzian profile also cause significant absorption. This happens in the so-called 'square-root regime' of the curve of growth (see section 4.4.3) and the wings in the spectrum are typically referred to as 'damping wings'.

4.4.3 Equivalent Width and Curve of Growth

The equivalent width is defined as the integral over the line. This is:

$$EW_\lambda \equiv \int_0^\infty \mathrm{d}\lambda \left(\frac{I_0(\lambda) - I(\lambda)}{I_0(\lambda)}\right) \tag{4.20}$$

$$= \int_0^\infty \mathrm{d}\lambda \left(1 - e^{-\tau(\lambda)}\right) \tag{4.21}$$

where I_0 is the flux before entering the gas and I is the flux after attenuation as in Eq. (4.13). Sometimes an analogue definition in frequency space is used, then labeled EW_ν, with $EW_\lambda/\lambda_0 = EW_\nu/\nu_0$. The quantities λ_0 and ν_0 are the line centres. The 'curve of growth' is the relation between the equivalent width and the column density N.

Linear Regime

In the regime of optically thin gas, $\tau \ll 1$, the curve of growth is linear to good approximation. By expanding the exponential in Eq. (4.13) to linear order and assuming a width that is small compared to the position of the line, $\Delta\nu \ll \nu_0$, one gets the following relation between equivalent width $EW_\lambda/$ and column density N:

$$\frac{EW_\lambda}{\lambda_0} = \frac{EW_\nu}{\nu_0} = \lambda_0 \, N \, f \, \frac{\sigma_\mathrm{cl}}{c} \tag{4.22}$$

$$\simeq 0.885 \times f \times \frac{\lambda_0}{1000\,\text{Å}} \times \frac{N}{10^{17}\,\mathrm{cm}^{-2}} \tag{4.23}$$

In the case of Ly_α this yields equivalent widths of ~ 0.054 Å at a column density of $10^{13}\,\mathrm{cm}^{-2}$. This is independent of the actual line shape—as long as the line originates from a homogeneous slice of gas, all with the same temperature and no internal motions.

Logarithmic / Flat Regime

Once the line starts to be saturated in the centre, its shape influences the equivalent width. Let us assume a pure thermal and/or turbulent broadening (with the natural line width being much smaller as it is the case for Ly_α) such that the line profile can be described by a Gaussian:

$$\phi(\nu) = \frac{1}{\nu_D\sqrt{\pi}} \exp\left(-\left(\frac{\nu-\nu_0}{\nu_D}\right)^2\right), \tag{4.24}$$

where $\nu_D = \nu_0 \frac{v_\mathrm{th}}{c} = \frac{\nu_0}{c}\sqrt{\frac{2\,k_B\,T}{m_\mathrm{ion}}} \equiv \lambda_0^{-1}\,b$ for a pure thermal broadening. b is commonly referred to as the Doppler b-parameter.

The equivalent width now is

$$EW_\nu \equiv \int_0^\infty \mathrm{d}\nu \, \left[1 - \exp\left[-\frac{\tau_0}{\nu_D\sqrt{\pi}}\, e^{-\left(\frac{\nu-\nu_0}{\nu_D}\right)^2}\right]\right], \tag{4.25}$$

where I have defined $\tau_0 := N\,f\,\sigma_\mathrm{cl}$ and the assumption of a saturated line translates to $\tau_0 \gg \nu_D\sqrt{\pi}$. This implies that the integrand in the neighbourhood of the line is roughly one and will rapidly decay where the argument of the outer exponential is of the order of unity. The latter happens at $|\nu - \nu_0| \approx \nu_D \ln(\tau_0/(\nu_D\sqrt{\pi}))^{1/2}$. Approximating the integrand by one within these limits and zero outside then gives:

$$EW_\nu \approx 2\,\nu_D \sqrt{\ln\left(\frac{N\,f\,\sigma_\mathrm{cl}}{\nu_D\,\sqrt{\pi}}\right)} \tag{4.26}$$

In other words: the equivalent width only depends logarithmically on the column density, but almost linearly on the Doppler broadening ν_D or the b-parameter.

The transition between the linear regime and the logarithmic regime does not only depend on the line itself, but also on the width due to Doppler broadening as the requirement is $N\,f\,\sigma_{\mathrm{cl}} > \nu_D\sqrt{\pi}$. In the case of pure thermal broadening at a temperature T and a Ly_α absorption line, the transition from the linear to the logarithmic regime is at column densities around

$$N_{\mathrm{linear}}^{\mathrm{log}} \approx \frac{1}{\lambda_0\, f\, \sigma_{\mathrm{cl}}} \sqrt{\frac{2\pi\, k_B\, T}{m_{\mathrm{H}}}} \tag{4.27}$$

$$\simeq \begin{cases} 1.7 \cdot 10^{13}\,\mathrm{cm}^{-2}, & \text{for } T = 10^4\,\mathrm{K} \text{ or } b \approx 12.8\,\mathrm{km\,s}^{-1} \\ 5.4 \cdot 10^{13}\,\mathrm{cm}^{-2}, & \text{for } T = 10^5\,\mathrm{K} \text{ or } b \approx 40.6\,\mathrm{km\,s}^{-1} \\ 1.7 \cdot 10^{14}\,\mathrm{cm}^{-2}, & \text{for } T = 10^6\,\mathrm{K} \text{ or } b \approx 128\,\mathrm{km\,s}^{-1} \end{cases} \tag{4.28}$$

Note that for $T \sim 10^4\,\mathrm{K}$ this equates to an EW of only $\sim$0.1 Å (using the linear regime approximation).

Square-Root Regime

At even higher column densities, the outer Lorentzian wings of the natural line broadening take over. This typically happens at much higher columns than the transition from the linear regime of the curve of growth to the flat regime. The width of the thermal broadening typically is of order $\mathrm{km\,s}^{-1}$; the natural line width of Ly_α, however, is about $9\,\mathrm{m\,s}^{-1}$—three orders of magnitude smaller. Numerical estimates show that they become relevant beyond column densities of about $10^{18}\,\mathrm{cm}^{-2}$ at a temperature of $10^4\,\mathrm{K}$ and even higher column densities for higher temperatures, which I rarely encounter in CGM of the simulations. Moreover, the approximation of optically thin gas typically breaks down at even lower column densities (for H I at above $\sim 2 \times 10^{17}\,\mathrm{cm}^{-2}$, see Churchill et al., 2015). The natural line width and resulting *damping wings* are nevertheless part of the PYGAD routines for generating mock absorption lines.

4.4.4 Generating Spectra from Simulations

The gas in the CGM is not homogenous in density, temperature, and ionisation states. Hence, the absorption spectra if the different transitions are not simply Voigt profiles. However, along each line-of-sight I can decompose the gas into several homogeneous elements, let us call them 'atomic gas elements', and calculate the spectra for these

atomic elements analytically using the theory presented above. Using Eq. (4.12) and (4.13) I then add up these individual 'atomic' spectra linearly to extract the full spectrum. The spectrum generation as explained in the following is implemented in the publicly available Python package PYGAD.

4.4.5 SPH Particles as Atomic Gas Elements (SPAGE)

As I am using SPH, the choice of the 'atomic' gas elements, i.e. the elements that are assumed to be homogeneous, might seem obvious: the SPH particles. I name this method SPAGE (*S*PH *p*articles as *a*tomic *g*as *e*lements). However, this choice is not perfect. Generally one might argue that only the SPH-smoothed fields are physically meaningful, not the properties of the particles themselves, because they would result in multi-valued fields already through SPH noise: the density, for instance, should generally have a single value at a given point in space, but a few dozen particles' kernels overlap with that point and they all can have (slightly) different densities (i.e. the SPH noise). In my case I even do not have a simple single-phase fluid nor do I have distinct phases; I rather have a continuous transition of many phases and a given particle does not belong to one phase exclusively (c.f. section 3.2). Therefore a multi-valued field is just consistent and a spectrum generation on a particle basis is the more natural approach.

A second issue with the generation from gas particles is that they do not include motions on sub-particle scales. There are generally two types of these motions: Hubble flow and sheer flows. Assume a particle with a diameter / smoothing length of $d = 100\,\mathrm{kpc}$. Then the Hubble flow over the size of the particle is $d{\cdot}H \simeq 7.2\,\mathrm{km\,s^{-1}}$, corresponding to a shift of $\Delta\lambda \approx 0.03\,\text{Å}$ for Ly_α. However, since particles with such large sizes firstly are rare and secondly have temperatures on the order of $10^6\,\mathrm{K}$, resulting in b-parameters of the order of $100\,\mathrm{km\,s^{-2}} \gg d \cdot H$, I ignore the Hubble flow over a single particle.

If two particles have a shear flow component, the gas in between them would move with an SPH-averaged velocity. Lets do the thought experiment of two overlapping particles with the same mass and smoothing length, and same but opposite velocities. The gas in the middle of their centres, would not move. If that point in space contributes to a spectrum, it is not redshifted. If I, however, take the spectra of the two particles and add them up, I end up with two lines: one redshifted, the other blue-shifted.

Finally, the SPH-average of fields has some freedom (cf. Hopkins, 2013). Moreover, a linear average of temperatures—even in the case of a single-phase SPH formulation—has the issue that the temperature varies over orders of magnitude

and the linear average of two values tends towards half the larger one in the case of two very different values (e.g. $(10^5\,\mathrm{K} + 10^4\,\mathrm{K})/2 \approx 0.5 \cdot 10^5\,\mathrm{K} \ll 10^4\,\mathrm{K}$). This situation is, of course, less pronounced in single phase SPH formulations, but even there it still occurs due to SPH-fluctuations, especially in the neighbourhood of shocks.

4.4.6 SPH-Smoothed Spatial Grid Cells as Atomic Gas Elements (GriCAGE)

An alternative to directly taking the SPH-particles as atomic gas elements for the spectra would be to first spatially bin the quantities of interest (T, n_{ion}, v_{los}, etc.) using the usual SPH-smoothing[5] and then take the bins as homogeneous gas elements. I will refer to this method as GriCAGE: (SPH-smoothed) *gri*d *c*ells as *a*tomic *g*as *e*lements.

This resolves the issues of missed Hubble and sheer flows, and might be more consistent with the classical interpretation of SPH, but makes it difficult to account for the multiphase nature of my code as it does not allow for different co-existing phases that absorb differently. Moreover, it is inconsistent with calculating the ionisation fractions on particle basis with their temperatures and densities but using the smoothed quantities for the spectrum generation.

The latter issue can, of course, be resolved by calculating the ionisation fractions on the spatial grid. However, as discussed, this alters the temperature and, hence, the ionisation fractions a lot (can be orders of magnitudes). The problem of averaging temperatures could be reduced by not averaging them directly, but the quantity I need for broadening, though: the square root of the temperatures.

Another issue is the binning itself. At a given point in space, the SPH-smoothed quantity is well defined. For an entire bin with spatial extent, I want typically want the average temperature and density in that bin. To the very least I would require the mass to be conserved. On an infinitesimal line that would require an integral[6], which is computationally demanding and the process of binning can introduce numerical uncertainties over the direct way of creating spectra for each particle.

4.4.7 Comparison of the Methods and my Fiducial Approach

There are pros and cons to both approaches, but as I am dealing with a multiphase code and artificially splitting the gas into distinct phases will either have to little

[5] In fact, there are two ways to smooth SPH values into a continuous field: the scatter and the gather approach. I use the scatter method here.

[6] For a spatially extended line there is a faster algorithm than doing the integral. See section 4.2.

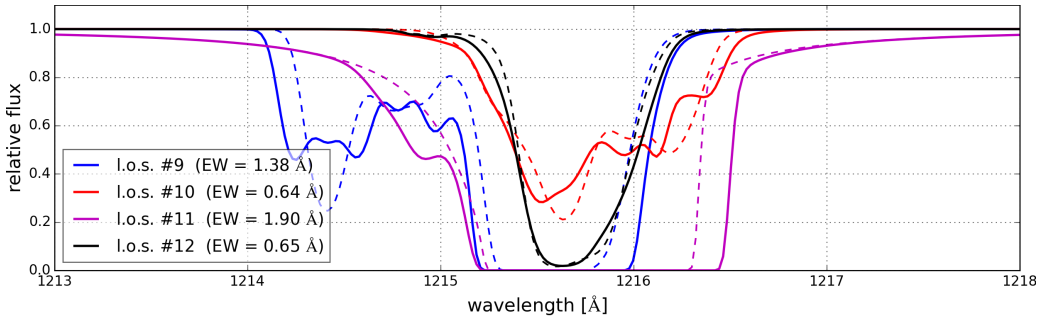

Figure 4.3: Mock Lyman-α absorption spectra of M0858 for lines #9 through #12 (cf. Fig. 5.3). Solid lines are generated by the fiducial SPAGE method and the dashed lines by the GriCAGE method (cf. text). Typically, the SPAGE method results in boarder lines in the saturated regions and more substructure in the line wings. The EWs (#9 through #12) are 1.38 Å (1.14 Å), 0.64 Å (0.62 Å), 1.47 Å (1.14 Å), and 0.65 Å (0.61 Å) for the SPAGE (and GriCAGE) method. Line #11 exhibits damping wings.

particles per phase to do a meaningful SPH-binning or to broadly taken phases, I choose to generate the spectra on a particle basis, i.e. using the SPAGE method: I calculate the τ-spectra in velocity space for each particle weighted with the kernel-integral along the line of sight, then add the spectra (utilising the linearity in the optical depths, Eq. 4.12 and 4.13) accounting for the velocities of the particles, including the Hubble flow. Finally the velocity bins of the spectrum are converted into the space of interest (e.g. wavelengths) and the flux spectrum is calculated via Eq. 4.13.

Again, I use the implementation of the spectra generation in PYGAD. Both methods are implemented and, in fact, it also allows to generate the spectra by a third approach, where there is binned like in GriCAGE but with with an extended column, i.e. a thick line of sight.

In Fig. 4.3, I show example absorption Lyman-α spectra of halo M0858 for different lines-of-sight with both methods. The solid spectra are generated with my fiducial SPAGE method; the dashed spectra are generated with the intermediate spatial binning onto the line-of-sight, the GriCAGE method. The general trend is that spectra with the SPAGE method show larger equivalent widths, often by 20% or more. These spectra were chosen to emphasise the difference between the methods, especially lines #9 and #10. More typical spectra are shown later in Fig. 5.6 and 5.5. Line #11, however, is a common example, where an additional absorption feature (at around 1215 Å) occurs next to the main line, which also grows significantly in

width when using SPAGE over GriCAGE.

Chapter 5

Results on Lyman-α Absorption

5.1 Motivation

Galaxies can grow by two different channels: the accretion of gas, that might eventually form stars, and the merging of already formed stellar structures such as other galaxies. It appears that major merger rates are low and most stars are formed in spiral galaxies (see Naab & Ostriker, 2016). It also seems that merger-triggered star formation is small and sometimes negligible (see e.g. Moster et al., 2011). Nevertheless, the in-situ fraction of Milky Way-like galaxies is predicted to be between only 5% (Moster et al., 2013) and 30% (Behroozi et al., 2013). However, a significant amount of stellar mass is formed by gas that was accreted onto the galaxy and it is this accretion process we know very little about observationally.

A crucial building block in the models of galaxy formation, thus, is the CGM as a reservoir of gas that can be accreted and, in fact, most gas is recycled multiple times: it is accreted, might form stars, of which some explode as SNe and often expel the gas, it can be accreted again, and the cycle starts over again (see e.g. Christensen et al., 2016, Übler et al., 2014). This continuous recycling and especially the resulting sustained flow of new gas is needed for the creation of spiral galaxies as we know them today (see e.g. Oppenheimer et al., 2010).

Virtually the only way we can observe the CGM is by absorption of QSO light. The findings of observations (and simulations) has been outlined in chapter 2: although the metals are associated with galaxies (typically column densities fall exponentially), different ions reach out to different distances and have different covering fractions that can be very low even for small impact parameters as such for Mg II, indicating a non-smooth distribution. Some lines have a dependence of the azimuthal angle (such as, again, Mg II) indicating that they trace in- and/or outflows, though

this dependence is not so clear for some ions such as H I. The different ions trace different phases in temperature and density. Churchill et al. (2015) showed that these cases them to trace physically distinct regions—highly questioning the metallicity measurements of the CGM derived from QSO absorption line observations—and that the commonly used models for fitting lines and deriving gas properties (Voigt profile (VP) decomposition and apparent optical depth (AOD) measurements) can lead to totally wrong measurements of temperatures and even column densities of the gas.

Churchill et al. (2015), however, have used only a single AMR simulation of a dwarf galaxy ($M_{\rm vir} = 3\times10^{10} M_\odot$, at $z = 0.5$). I will here investigate the nature of the absorption lines with a good dozen zoomed-in simulations described in chapter 3 with virial masses in the range $10^{11.6}\,M_\odot - 10^{12.5}\,M_\odot$, keeping a relatively high resolution that is needed for the CGM (see e.g. Crain et al. (2017)).

5.2 Results for H I and Lyman-α Lines

I applied my fiducial method (SPAGE) for generating absorption line spectra to all of my simulations. In the following I will present and discuss my findings with the representative example of halo M0858 with a focus on the disc-halo interface, i.e. within a few times the H I disc size, $R_{\rm HI}$.

5.2.1 Large Scale Picture

For halo M0858 I create a regular grid of 200×200 equally spaced sight lines along the x-axis. For each sight line I generate a mock Lyman-α spectrum with my fiducial method and calculate the corresponding equivalent width (Eq. 4.21). The result is presented as a two-dimensional map of EWs in Fig. 5.1 alongside a map of the H I column densities, the H I line-of-sight velocity dispersions, and a map of the mean H I-mass weighted temperatures.

Overall, the structure of the EW map is well correlated with the column densities. Regions of large EW correspond to regions of enhanced HI column densities. In this projection, for example, the accreting neutral gas filaments are clearly seen in the EW map stretching out to the west and east.

The reason for this correspondence is that at such low column densities ($\lesssim 10^{14} - 10^{15}\,{\rm cm}^{-2}$) the absorption lines are still in the linear regime of the curve of growth (cf. section 4.4.3) (and in the transition to the logarithmic regime) and thus the EWs are largely proportional to the column density (see left panel of Fig. 5.2). In the central region, discrepancies between the equivalent widths and the column densities emerge.

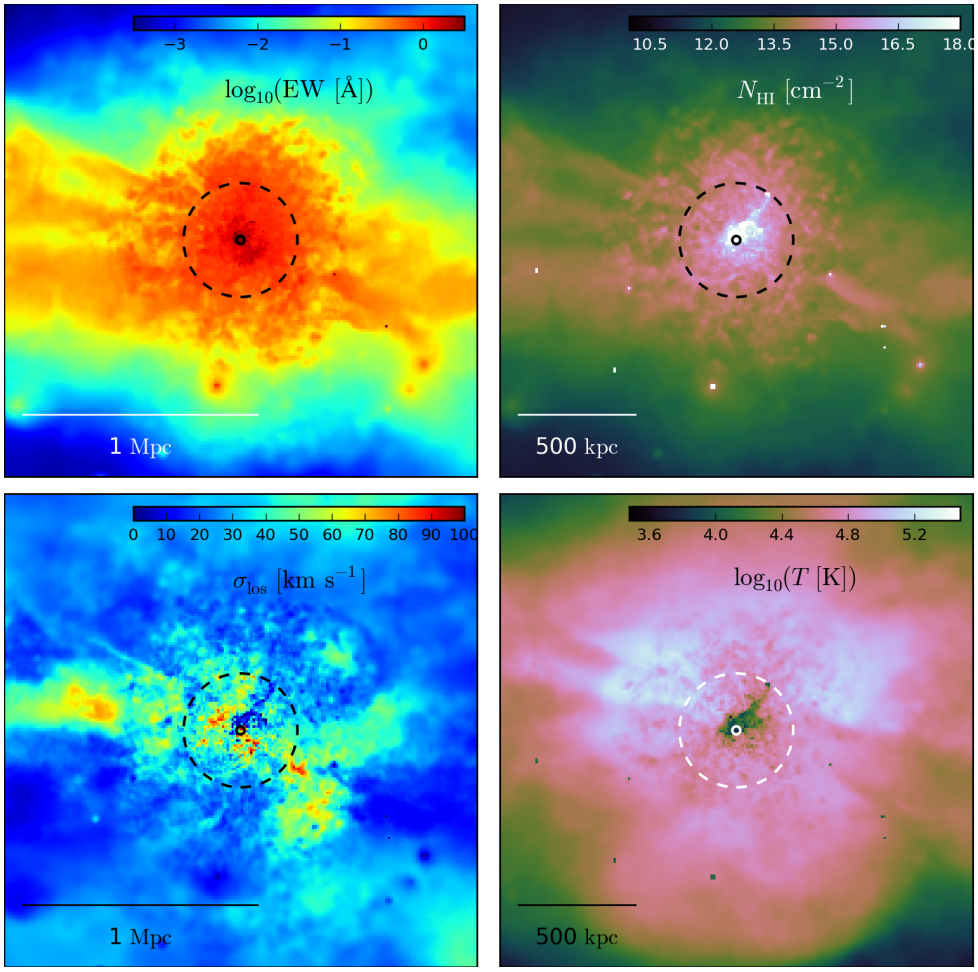

Figure 5.1: A side-on projection of M0858, 2 Mpc wide: The top left panel shows the Lyman-α EWs for 200×200 (infinitesimal thin) equally spaced sight lines through the simulation domain; the panel to the right shows the column densities of HI; the bottom left panel shows the HI gas (mass weighted) velocity dispersion; and the bottom right panel shows the HI (mass weighted) gas temperature. The small solid circles indicate the HI disc size; the dashed circles enclose R_{200}. Except for the very dense inner part (see also Fig. 5.3) the EWs resemble the image of the column densities very well (cf. Fig. 5.2). However, the dense region (small satellite at $\sim R_{200}$, top right) has no corresponding feature in the EW map (top left) as the line-of-sight velocity dispersion is very low (bottom left, see also Fig. 5.3).

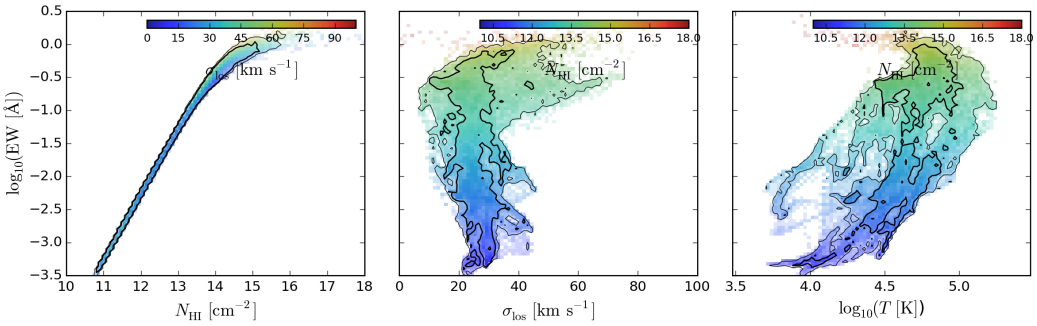

Figure 5.2: The correlations of the EW from the maps of Fig. 5.1 with column density (left panel), HI line-of-sight velocity dispersion (middle panel), and the HI temperature (right panel). The colour coding for the column density and mean velocity dispersion scales with velocity dispersion and column density respectively, the brightness scales with the number of lines-of-sight. The colour bar in the right panel scales with velocity dispersion. The column densities for most lines-of-sight are in the linear part of the curve of growth—as can be seen by the tight line in the left panel—and transition into the flat regime at around $10^{14}\,\mathrm{cm}^{-2}$. Also line-of-sights with higher EW tend to have higher velocity dispersion and temperature.

Here the linear regime of the curve of growth is also left at around $\sim 10^{14}\,\mathrm{cm}^{-2}$ (cf. Eq. 4.28). In particular the dense satellite and its gaseous connection to the main galaxy (visible in the north east of the upper right panel of Fig. 5.2) do not show up in the EW map. In the velocity dispersion and temperature map, however, it is clearly visible as a coherent and cold feature.

Besides the tight correlation of EW with the column density I also find a clear correlation with temperatures as can be seen in the right panel of Fig. 5.2. I would like to argue that this correlation is not due to the fact that the gas temperate increases the b-parameter and therefore broadens the line, but it is mainly a secondary effect of the correlation with column density. In fact, for the highest EWs (EW $\gtrsim 0.3\,$Å), temperatures start to decrease with larger EWs (also can be seen more clearly in Fig. 5.4). As in the outer parts of the halo and beyond R_{200}, the gas behaves roughly adiabatically, smaller densities imply smaller temperatures. Hence, the correlation of EW with temperatures is secondary to the correlation with the column densities.

The fact that the gas behaves almost adiabatically can be shown by comparing the cooling times with the dynamical times. Following Mo et al., 2010 (Eq. 8.94) I

calculate the cooling times $t_{\rm cool}$ for each particle:

$$t_{\rm cool} \simeq 3.3\,{\rm Gyr} \times \frac{T/10^6\,{\rm K}}{(n_H/10^{-3}\,{\rm cm}^{-3}) \times (\Lambda/10^{-23}\,{\rm erg\,cm^3\,s^{-1}})}. \quad (5.1)$$

For the cooling rates Λ I use the same tables from Wiersma et al., 2009 as I do for the simulations themselves. With a definition of the dynamical times as $t_{\rm dyn} = \frac{R_{200}}{|\vec{v}|}$, I find that more than a fourth of the particles at around R_{200} in halo M0858[1] have at least a ten times larger cooling time than dynamical time and the median value for the ratio is: $t_{\rm cool}/t_{\rm dyn} = 2.3 > 1$. Hence, most of the gas behaves adiabatically. Note, however, that the gas does not actually need to be adiabatic.

5.2.2 Absorption at the Disc-Halo Interface

In Fig. 5.3, I zoom into the central region of Fig. 5.1 and more closely investigate absorption features to the disc-halo interface (the HI disc size is indicated by the solid circle) where the tight correlation of column densities and EWs breaks down. I again create mock absorption line spectra along 200×200 l.o.s. and also show HI column densities, velocity dispersion and temperature. The typical column densities in this region are in the logarithmic regime where the linear correlation between equivalent width and column density no longer holds. In this regime the structural similarity of the column density and EW maps break down. The dense, arc-like, tidal feature in the north-east appears as a kinematically coherent and cold feature with a velocity dispersion of the order of the expected sound speed (bottom left and right panels of Fig. 5.4). It is, however, almost completely absent in the EW map (top left panel of Fig. 5.4). Only at small regions where the column densities exceed $\sim 10^{19}\,{\rm cm}^{-2}$, the EWs are elevated as the square-root regime is met. Instead, the EWs are enhanced in the south-east, a region with low column density warm gas ($T \sim 10^{4.6}\,{\rm K}$) but enhanced line-of-sight velocity dispersion ($\sigma_{\rm los} \sim 80\,{\rm km/s}$).

As the logarithmic regime of the curve of growth is entered (see left panel of Fig. 5.4) the EWs now only weakly depend on column densities. In the ideal world of homogeneous gas, the EWs would almost linearly depend on the b-parameter (in my model purely the thermal broadening, cf. Eq. 4.26). The temperature to large extent is determined by the densities, though (higher density gas have lower temperatures and larger EWs, right panels of Fig. 5.4, because as the gas cools, it also condenses into dense structure). However, also the temperature map is not correlated with the EW map (cf. Fig. 5.3). Indeed, the correlation between these two quantities is poor

[1] I allow for 5% variation, yielding about 12,500 particles.

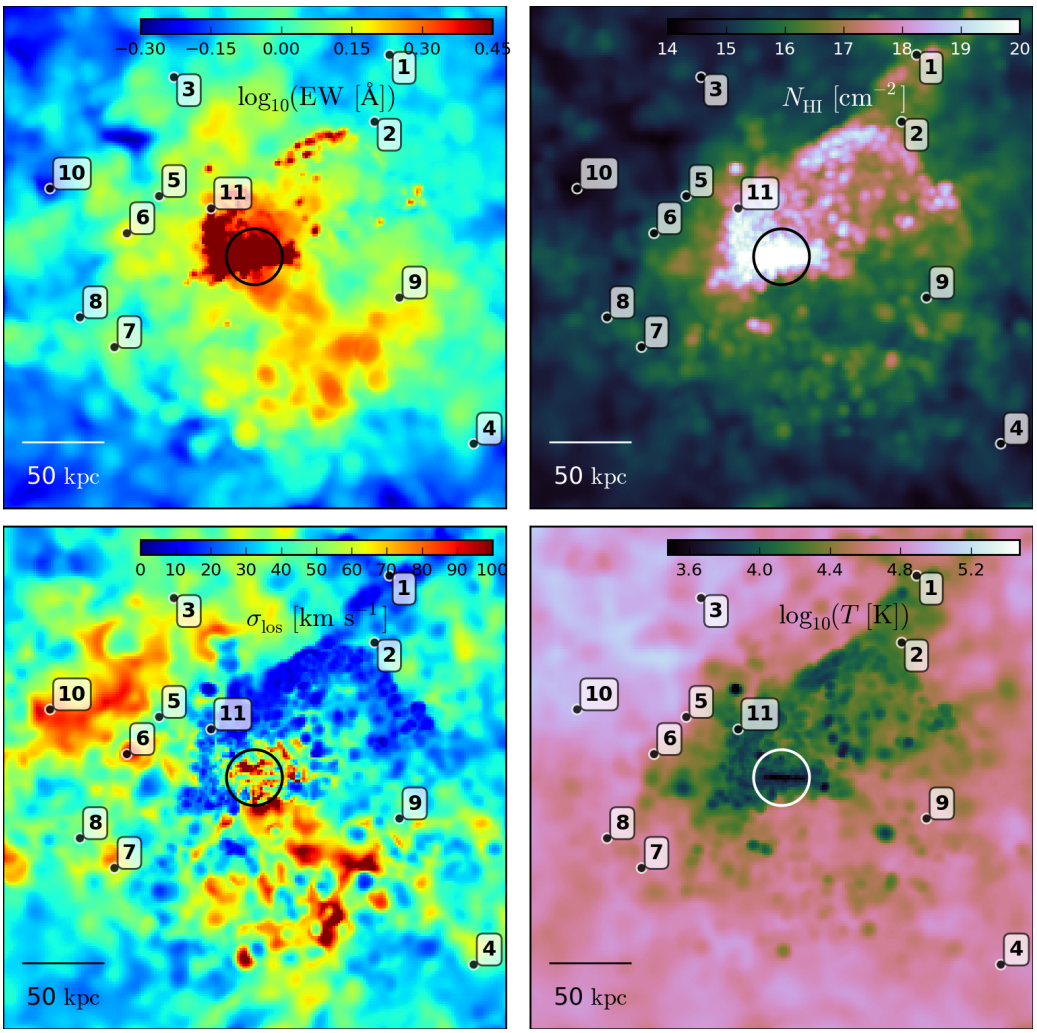

Figure 5.3: The same side-on projection of M0858 as in Fig. 5.1 but with 306 kpc on a side. Again: the upper right panel shows the column densities of HI; the upper left panel shows the Ly$_\alpha$ EWs; the lower left panel shows the H I gas velocity dispersion; and the lower right panel shows the mean HI mass weighted gas temperature. The EW in the intermediate dens regions ($\sim 10^{15} - 10^{18}\,\mathrm{cm}^{-2}$)—where we left the linear part of the curve of growth and entered the 'flat part'—does not depend (much) on the column density, but mostly on the line-of-sight velocity structure largely captured by the velocity dispersion. The sample spectra of Fig. 4.3, 5.6, and 5.5 are indicated in with numbers next to them.

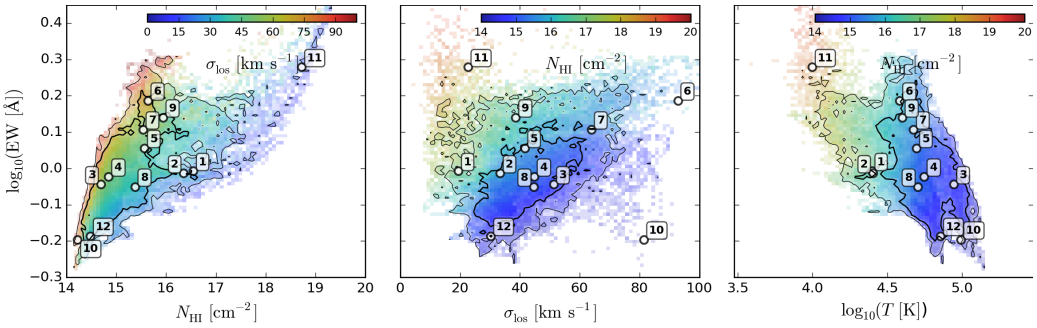

Figure 5.4: The pixel-wise correlations of the EW from the maps of Fig. 5.3. I have colour coding for the mean velocity dispersion or column density of the pixels, and the pixels' luminosity scales with the number of sight lines. As I am here leaving the linear part of the curve of growth ($\gtrsim 10^{14.5} - 10^{15}\,\mathrm{cm}^{-2}$), the line-of-sight velocity structure dominates the EW (not so much the temperature, since it is well correlated with the densities).

and it even is an anti-correlation (see Fig. 5.4). One can, however, see a correlation of the l.o.s. velocity dispersion and EW (middle panel of Fig. 5.4, note that most l.o.s. lie on the diagonal from bottom left to upper right as highlighted by the contours).

From Fig. 5.4 one can see the following trend: at a given column density the EW is larger for sight lines with higher velocity dispersion. For example at $N_{\mathrm{HI}} \sim 10^{16}\,\mathrm{cm}^{-2}$ the EWs range from $\log_{10}(EW/(1\,\mathrm{\AA})) \approx -0.1$ for gas with $\sigma_{\mathrm{los}} \approx 10\,\mathrm{km/s}$ to $\log_{10}(EW/(1\,\mathrm{\AA})) \approx 0.3$ for gas with $\sigma_{\mathrm{los}} \approx 80\,\mathrm{km/s}$ (left panel). At a given velocity dispersion, higher column density gas has lower EWs (middle panel). At high EWs ($\log_{10}(EW/(1\,\mathrm{\AA})) \approx 0.2$) the gas covers almost the whole temperature range (from $T \sim 10^4\,\mathrm{K}$ to $T \sim 10^5\,\mathrm{K}$), low EW sight lines are dominated by higher temperature gas ($T \sim 10^5\,\mathrm{K}$). This occurs due to the low column density regime ($\lesssim 10^{15}\,\mathrm{cm}^{-3}$). Such l.o.s. reside in the halo well outside the disc, where there is very little cold gas. Or in other words: low-temperature gas (almost always) has high densities (mainly because of cooling) and, hence, high column densities, too. The latter results in high EWs.

To investigate these trends in more detail I marked four sight lines with very similar column densities of about $10^{15.6}\,\mathrm{cm}^{-2}$, namely lines five through eight in Fig. 5.3 and 5.4. The spectra are shown in Fig. 5.5. Spectrum number eight has the lowest EW of 0.90 Å with a velocity dispersion of $\sim 45\,\mathrm{km\,s}^{-1}$, whereas line number six has an equivalent width of 1.53 Å and a σ_{los} of almost $\sim 100\,\mathrm{km\,s}^{-1}$. This is an example for the typical case where the velocity dispersion generates a large EW despite an unchanged column density.

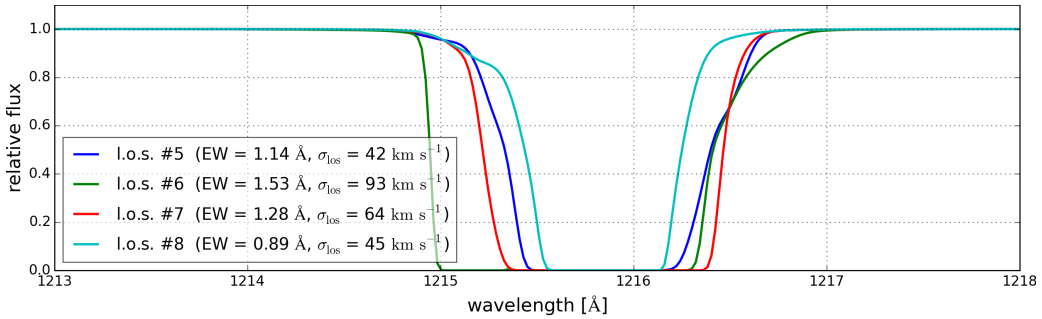

Figure 5.5: Lyman-α absorption spectra for lines #5 through #8 as marked in Fig. 5.3 (cf. also Fig. 5.4). All lines have similar column densities of about $10^{15.6}\,\mathrm{cm}^{-2}$, but varying EWs due to their different l.o.s. velocity structure (see text).

Similarly, I have marked lines one through four (and line eight) all with very similar equivalent widths (of $\sim$0.95 Å) but different column densities. The spectra are shown in Fig. 5.6. The (weak) dependence of the equivalent widths would suggest raising EW with raising column densities. This trend is compensated both, by temperatures and velocity dispersion. Since the former are anti-correlated with the column densities, higher column densities tend to have smaller temperatures and thus their b-parameters compensates the natural trend with column densities, because the EW of the already saturated lines is dominated by the b-parameter. Furthermore, here the lines with smaller column densities have higher velocity dispersions, adding additional equivalent widths. Finally, all of the chosen four (five) lines have very similar EW despite their very different column densities.

5.2.3 Velocity Structure and Line Shapes

I have shown that the gas velocity structure along each line-of-sight can play an important role for the determination of the EWs at the disc-halo interface, where the Lyman-α column densities and equivalent width are high enough to be in the logarithmic regime of the curve of growth (cf. Fig. 5.4 and Eq. 4.28). In my simulations this happens out to a few HI disc sizes, so almost everywhere within the halos (within R_{200}) of the galaxies. A single broad absorption line is typically not arising form a single homogeneous clump of gas (as I will show in the following), but typically by a superposition of many absorbing clumps of a continuum of gas with spatially varying properties such as exponential density and temperature profiles of gas in a virialised halo.

The line spectra of the already discussed sight lines are plotted in Fig. 5.5 (#5 -

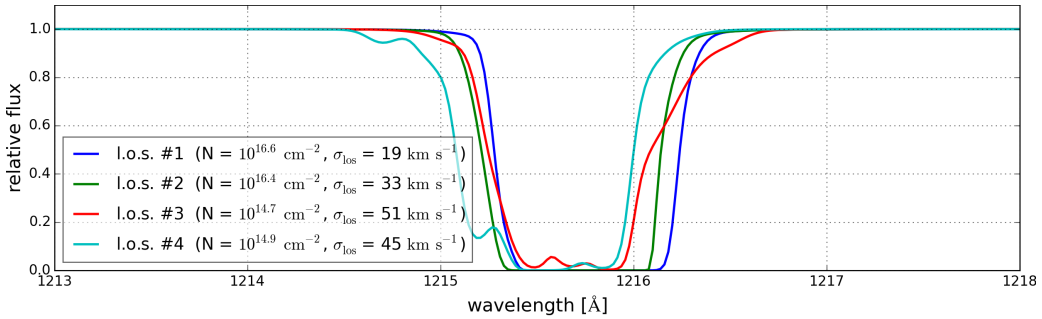

Figure 5.6: Lyman-α absorption spectra for lines #1 through #4 as marked in Fig. 5.3 (cf. also Fig. 5.4). The lines have similar EWs (~ 0.95 Å), but different line-of-sight velocity dispersions. In general the broadening due to line-of-sight dispersion effects / the composition of different lines cannot be seen as the lines are saturated. For a few cases, like line #4, weak separate lines can appear (at $\sim$1215.1 Å).

#8), Fig. 5.6 (#1 - #4), and Fig. 4.3 (#9 - #12). The lines have impact parameters between $2\,R_{\rm HI}$ and $11\,R_{\rm HI}$ at HI column densities of $10^{14}\,{\rm cm}^{-2}$ to $10^{17}\,{\rm cm}^{-2}$ (and one at $10^{19}\,{\rm cm}^{-2}$). Most lines are saturated and have EWs of more than 0.8 Å. (The only exceptions are lines #10 and #12 with EWs of ~ 0.6 Å.) In the chosen lines, I rarely find internal structure in any Ly$_\alpha$ absorption line. That implies that it is mostly not possible to distinguish between the different possible origins of the high column densities. There could be a) a high column density, b) a high temperature / b-parameters, or c) a high velocity dispersion / clumps at different l.o.s. velocities which lines are blended into another due to their proximity and width. Sometimes the lines exhibit wings or even distinct secondary lines, that often are interpreted as outflow features (such as for lines #4 and #11). Seldom—even for the broad lines—these actually arise from damping wings.

Only in few cases (e.g. lines #9 and #10) one can see more complex line shapes, often composed out of several resolved lines. It is, however, difficult to interpret these structures physically. Firstly, because it strongly depends on the chosen method to generate the lines (SPAGE or GriCAGE), making it dependent on the interpretation of the multiphase simulations. Secondly, they often arise from single SPH particles, indicating that my resolution is not sufficient for generating these structures / additional lines.

In Fig. 5.7 I show the distribution of the HI column density in phase space along the sight line #9 covering 400 kpc and about 400 km s^{-1} in velocity space, alongside with the total spectrum as well as those of the just the gas in the marked (blue and green) regions. Most of the mass is at positions between $x = 0$ kpc and $x = 100$ kpc

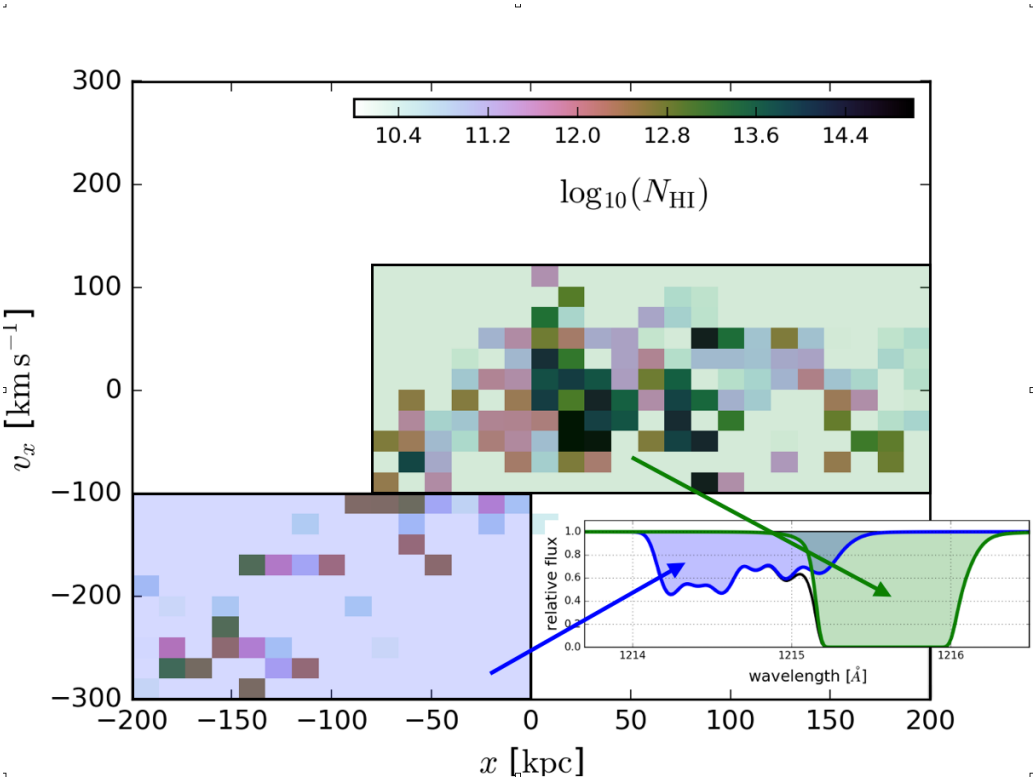

Figure 5.7: The column density distribution along the line of sight number 9 (cf. Fig. 4.3, 5.3, and 5.4) and as a function of its velocity and position along the line of sight. In the 2D-histogram the amount of column density in each pixel is colour coded. In the inlayed spectrum of the line (cf. Fig. 4.3) I separated the HI mass by its position and velocity as indicated by the coloured regions in the phase space and created spectra of just that mass. The mass extending towards negative positions and velocities (light blue square) created the left wing (also light blue) in the spectrum, whereas the rest creates the main line.

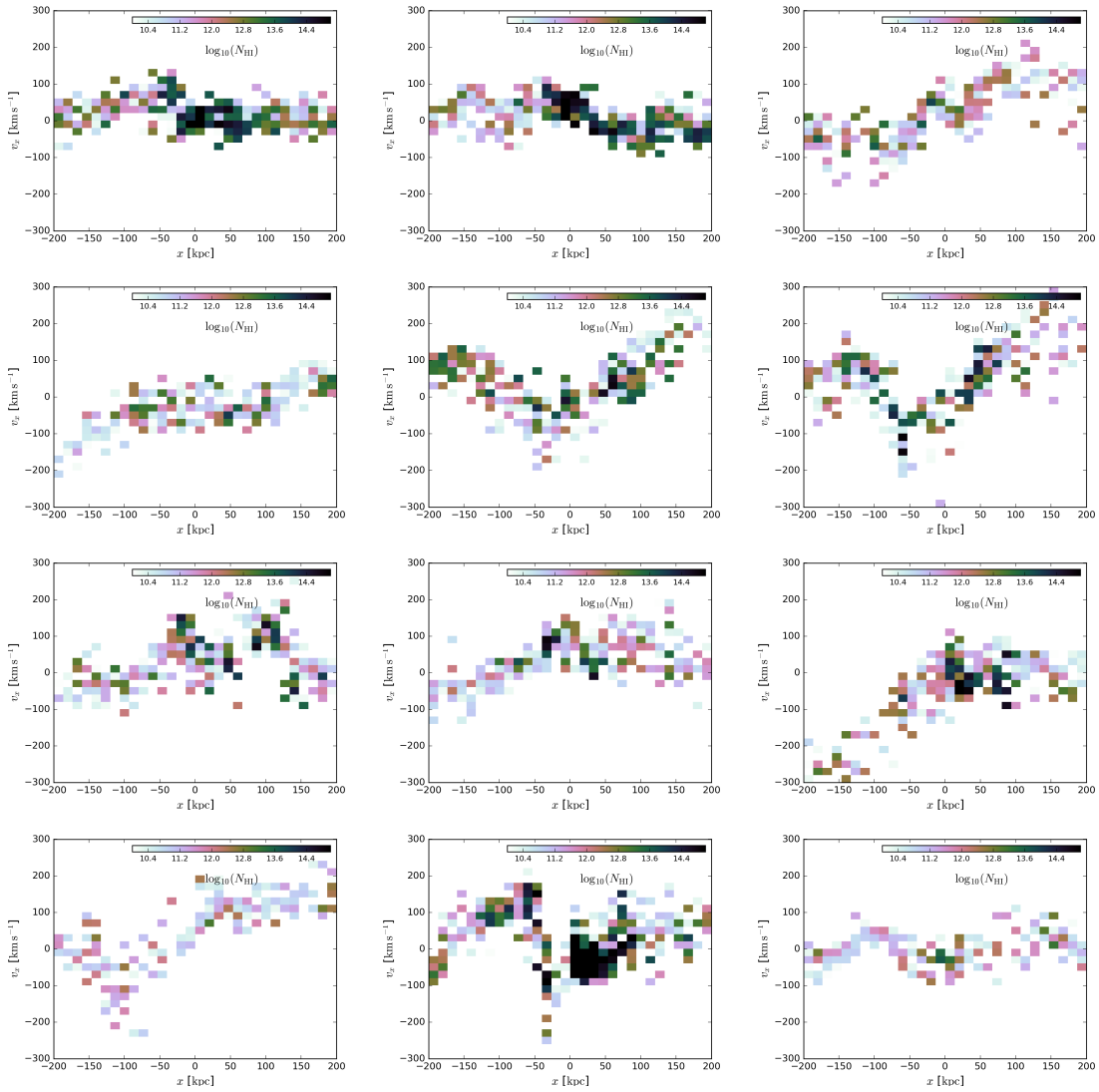

Figure 5.8: Similar to Fig. 5.7 we show the column density distribution along the lines of sight and as a function of its velocity and l.o.s. position. Colour coded is the amount of column density in each pixel. Shown are the distribution of all 12 lines that are marked in Fig. 5.3 with their spectra shown in 5.6, Fig. 4.3, and 5.5. The panels are ordered by line numbers in western reading order, i.e. from top left to bottom right.

along the line of sight with velocities of less than $100\,\mathrm{km\,s^{-1}}$, which equates to a total shift of about 0.4 Å—a bit less than its EW. However, towards negative positions there is some mass with l.o.s. velocities of down to about $-300\,\mathrm{km\,s^{-1}}$, explaining the wing of a width of ~ 1 Å in the spectrum towards smaller wavelengths (present in both methods, SPAGE and GriCAGE).

Let us concentrate on the phase space distributions of lines six (right panel in second row of Fig. B.1) and eight (middle panel in third row of Fig. B.1). Recall that these two lines both have a total HI column density of about $10^{15.6}\,\mathrm{cm^{-2}}$ and also similar (averaged) temperatures of 40 000 K to 50 000 K (equating to a b-parameter of roughly $25\,\mathrm{km\,s^{-1}}$). Still, the equivalent widths of line #6 is about 0.75 Å larger that that of line #8.

Looking at the line-of-sight phase space distribution of the two lines, I find that line eight has a narrow distribution in velocities and is centred at $x \approx 0\,\mathrm{kpc}$, whereas the distribution of line six has a somewhat V-shaped distribution. One arm extents from around $(-150\,\mathrm{kpc},\ 100\,\mathrm{km\,s^{-1}})$ to roughly $(-50\,\mathrm{kpc},\ -150\,\mathrm{km\,s^{-1}})$; the second one stretches from there to about $(50\,\mathrm{kpc},\ 120\,\mathrm{km\,s^{-1}})$, where most of the mass sits.

These two arms of the V of line six come from the complex halo gas distribution, driven by the still circling gas remnants of the merger almost 2 Gyr ago and/or a smaller fly-by about 1 Gyr ago. This spatial and kinematic structure, however, cannot be seen in the line spectrum (see Fig. 5.5) as it is too saturated. It only has an enlarged width. The only hint might be the extended wing on the right hand side. That, however, is neither universal in such scenarios nor are these wings missing in other lines, for which the mass is mostly confined in one compact region in phase space, such as number eight. (See also appendix Fig. B.1 for the space distribution of all shown lines).

5.2.4 Radial Equivalent Width Profiles

Observationally one is restricted to sight lines where there is actually a QSO in projection close to a galaxy. This makes it impossible to measure entire maps of absorption lines like presented in this work, but with several different QSOs and galaxies one can still find observational radial trends of the EWs. In Fig 5.9 and 5.10, I compare the observations presented in Borthakur et al. (2015) (having redshifts of $0.025 < z < 0.05$) to those I obtain from each halo at random orientations (at $z = 0$). For each radial bin of 5 kpc I tested 20 random orientation with 30 random l.o.s., yielding more than $20,000$ lines for each profile.

When comparing individual halos with an entire ensemble (the combined profile will be discussed below, cf. Fig. 5.11), one should not expect that each halo can

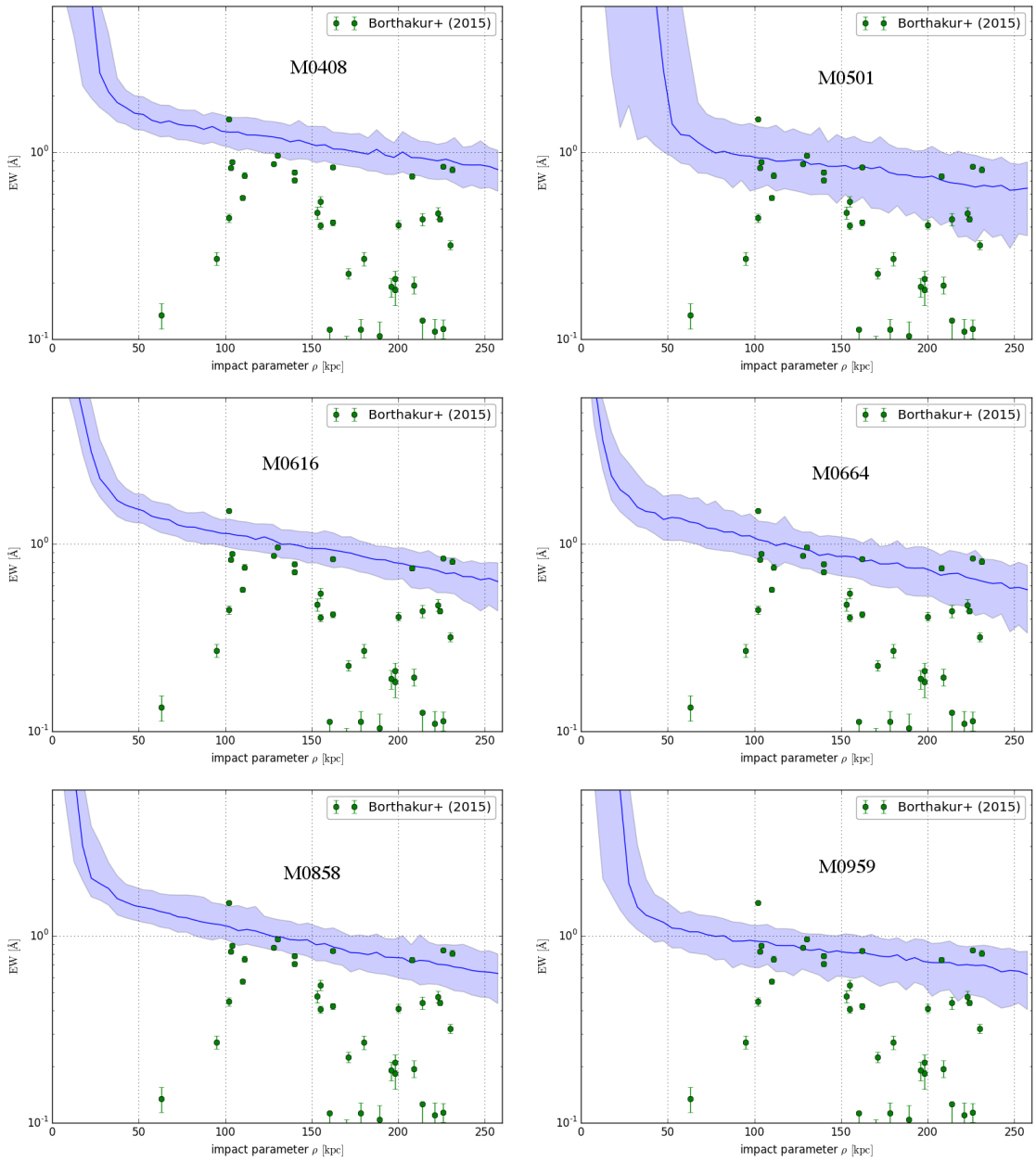

Figure 5.9: Profiles for halos M0408, M0501, M0616, M0664, M0858, and M0959 (from top left to bottom right) as generated from many random orientations for each halo. The blue line is the median EW for each radial bin of 5 kpc width and the light-blue band indicated the 10%ile and 90%ile in these bins. For comparison the observations as presented by Borthakur et al. (2015) ($0.025 < z < 0.05$) are plotted in green.

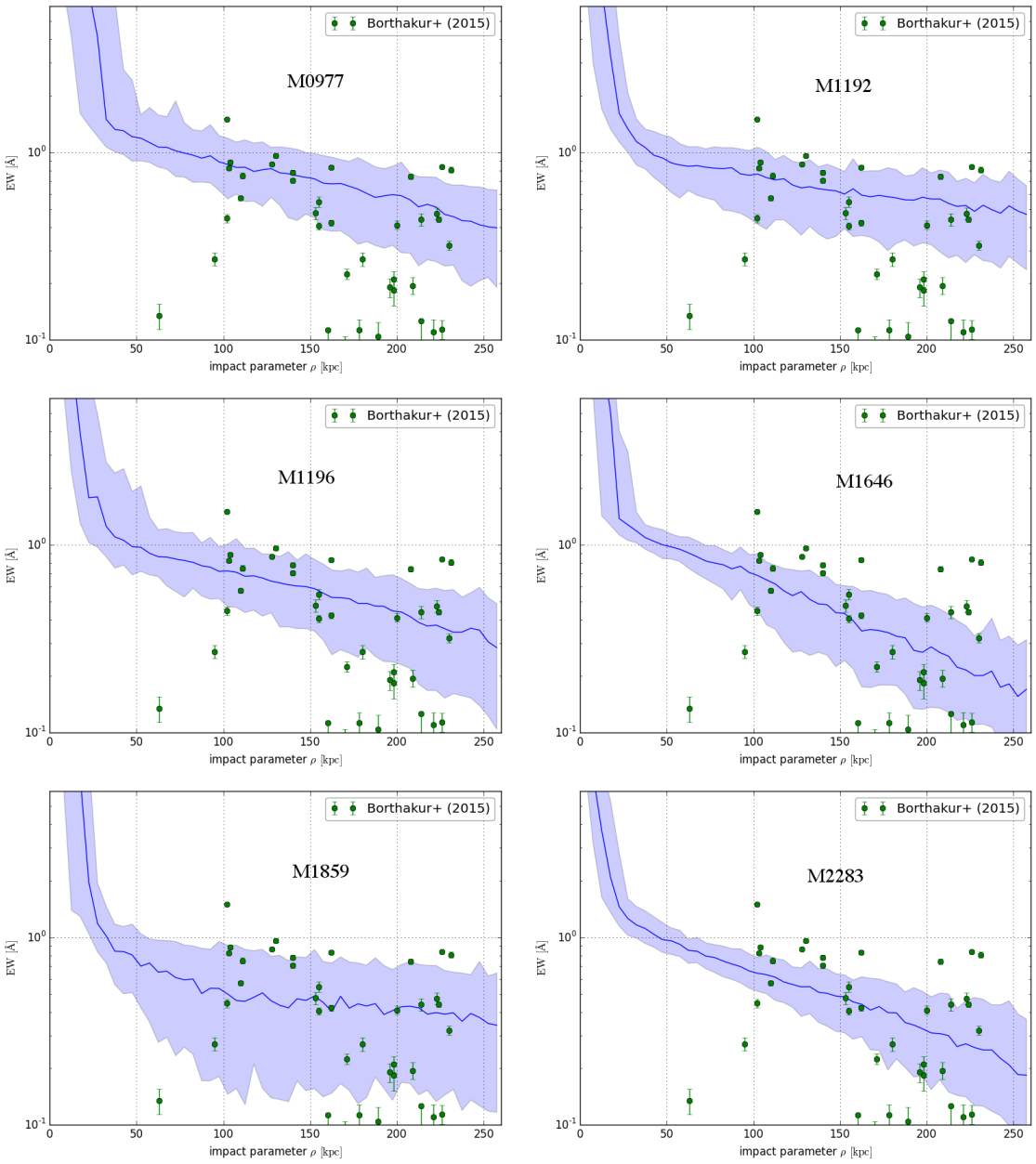

Figure 5.10: Profiles for halos M0977, M01192, M1196, M1646, M1859, and M2283 (from top left to bottom right) as generated from many random orientations for each halo. The blue line is the median EW for each radial bin of 5 kpc width and the light-blue band indicated the 10%ile and 90%ile in these bins. For comparison the observations as presented by Borthakur et al. (2015) ($0.025 < z < 0.05$) are plotted in green.

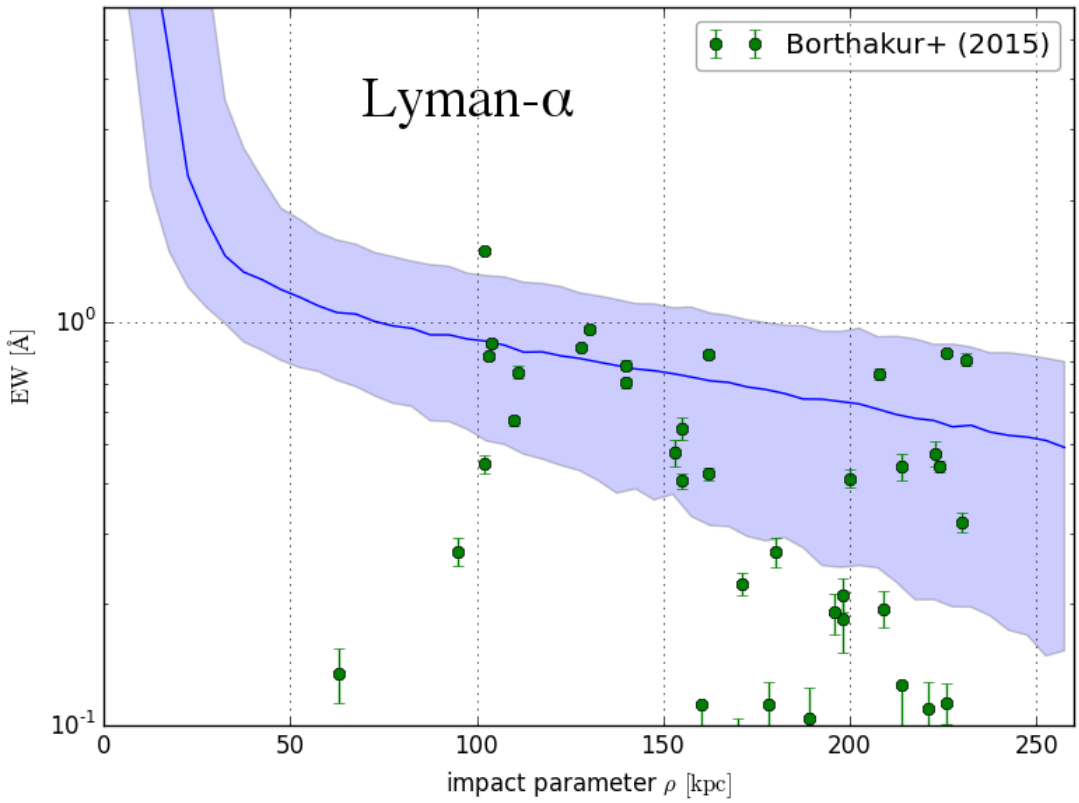

Figure 5.11: The blue line is the median EW for each radial bin of 5 kpc width and the light-blue band indicated the 10%ile and 90%ile in these bins of the Ly$_\alpha$ EWs of all 12 simulations combined. For comparison the observations as presented in Borthakur et al. (2015) ($0.025 < z < 0.05$) are plotted in green.

explain the entire observations. Still, the most massive halos (Fig. 5.9) explain the stronger Ly$_\alpha$ lines fairly well and the lighter ones (Fig. 5.10) progress to the lower observed (rest-frame) EWs, also explaining the smallest ones (although they are in the lower 10%ile and only M1859 gets actually close the smallest EWs). However, the observational sample has galaxies with stellar masses in the range $10^{10} - 10^{11}\,M_\odot$ with a median mass of $2.5 \cdot 10^{10}\,M_\odot$ and my simulations have stellar mass of $10^{9.9} - 10^{11.2}\,M_\odot$ with a median mass of $4.2 \cdot 10^{10}\,M_\odot$. Considering the trend of the Lyman-α EWs with the halo masses, it is therefore plausible that the simulations show slightly higher EWs.

Actually, combining the simulations EWs into one profile yields the relation shown

in Fig. 5.11. Even though most observations are within the 10%ile and the 90%ile, more than just 20% of the observations are off, mainly below the simulations' scatter and at larger impact parameters ($\gtrsim 150\,\mathrm{kpc}$). Also, the median of the observations lies slightly lower than the one of the simulations. At around 200 kpc the observations' median is almost 0.5 dex below the one from the observations, whereas between $\sim 100 - 150\,\mathrm{kpc}$ it is virtually spot on. As a result, the profile from the simulations is flatter than the observed profile.

It should be kept in mind though, that the observation sample (45 lines) and especially the simulation suite (12 halos) are limited in numbers. Considering halos M1646 and M1859 (middle right and bottom left panels in Fig. 5.10), the low EWs at larger radii are not that unusual. Considering that the stellar mass median of my simulations is more than 0.2 dex higher than the one of the ensemble, the tension (also of order 0.2 dex) to the data is not very large. The relatively higher EWs in the simulations still might point towards a not well enough resolved CGM, missing some of a potential small scale structure and clumpiness, that could open some lines with small column densities and, hence, small EWs.

Another explanation might be that the EWs scale with the H I disc size, R_{HI}, as Borthakur et al. (2015) found. As their ensemble has a median R_{HI} of 16 kpc and my simulations have a median R_{HI} of 20 kpc. This also would scale my results towards lower EWs and closer to the observed data and is also plausible when seen in the context of the H I masses of my simulations that are slightly higher (when compared to the stellar masses) than observed (cf. Fig. 3.4).

It might also be that the EWs actually do not scale with the physical distance to the halo's centre, but with the distance normed to the virial radius as gravity is probably the dominating factor in shaping the H I density profiles and thus also the EW profiles. In Fig. 5.12 I show the radial profiles—now edge-on—of all my seven halos, that do not have a (large) merger (see also Tbl. 3.1), out to about R_{200} as well as a plot to larger radii for halo M0858. Again, I compare to the results from Borthakur et al. (2015) but now scaled to R_{200}.

In Fig. 5.12 I also show angular dependences of the EWs. That will be discussed in the next chapter. Still focusing on the radial trends for now, it can be seen that the overall picture does not change significantly. The EWs of the simulations are still slightly too large and the tension between the simulations and the data is not resolved.

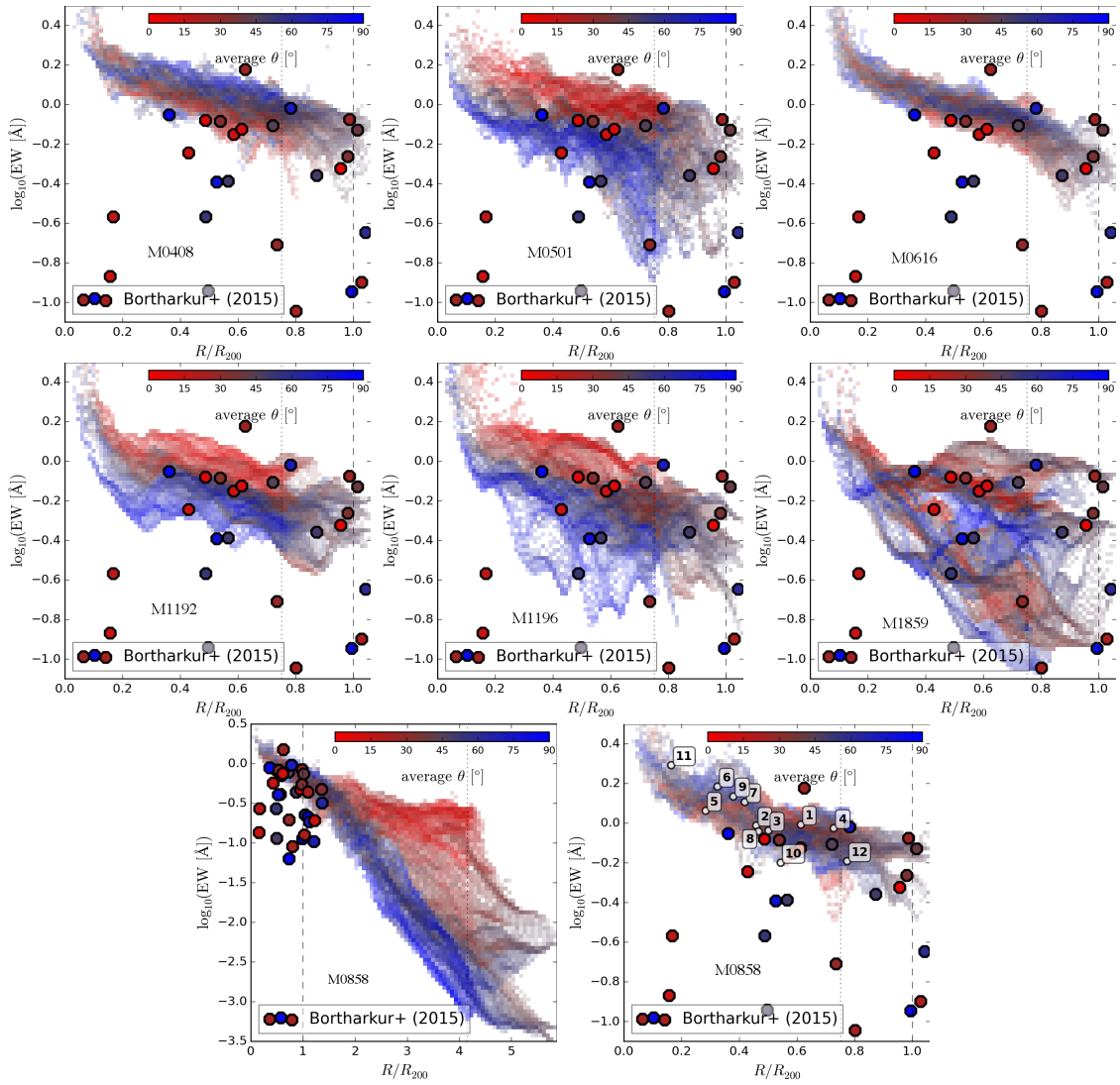

Figure 5.12: The equivalent widths of the Ly-α lines for the non-merging halos are plotted as a function of their normalised impact parameter R/R_{200} in edge-on projection. From top (left) to bottom (right) the profiles are for halos M0408, M0501, M0616, M1192, M1196, M1859, M0858 large scale (cf. Fig. 5.1), and M0858 small scale (cf. Fig. 5.3). Additionally there is a colour coding by the (average) angle (of the pixels) to the major axis (i.e. 0° is in the disc plane). The dotted lines are half the side length of the maps from which the profiles were created. The hexagonal data points are taken from Borthakur et al. (2015) and are also scaled to R_{200} and colour-coded by angle (data from face-on projections are not included).

5.2.5 Angular Dependence of the Equivalent Widths

Lyman-α equivalent widths might not only show a trend width radius but also with azimuthal angle. One might assume that the gas condenses preferentially in the plane of the disc onto the disc, and thus one would expect higher equivalent widths following the larger HI column densities. As I have discussed previously, in the disc-halo interface the correlation between those two quantities is not very strong as at the relevant radii the EWs and column densities are in the logarithmic regime of the curve of growth. In order to investigate how this effects a potential angular dependence, I have the (edge-on) profiles in Fig. 5.12 colour coded with the (mean) angle to the disc plane (the brightness scales with the number of sight lines).

Well beyond the virial radius the Lyman-α equivalent widths follow the density structure well as the densities are low enough to be in the linear regime of the curve of growth. M0858 is a good example of this situation as there are two cosmic filaments aligned with the disc plane (in the projection I have chosen, cf. Fig. 5.1). This results in two branches of the profiles: one with equivalent widths in the range of $10^{-0.8}$ Å to $10^{-0.5}$ Å, close to zero degrees to the disc plane and another one with exponentially falling widths (down to less than 10^{-3} Å) close to perpendicular to the disc plane.

Close to the disc, i.e. in the CGM and disc-halo interface, I see about half of the (non-merging) galaxies having an angular dependence of the EWs: M0501, M1192, and M1196 clearly have higher EWs in the disc plane (though outside the disc) than perpendicular to it (in Fig. 5.12 seen by the blue parts having higher EWs); the most massive galaxy M0408, however, shows a somewhat weaker opposite behaviour; and the three remaining galaxies have no angular dependence. In the observational data from Borthakur et al. (2015), however, there is no clear trend with azimuthal angle seen.

Those three galaxies that do show an angular dependence live in a quiet environment with no signs of passed mergers (cf. Fig. 5.13). For those, the gas condensates primarily in the disc plane leading to the large EWs. Due to the undisturbed environment, the velocity dispersion shows no significant structures that diverge from that picture and, hence, does not skew the angular dependence of the EWs that follows the HI distributions. An example of a very quite halo is especially M0501, for which I present the H I column densities, EWs, temperature, and velocity dispersion in Fig. 5.13.

In the other cases, where there is no such angular dependence—or even an opposite one as for M0408—I find structures in the HI gas density as well as its velocity dispersion close to the disc, that typically is an after-effect of a merger in the past (cf. Fig. 5.3 for M0858). This merger created HI structures and/or disturbances in the velocity field such that the EWs are no longer elevated in the disc plane. Note,

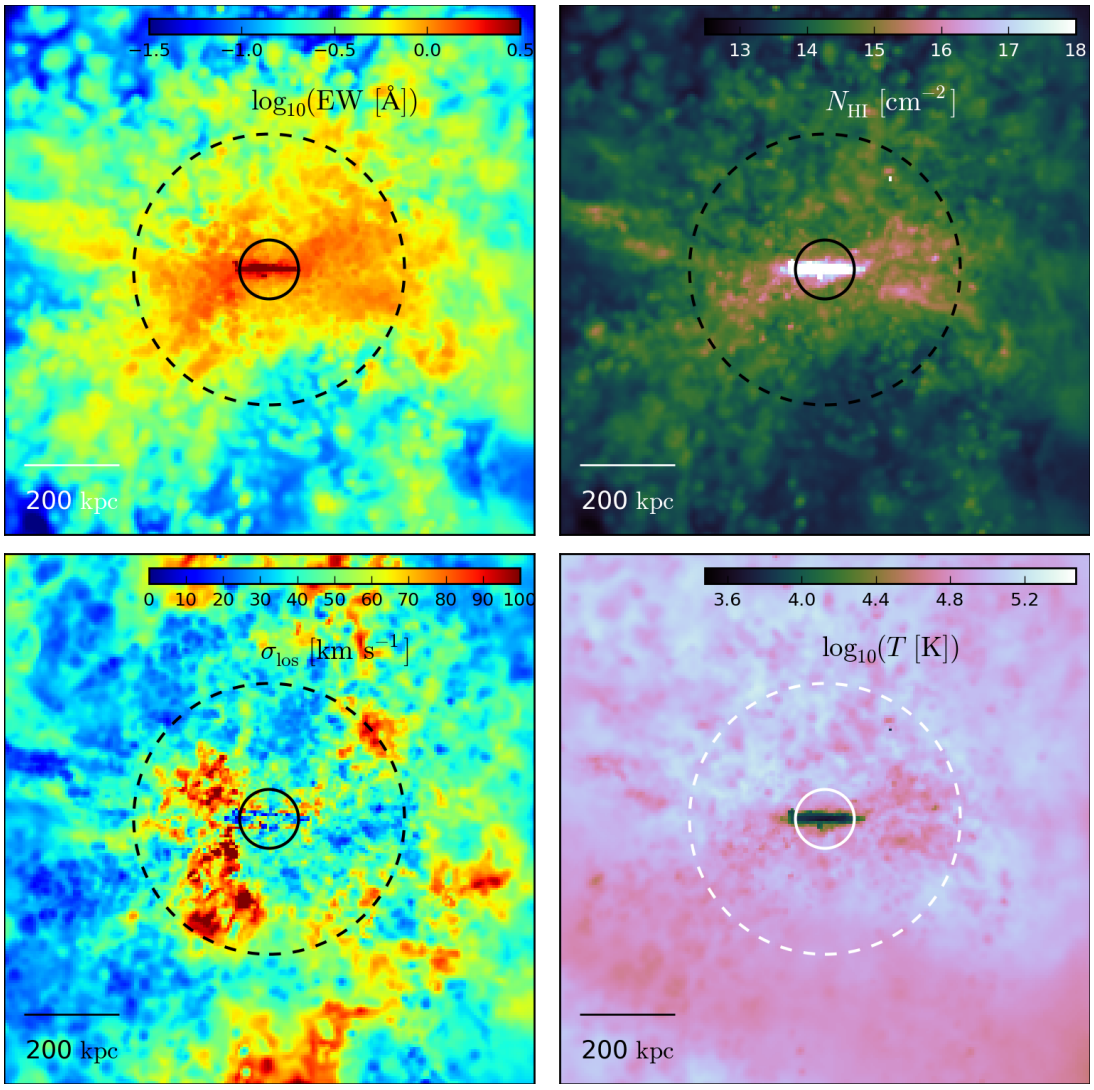

Figure 5.13: A side-on projection of M0501 similar to those of M0858 in Fig. 5.1 and 5.3. The upper right panel shows the column densities of HI; the upper left panel shows the Ly$_\alpha$ EWs; the lower left panel shows the HI gas velocity dispersion; and the lower right panel shows the mean HI mass weighted gas temperature. It is an example of (a large H I disc and) a 'quiet' halo that is not disturbed by a (recent) merger yielding a clear dependence of the EWs with the azimuthal angle.

that this after-effect of mergers can last long as e.g. for M1859 for which the last noteworthy merger happened more than 5 Gyr ago.

5.3 Model and Resolution Dependence

As the results of galaxy formation models of today strongly depend on the methodical and numerical details of the models (see e.g. Scannapieco et al., 2012), I test my results against changes in my model. For that purpose I take the halo M1859 and simulate it once with higher resolution and once with a different, 'weaker' feedback model. For both of these two new simulations I use the exact same analysis pipeline as for the standard resolution and model run and compare the results.

5.3.1 Different Simulations of Halo M1859

Higher Resolution

The higher resolution simulation has higher particle masses (and number) by a factor of 8, making the initial gas masses $\sim 9 \times 10^4 M_\odot$ (see also Tbl. 3.2; I also adjusted the softening lengths, of course). For historical reasons I call it the '8x' resolution, whereas the standard resolution I use in this work is called '4x'.

For the final halo and galaxy of the 8x simulation at redshift zero, I find the radius R_{200} to decrease by 0.85% from 188.8 kpc of the 4x run to 187.2 kpc, while the mass M_{200} decreases by 2.6% from $8.1 \times 10^{11}\,M_\odot$ to $7.9 \times 10^{11}\,M_\odot$. Hence, for these halo properties the simulations differ only marginally. Let us take a look at the central galaxy where the baryon physics matter significantly and numerical difference might change the model outcome more. The stellar mass of the galaxy raised by 8.6% up to $1.72 \times 10^{10}\,M_\odot$, whereas the galaxy's gas mass decreases from $9.09 \times 10^9\,M_\odot$ to $4.37 \times 10^9\,M_\odot$ (-52.2%). The (mass-weighted) average stellar ages are again very similar: 6.96 Gyr for the 8x run and 7.02 Gyr for the 8x, normal run.

These changes are relatively small. Especially as I investigate absorption from the CGM gas, they might still not be considered converged results (the largest difference is in the gas mass). However, I am not so much concerned with convergence, but the dependence of my findings on changes in the model.

In Fig. 5.14 I show maps for H I column densities, Lyman-α EWs, H I velocity dispersions, and temperatures of this higher resolution simulation amongst the 4x resolution and the two simulations with changes in the model itself. The results will be discussed in section 5.3.2.

The models in galaxy formation simulations typically require to adjust parameters in their 'sub-grid' models (cf. the discussion about 'strong' and 'weak' convergence in Schaye et al., 2015), I however have a resolution independent model as energy, momentum, and mass in a feedback event from a given stellar particle is distributed amongst the ten next neighbours. Their mass decreases with higher resolution, but so does the mass of the stellar particle. This situation is not untypical in modern models and they still suffer from resolution dependence (bad 'strong' convergence in the words of Schaye et al., 2015). I, however, always distribute energy, momentum, and mass to both, the cold and the hot phase as well as I delay the thermal energy input to the cold phase until it is sufficient to heat the particle to the hot phase (8×10^4 K). As discussed earlier, the effect of a SN depends much on its surroundings, which can change with resolution. It might be this two-phase feedback which can circumvent the problem of strong vs. weak convergence as my higher resolution simulations are relatively similar to the '4x' simulations[2].

Weaker Feedback

In the weak feedback run (weakFB) I reduced the outflow velocity of SNe from 3000 km/s to just 30 km/s, which reduced the input of momentum into the surrounding gas, but increased the thermal energy input as the total energy output by a single SN ($\sim 10^{51}$ erg) was not changed.

In this simulation the halo grew by about 10% in mass and 3% in R_{200}. The central galaxy, however, has a mass of $6.74 \times 10^{10}\,M_\odot$, more than four times as heavy as the fiducial run with '4x' resolution. This was expected due to the weaker feedback. The galaxy's gas mass decreased by about 40% to $5.48 \times 10^9\,M_\odot$, with also a diminished H I mass of $2.98 \times 10^9\,M_\odot$ as more gas could be converted into stars.

For the Lyman-α absorption in the CGM, the HI gas density in the halo is naturally important. Due to the week feedback I have just very little outflowing gas that can fill the halo (in addition to gas streaming in from the outside) and, hence, I find much lower HI column densities and EWs in the halo. This can be seen in Fig. 5.14, which also shows the familiar maps of EWs, column densities, velocity dispersions, and temperature for this simulation.

These simulations were not done with the purpose of matching observational results but to compare my findings in the Lyman-α absorption lines to a different model, in order to show that they are not just a feature of my particular model.

[2] As the domain decomposition in GADGET prevented me from running more than four, I had just little data for a proper comparison. Additionally, three out of the four high resolution simulations are smaller halos than those presented in this thesis.

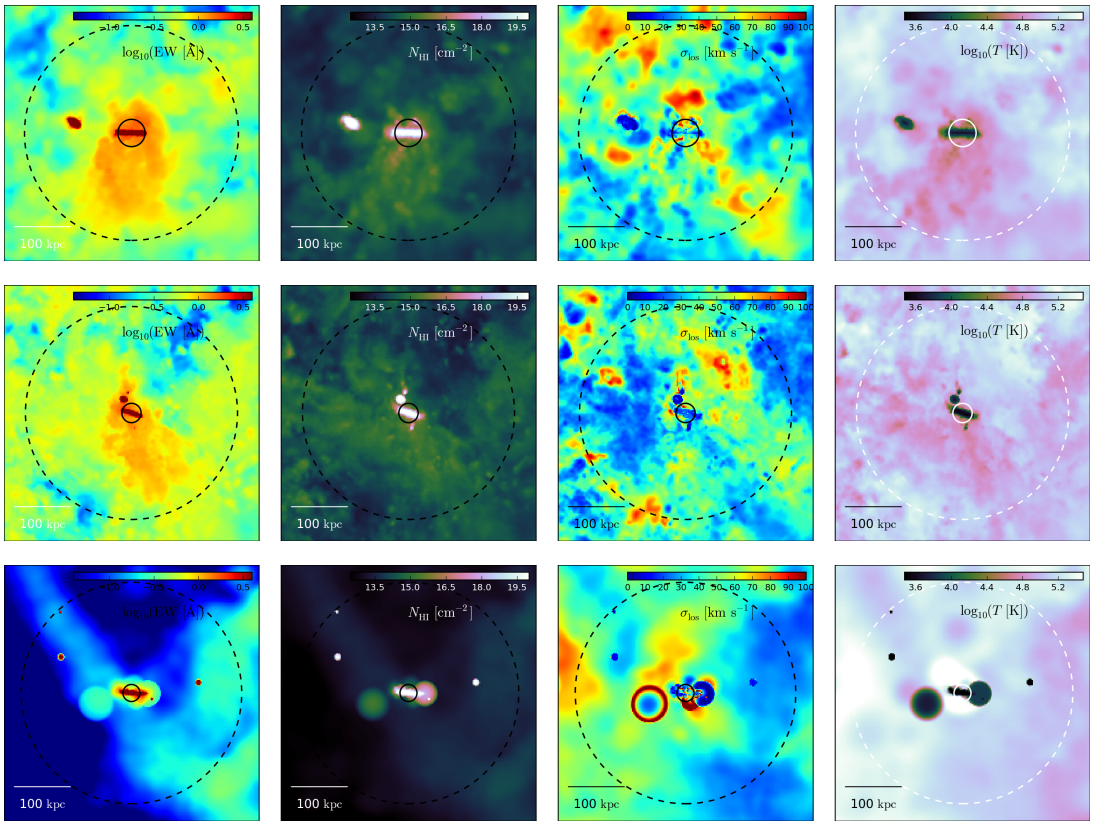

Figure 5.14: The maps for M1859 with the standard model and resolution (first row), with increased resolution (initial particle masses are larger by a factor of 8; second), and with the standard resolution but a weaker feedback (bottom row).

5.3.2 Absorption in Different Simulations Models

Comparing the Maps

The weak feedback run differs quite significantly in terms of stellar masses, gas masses, halo density, or halo structure. However, the normal (4x) and high (8x) resolution simulations are remarkably similar (cf. also Fig. 5.14; what is typically found in galaxy simulation models is that the model parameters have to be adjusted for different resolutions), but here I my intention is to compare the behaviour of the Lyman-α lines with respect to column density, temperature, and velocity dispersion. For that purpose it is actually valuable to have a variety of different conditions to compare with.

The 4x and 8x (upper and middle row in Fig. 5.14) are not only similar in their integrated properties but also their maps compare well. The H I column densities in the CGM are typically of the order of $10^{14} - 10^{15}\,\mathrm{cm}^{-2}$ and the temperatures range from $10^{4.5}\,\mathrm{K}$ to $10^{5.5}\,\mathrm{K}$. Despite that the smaller galaxy is closer to the central galaxy, tilting its disc slightly, both the normal and the high resolution run have a common feature in the EW map: south of the galaxy they are elevated to about 1 out to almost R_{200}. In this case, the higher EWs are indeed mainly caused by high column densities. However, the velocity dispersions are still shaping the EW map. For instance, in the western part of the maps of the 8x resolution simulation (middle panels of Fig. 5.14) the column densities are about as large as in the southern feature of high EWs, while the velocity dispersions are small, keeping to EW at almost 0.5 dex lower values.

In the bottom row of Fig. 5.14 a different pictures emerges for the weak feedback run. The column densities are about an order of magnitude smaller than in the other two simulations of the same halo and the temperatures have a slight tendency towards higher values. The satellites are also different ones and more than in my fiducial run. These smaller column densities result in a much worse (spatial) resolution of the CGM because in SPH it is tied to the mass. This phenomenon is particularly striking next to the central galaxy where there is a single cold gas particle dominating column densities west of the gas disc. It is a particle that was expelled from the disc by stellar feedback recently and did not yet match the properties of the surrounding gas. As this particles also has a very different velocity (because it was ejected) than the surroundings, there is a ring-like structure in the velocity dispersion, where the kernel weight is small enough so that the column densities are comparable to the background.

Equivalent Widths Correlations

In Fig. 5.15 I plot, similar to Fig. 5.2 and 5.4, the correlations of the EWs with column density, velocity dispersion, and temperature for all the discussed runs of halo M1859 that correspond to the maps in Fig. 5.14.

Again, the 4x and 8x simulation are very similar. All three correlations with the EWs are very similar by all means, which is not surprising considering that they are similar in all other points. For the weak feedback run, however, the sight lines have much smaller column densities due to the low densities in the CGM. This puts the bulk part of the l.o.s.s into the linear regime of the curve of growth. Here, temperature and velocity dispersion are naturally not important for determining the EWs. A closer look, however, shows that there are a few sight lines in the logarithmic regime as well. There is one more prominent arm at around $10^{-0.5}$ Å, starting slightly below at $\sim 10^{14}\,\mathrm{cm}^{-2}$ and extending to slightly higher values at $10^{17} - 10^{19}\,\mathrm{cm}^{-2}$, where the square-root regime is entered. The second arm is much weaker and runs parallel to the first one with $\sim$0.5 dex higher EWs.

At lower column densities ($\sim 10^{14} - 10^{15}\,\mathrm{cm}^{-2}$), the lower arm can be attributed to the single cold gas particle seen to the east of the gas disc in the maps of Fig. 5.14. The other part of the arm is caused by other, smaller regions of dense, cold gas with low velocity dispersions. In the outer parts of these regions, the velocity dispersions rise again as the kernel weights of the dense, cold gas decreases and its weighted column density is comparable to the surrounding CGM gas. These transition zones cause the second, less confined arm in the logarithmic regime of the weak feedback simulation.

Conclusion

I have compared a high resolution simulation and one with weaker feedback to the simulation of one of the halos, M1859. The higher resolution run was in all aspects very much like the 4x run, including the EW map itself. Hence, it supported all of my findings. The weak feedback model resulted in a very sparse CGM gas and thus poor resolution there. Hence, most of the sight lines have column densities in the logarithmic regime, still a few indicated the same relations of the EWs with velocity dispersions, although it was often caused by single particles.

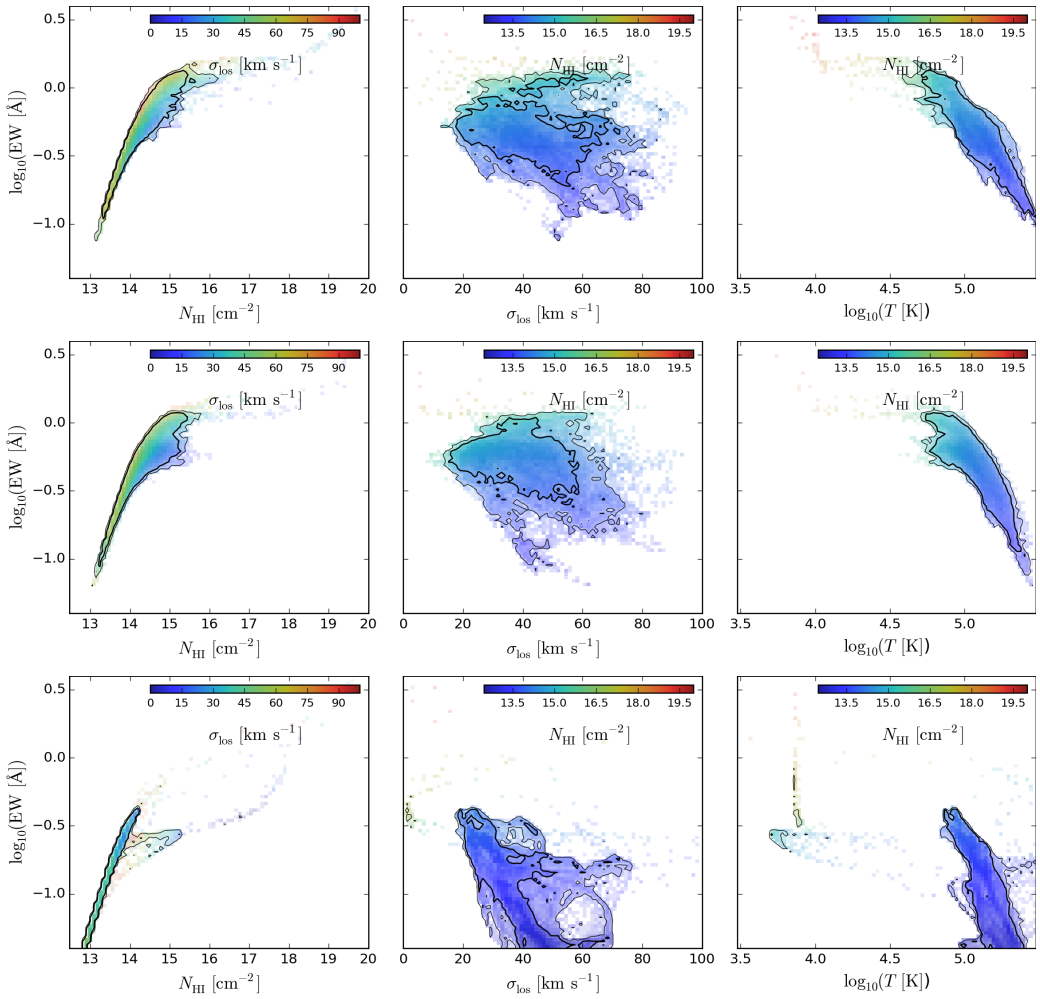

Figure 5.15: The maps for M1859 with my standard model and resolution (upper row), with increased resolution (initial particle masses are larger by a factor of 8; second row), and with the standard resolution but a weaker feedback (bottom row).

Chapter 6

Results for Metal Ions and Metal Line Absorption

As outlined earlier, metal line observations in the CGM are crucial to understand its structure. They can provide valuable information on the ionisation state, the metal distribution itself of course, the metallicities, and might also resolve the degeneracies in the Hydrogen lines, because the metal column densities are naturally much smaller and, hence, their lines are typically not as saturated.

6.1 Phase Space Distributions

Complementing the phase diagram mentioned in the beginning (Fig. 2.4) I plot the distribution of chosen ions in the phase diagram of the zoom volume. This is all gas within $2 \times R_{200}$ and thus I am missing the very low densities in voids that do occur in the phase diagram of the EAGLE simulation (Fig. 2.4), which is a full cosmological box. In Fig. 6.1, I show two phase diagrams, the upper one is of the already discussed halo M0858, which is a very typical one in terms of the phase diagram . I have restricted myself to H I (the most common aborbing species), Mg II, C IV, and O VI (the next most often studied species) as well as Si III, which bridges the gap between the lower ions (H I and Mg II) and the higher ones (C IV and O VI) and also is detectable relatively easily.

As a main ionisation process is photo-ionisation, higher ions progressively trace less dense gas and thus also hotter gas. Additionally, the ionisation potentials progressively increase for the higher ions, moving the range of temperatures up where collisional ionisation takes place. For O VI this is around $10^{5.5}$ K, for C IV this is around 10^5 K and for Si III it is a few 10^4 K. H I and Mg II occupy almost the same

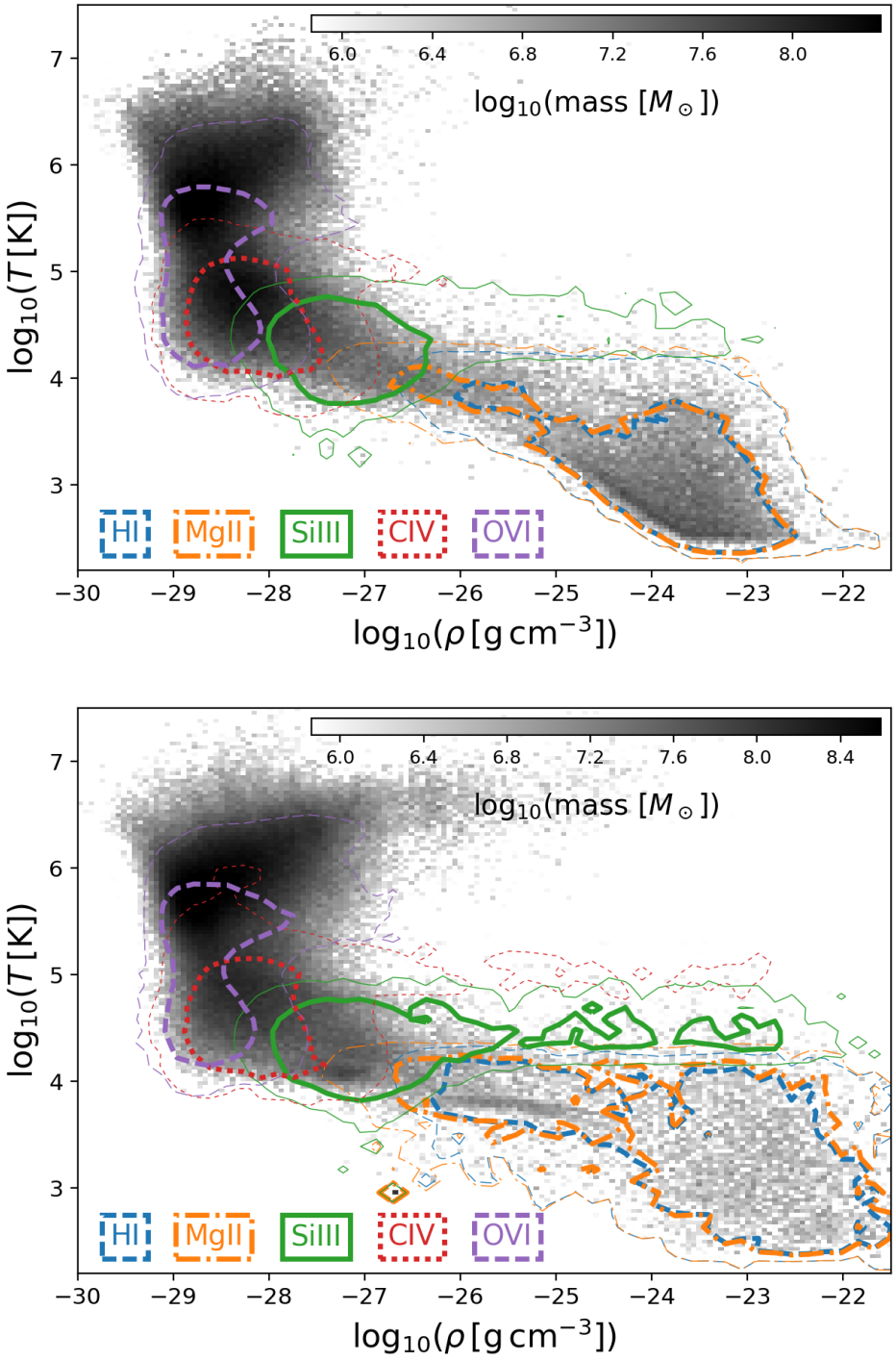

Figure 6.1: The phase diagram for all gas within $2\,R_{200}$ for M0858 (top panel, typical example) and M0664 (lower panel) together with the temperature-density distribution of H I, Mg II, Si III, C IV, and O VI. The thick lines enclose 80% of the ion mass (similar to Fig. 2.4) and the thin lines enclose 99%. The Si III occurs at much higher densities in M0644 than typically seen (see text for discussion).

region in the phase space, making them good tracer for each other, whereas the higher ions almost do not overlap with these two. I will discuss this in section 6.5 in more detail.

The phase diagram of M0664 (lower panel of Fig. 6.1) is special in the way that it has a little C IV at higher densities ($\rho \gtrsim 10^{-27}\,\mathrm{cm}^{-2}$) where I typically find no C IV and it also has significant amounts of Si III at high densities ($\rho \gtrsim 10^{-26}\,\mathrm{cm}^{-2}$). Finally, the high density gas, and thus also H I and Mg II, is heated to unusual warm temperatures of up to $\sim 10^4\,\mathrm{K}$. This can be explained due to the fact that M0644 is currently undergoing a violent major merger (cf. also Fig. 6.2) that shock-heats the ISM (and a slightly elevated SFR of currently $14\,M_\odot\,\mathrm{yr}^{-1}$). There are also large amounts of tidally stripped gas, reaching out $\sim 300\,\mathrm{kpc}$ (beyond $R_{200} \simeq 264\,\mathrm{kpc}$). The bulk part of the dense, warm Si III, however, is located in the ISM. This gas is still dense, but heated above the typical low ISM temperatures.

6.2 Ion Spatial Distributions and Flows

6.2.1 Ion Flow Maps

Fig. 6.2 shows maps of the H I, Mg II, Si II, Si III, C IV, and O VI distributions as well as an overall gas column density map, a (density-weighted) temperature map, and the stellar distribution for comparison. These maps have the (ion) mass-weighted velocities plotted over as small arrows which lengths are proportional to the mean velocity.

The low ions (Mg II and Si II) and H I are similarly distributed, although the cold inflowing stream to the west has low metallicities (it was not yet enriched by stellar feedback from the big central galaxies) and thus has in relative terms less Mg II and Si II when compared to H I. In the cold and warm regions, these ions also have a similar velocity structure as the overall gas and by this they primarily trace the inflowing gas in the CGM. The two cooler ($10^4 - 10^5\,\mathrm{K}$, one is the tidally stripped gas, the other is a rather pristine inflow), dense streams to the north west move towards the central galaxy and their velocity fields are traced by the low ions. There is also inflow from the south-east in the low ions (as well as Si III and C IV). About 50 kpc north west of the central galaxy, the overall velocity structure is quite diffuse, but H I as well as Mg II and Si II coherently flow to the center. In fact, the inflowing velocities of the H I / Mg II / Si II mass weighted are significantly larger than the ones weighted with all gas mass (cf. subsection 6.2.4).

The inflows can still be seen in the flow of the intermediate ion Si III (bottom left panel of Fig. 6.2). They decrease a lot for C IV, although the inflow from the south-

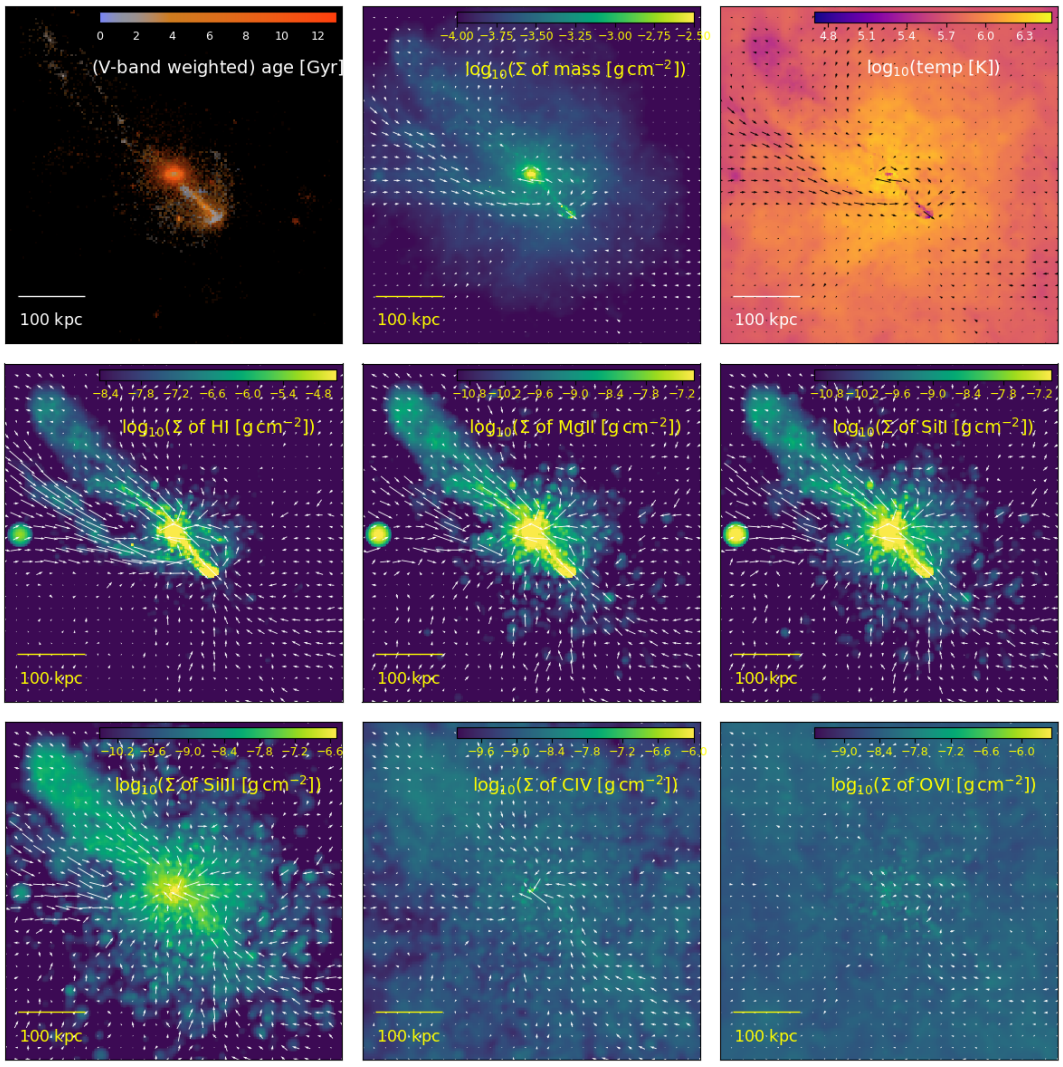

Figure 6.2: From top left to bottom right: stars, total gas column density, (density-weighted) temperate of all gas, and then the column densities of the ions H I, Mg II, Si II, Si III, C IV, and O VI of halo M0664. The maps have a side length of 500 kpc and the arrows are proportional to the (ion-)mass-weighted velocities. For all the ions, the scales for the column densities span four orders of magnitude each.

west is still present. O VI, finally, is almost static when compared to the lower ions, tracing the hot CGM atmosphere in the halo. However, in many cases, O VI traces outflows from the galaxy, which are simply not present (to significant amounts) in the case of M0664.

In Fig. 6.3, I present the same maps for the much more typical (than M0664) and familiar halo M0858, that is not currently or has recently been in a merger. It, however, has the arc-like feature and the satellite to the north-east. Again, inflowing gas is well traced by the lower ions (H I, Mg II and Si II) and still partly by Si III. The properties if C IV such as spatial distribution and the tracing of in- or outflows are inbetween those of the low ions and O VI. O VI, which finally traces outflowing gas, that was bot seen in M0664. It, however, is typical to see outflows in O VI (for more details see subsection 6.2.4). This is mainly towards the south-east, but also to the north and north-west. This outflowing gas of the higher ions is still close to a uniform distribution with only very slightly elevated densities in the prominent flows.

Different ions indeed often trace physically distinct phases of the CGM as was already indicated by the phase diagrams in Fig. 6.1. Generally, low ions (such as the discussed H I, Mg II and Si II) are more concentrated towards the halo center and also trace satellites and streams. Hence, they are not as uniformly distributed as higher ions are. The higher ions such as C IV and O VI are much more uniformly distributed over the halo and do not trace denser structures. They, however, do sometimes trace outflows; preferentially, these are the highest ions, O VI and above.

6.2.2 Escaping Gas

It is predominantly the hot gas and the higher ions that trace outflowing gas. This is also represented by the fact that the fractions of gas with velocities larger than the escape velocity is largest for O VI amongst the studied ions. To show that, I calculated the escape velocities at the position of each SPH particle assuming spherical symmetry, i.e. I calculated $v_{\rm esc} = \sqrt{2 M_{\rm enc} G / r}$ with $M_{\rm enc}$ being all mass closer to the halo's centre than the SPH particle. I then defined all particles as 'escaping' that have a (outward) radial velocity larger than $v_{\rm esc}$. The escape velocities depend on the radius, but are typically relatively constant in the CGM and of the order of 200 km/s.

Typically, I find of order 1% of the CGM mass 'escaping'. Here the CGM was simply defined as all gas with radii $0.2\,R_{200} - 1.0\,R_{200}$. Using these definitions for the different ions, the escaping fractions of the low ions such as H I and Mg II are normally $\lesssim 10^{-4}$ and never come close to the global escaping fractions. In absolute

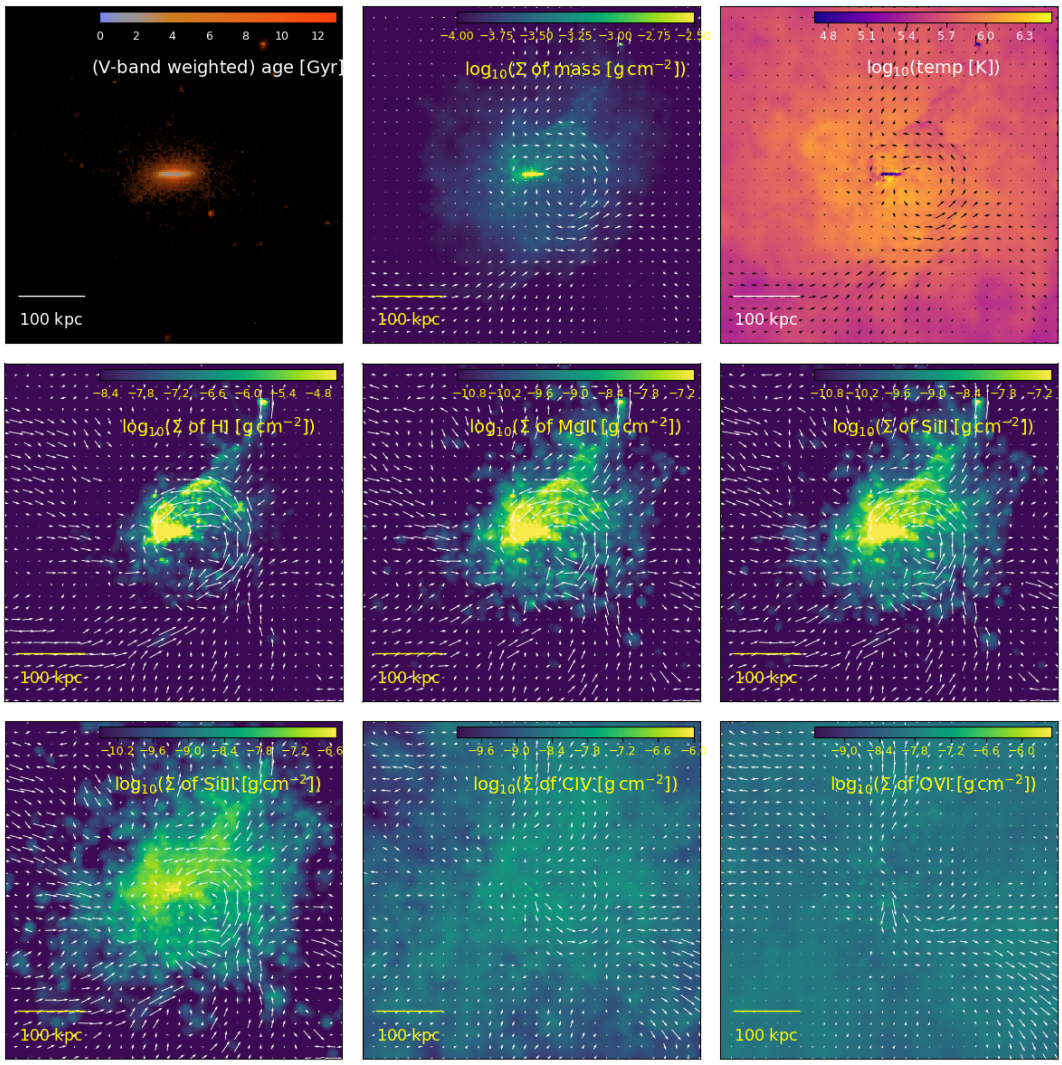

Figure 6.3: From top left to bottom right: stars, total gas column density, (density-weighted) temperate of all gas, and then the column densities of the ions H I, Mg II, Si II, Si III, C IV, and O VI of halo M0858, analogue to Fig. 6.2. The maps have a side length of 500 kpc and the arrows are proportional to the (ion-)mass-weighted velocities. For all the ions, the scales for the column densities span four orders of magnitude each.

values this translates to $< 10^3\,M_\odot$. In other words, there is rarely a noteworthy amount of low ions that could escape the halo. Si III has only seldom significantly higher fractions of 'escaping gas'. C IV has higher escaping fractions and O VI finally has typically larger escaping fractions that the total gas, sometimes reaching 10% (typically $\sim 10^5\,M_\odot$ in pure O VI) and more.

As already mentioned above, it sometimes is even hotter gas than that traced by O VI that is mainly outflowing. And also the escaping fractions of the hot gas—here defined by $T > 10^6\,\mathrm{K}$—are often even higher than those for O VI. In my ensemble that happens for six out of the twelve halos, and here I just counted those that have at least 1% of O VI and hot gas escaping.

The picture drawn so far shows that hot gas traces outflowing gas quite well, which is not very surprising as the outflows are driven by SNe that heat the gas (cooling times are of the order of gigayears as the dynamical time are, too). Also higher ions such as O VI (and higher ones) and sometimes also already C IV trace outflows. Note, however, that I find $\sim 25\% - 45\%$ of the hot ($T > 10^6\,\mathrm{K}$) gas inflowing, i.e. with radial velocities smaller than zero. Also $\sim 25\% - 55\%$ of the O VI is inflowing in that sense! Warm-hot gas ($T > 10^5 - 10^6\,\mathrm{K}$) does trace outflows better than other gas, and similarly do metals trace outflows ($\sim 30\% - 45\%$ infalling and also slightly larger amounts than for the hot gas are escaping) better than other gas. However, one shall not mistake this as hot gas / higher (metal) ions always trace outflows.

6.2.3 Radial Velocity Profiles

The numbers so far were mass averaged over the entire CGM, which typically weighs smaller radii more as the gas gets denser towards the centre. In Fig. 6.4, I present the radial profiles of in- and outflowing fractions, equalising the weighting problem. For this purpose I defined gas as outflowing if it has a radial velocity of at least 50 km/s away from the centre (just a working definition; for comparison, though: the FWHM of a Lyman-α line due to thermal broadening by $T = 5 \times 10^4\,\mathrm{K}$ would be 48 km/s, for C IV lines at $T = 5 \times 10^5\,\mathrm{K}$ it is 44 km/s;typical escape velocities in the simulations are of order 200 km/s) and analogously I define inflowing gas as such that has radial velocities smaller than -50 km/s. I call the remaining gas that has small radial velocities 'static gas', although it could have high tangential velocities.

Typically around 60% of the H I and Si III gas is inflowing in that sense at radii between ~ 50 kpc and ~ 250 kpc and usually less than 10% are inflowing. The scatter around these values, however, is quite large. For the highly ionised O VI, the scatter is not as large, but there is around 20% inflowing and the 'static' component rises

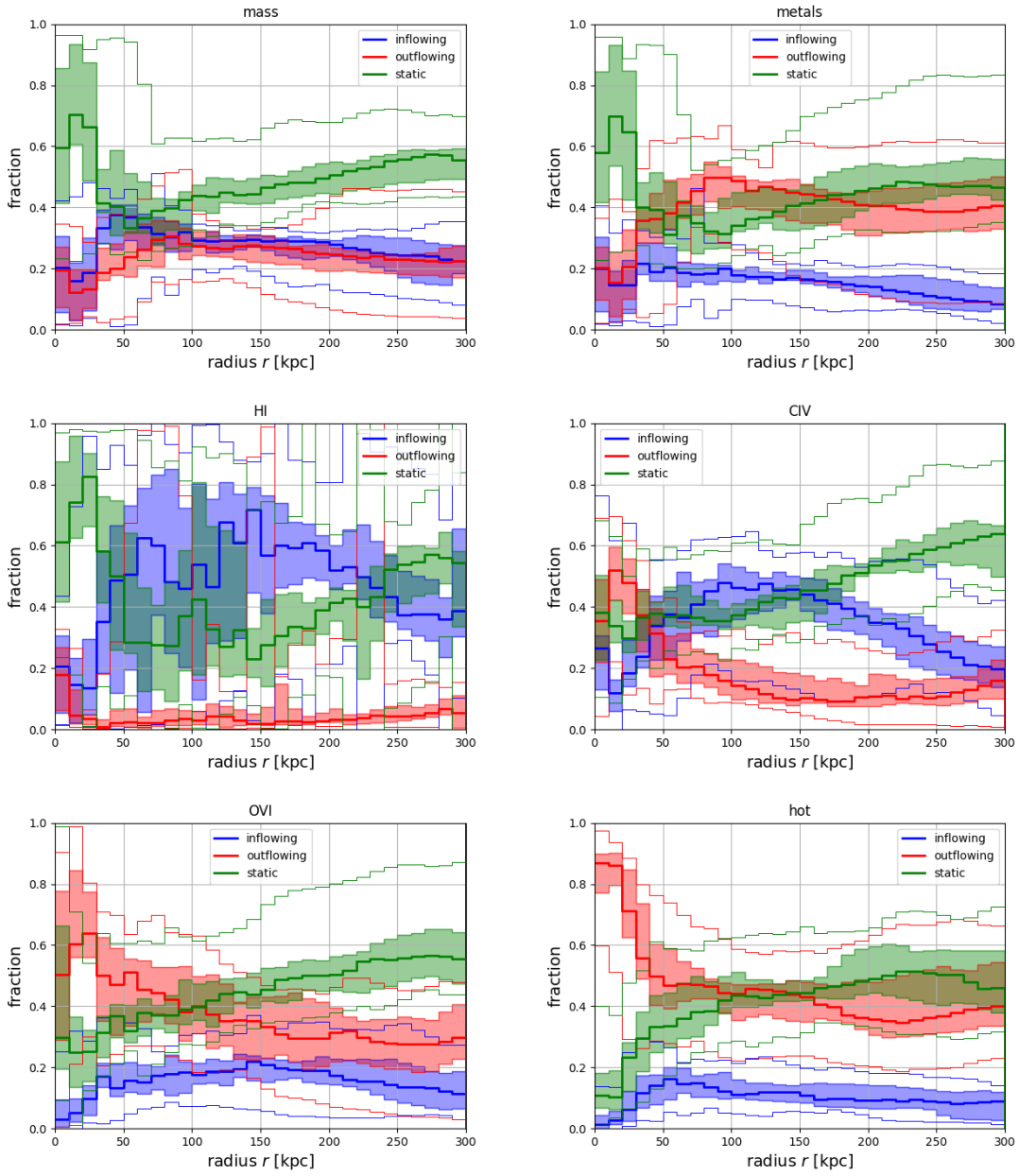

Figure 6.4: The mass fractions of in- and outflowing gas of all 12 simulations. Inflowing gas is defined as gas having a radial velocity of less than ($-50\,\mathrm{km/s}$; blue); outflowing gas (red) is defined analogously; the 'static' gas (green) is finally all remaining gas, i.e. that gas with radial velocities of less than $50\,\mathrm{km/s}$ in either direction. The thick lines are the median values over all halos, the transparent bands indicate the quartiles, and the thin lines are the minimum and maximum fractions over the simulations. Here, hot has is defined as gas with temperatures $T > 10^6\,\mathrm{K}$.

from $\sim 20\%$ to more than 50%. Still, the outflowing gas dominates at radii larger than $\sim 100 - 150\,\mathrm{kpc}$. Although the hot gas ($T > 10^6\,\mathrm{K}$) can have even larger outflowing fractions than the O VI gas, the static component is comparably large. The intermediate ion C IV transitions between the two extremes. In contrast to the lower ions, it typically has a non-negligible outflowing component, and the inflowing one is slightly diminished and almost never exceeds $50\% - 60\%$.

In order not to impose a limit for in- and outflowing rate, I plot the net-flow rates through the shell of a given radius of various gas phases and ions in Fig. 6.5. The results are similar to what Fig. 6.4 shows: the metals are almost never inflowing like the hot ($T > 10^6\,\mathrm{K}$) gas, which is always outflowing. Also O VI is almost always outflowing, now more clearly seen than in Fig. **??**. C IV is sometimes inflowing and sometimes outflowing. Finally, the lower ions and H I are mostly inflowing; that's on very small rates, though, too small for the scales used here (for the sake of clarity). The consistent inflowing rates are only large enough at small radii to be seen. The low ions and H I are concentrated in substructures that move through the CGM, creating the large peaks.

6.2.4 Metal Budget and Recycling

Fig. 6.6 shows the mass, metal, H I, and ion profiles of all simulated halos, normalised to R_{200}. Although the metal profiles fall steeper than those of all gas, I often find more than 50% of the metals within the halo to be beyond $20\%\,R_{200}$. In the cases, where it is less than half of the metals in the halos, the halos are lighter and metals that were ejected could travel beyond R_{200} as the potential is not so deep. In fact, typically $40\% - 50\%$ of the metals between R_{200} and $2\,R_{200}$ once have been in the central gas disc, whereas this is true for only $\sim 25\% - 35\%$ (sometimes even less) of the total gas mass in this region. Also for the CGM, again defined as all gas with radii in the range $0.2\,R_{200} - R_{200}$, the recycled fraction (those once been in the central gas disc) of metals is typically twice as large as those of the total gas mass.

H I and the low ions Mg II and Si II exhibit peaks at locations of substructure in the CGM as they trace the cold, dense gas. In higher ionisation states (Si III, C IV, and O VI) the substrucutre does not persist. Furthermore, the profiles get flatter from intermediate (e.g. Si II) to higher ionisation states (e.g. O VI). O VI is almost flat. Its densities decrease by only a factor of typically ~ 3 from $0.5\,R_{200}$ to $2\,R_{200}$, whereas Si III densities can decrease by up to almost eight orders of magnitude over that range. That will also imply that the line spectra of O VI will arise from large regions with absorbing path lengths of several hundred kilo-parsec (see section 6.5 and Fig. 6.13).

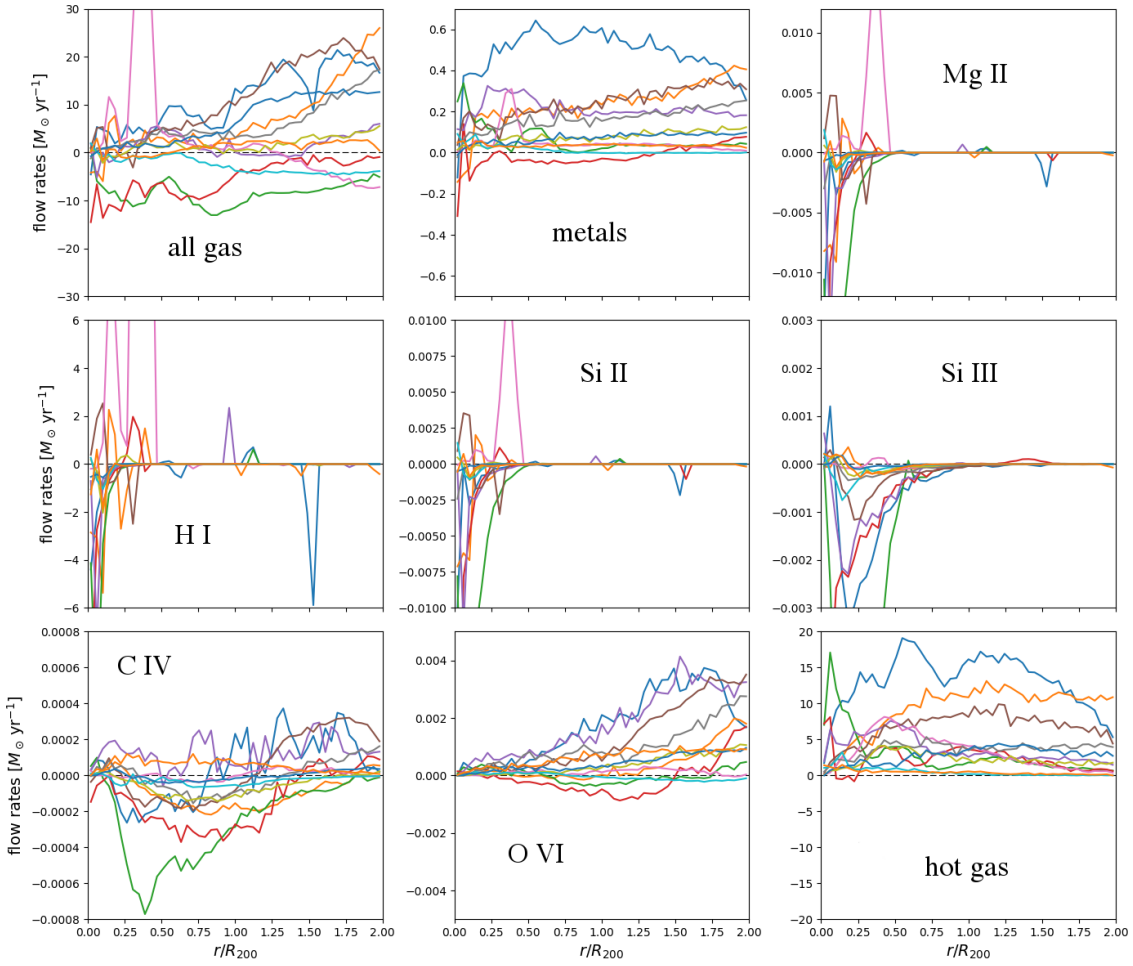

Figure 6.5: The gas flow rates. In reading direction: all the gas, the metals, Mg II, H I, Si II, Si III, C IV, O VI, and hot gas ($T > 10^6$ K). The overall flow rates are more often than not pointed outwards, the metals are always never inflowing like also O VI and the hot gas. The Mg II, Si II, and H I primarily live in cold dense structure, that is spatially confined at small locations. They show a very spiky profiles, however, are mostly inflowing with small rates (too small to be seen here).

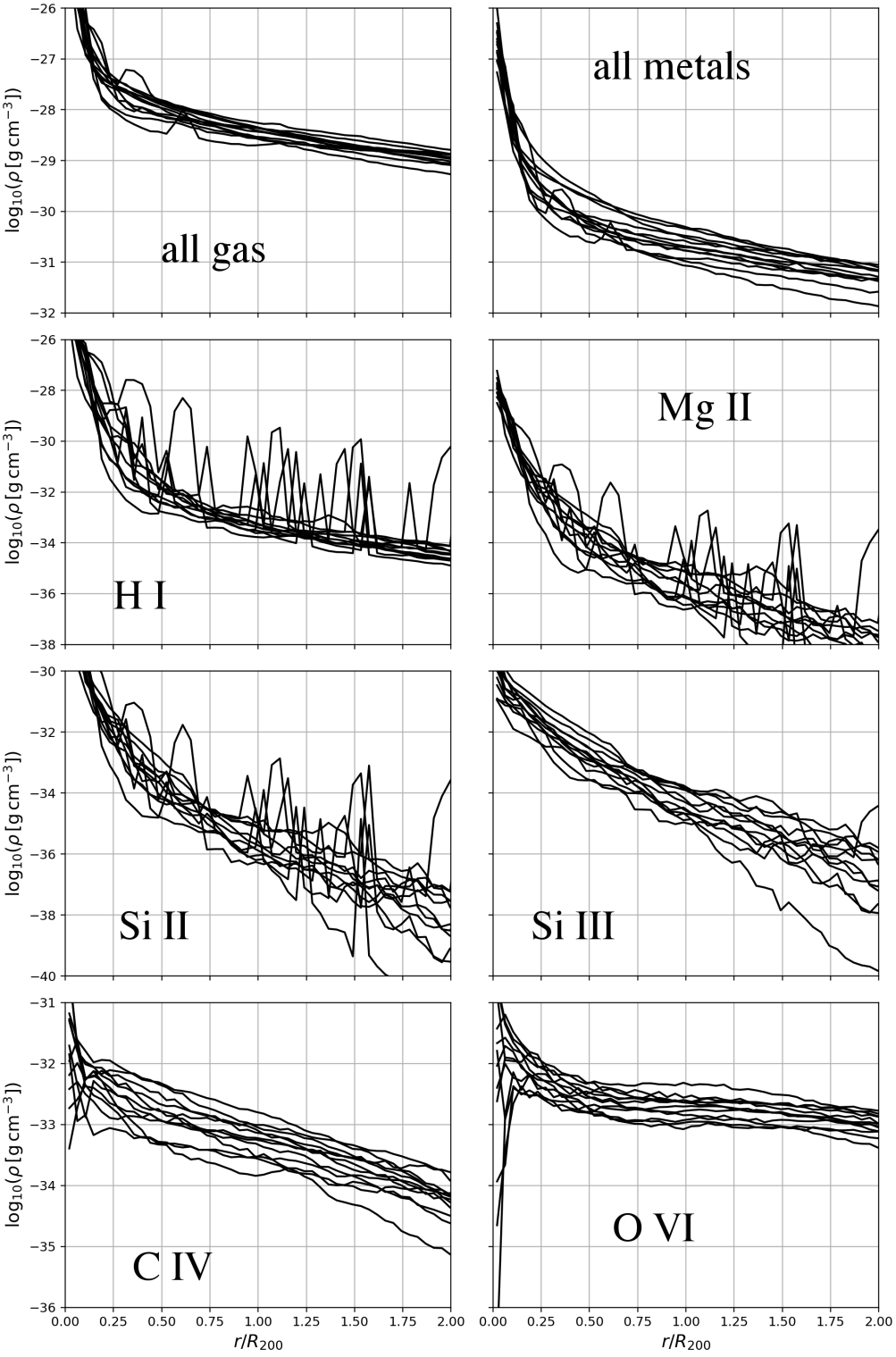

Figure 6.6: The 3D mass, metal, H I, and ion density profiles of the 12 simulated halos.

6.3 Mg II Lines

Let us now have a look at the EWs profiles that arise from these. In Fig. 6.7 and 6.8 I present the Mg II λ2796Å EW profiles for the 12 simulated halos analogous to Fig. 5.9 and 5.10 in subsection 5.2.4 where I did the same for H I. Here, however, I compare to Werk et al. (2012) who presented data for redshifts between 0.14 and 0.36. I restricted these further from 44 to 34 galaxies with Mg II detections at redshifts $0.14 < z < 0.27$ for better comparison to the simulations, from which I used snapshots at $z = 0.22$, the median redshift of the residual observational data.

For all halos the profiles are steeper and more concentrated than those for Ly_α, becoming entirely non-detectable between $\sim 100\,\mathrm{kpc} - 200\,\mathrm{kpc}$ at present day instruments as they fall steeply below 0.01 Å. The highest EWs can easily be explained by the most massive halos, especially M0408 (upper left panel in Fig. 6.7) and M0616 (middle left panel in Fig. 6.7). The smallest EWs, i.e. those below 0.1 Å, which are mostly upper limits lie within the middle 80% of the EWs I find in the simulations. For those further out, these are naturally the massive halos and galaxies as the EWs correlate with the halo mass; the small EWs at small radii can be explained with the lighter halos. Only the two upper limits at $\sim 20\,\mathrm{kpc}$ and $\sim 30\,\mathrm{kpc}$ are barely below the 10%ile in even the lightest halo (M2283, bottom right panel in Fig. 6.8).

However, my simulationed galaxies have slightly higher masses than those of the observations. My simulated profiles are drawn from halos with central galaxies of stellar mass of $10^{9.9} - 10^{11.2}\,M_\odot$ with a median mass of $4.2 \cdot 10^{10}\,M_\odot$. The observed EWs are associated with galaxies of stellar masses between $10^{9.7}\,M_\odot$ and $10^{11.4}\,M_\odot$, a little broader than my range and thus reaching to lower masses. Also the median stellar mass, $3.7 \cdot 10^{10}\,M_\odot$ is slightly below mine.

Despite the very slight mismatch of the ensembles, the overall profile from all the 12 simulations combined agrees with the data from Werk et al. (2012). The result is presented in Fig. 6.9. Most observations are within the 10%ile and the 90%ile with also the median roughly following the simulated one. However, especially for the smaller radii ($\lesssim 70\,\mathrm{kpc}$) the simulations might over-predict the observed EWs slightly similar to what the Ly_α comparison had shown. Again, as both the observations and especially my simulations (only 12 galaxies) are limited in size, these results shall be taken with caution. The discrepancy, though, might be as large as $\sim 0.2\,\mathrm{dex}$ in terms of the median. And again, as for the Ly_α lines, that could be explained by M_HI-to-M_stars ratios that are also about 0.2 dex too small on average (though still well within the scatter) (cf. Fig. 3.4).

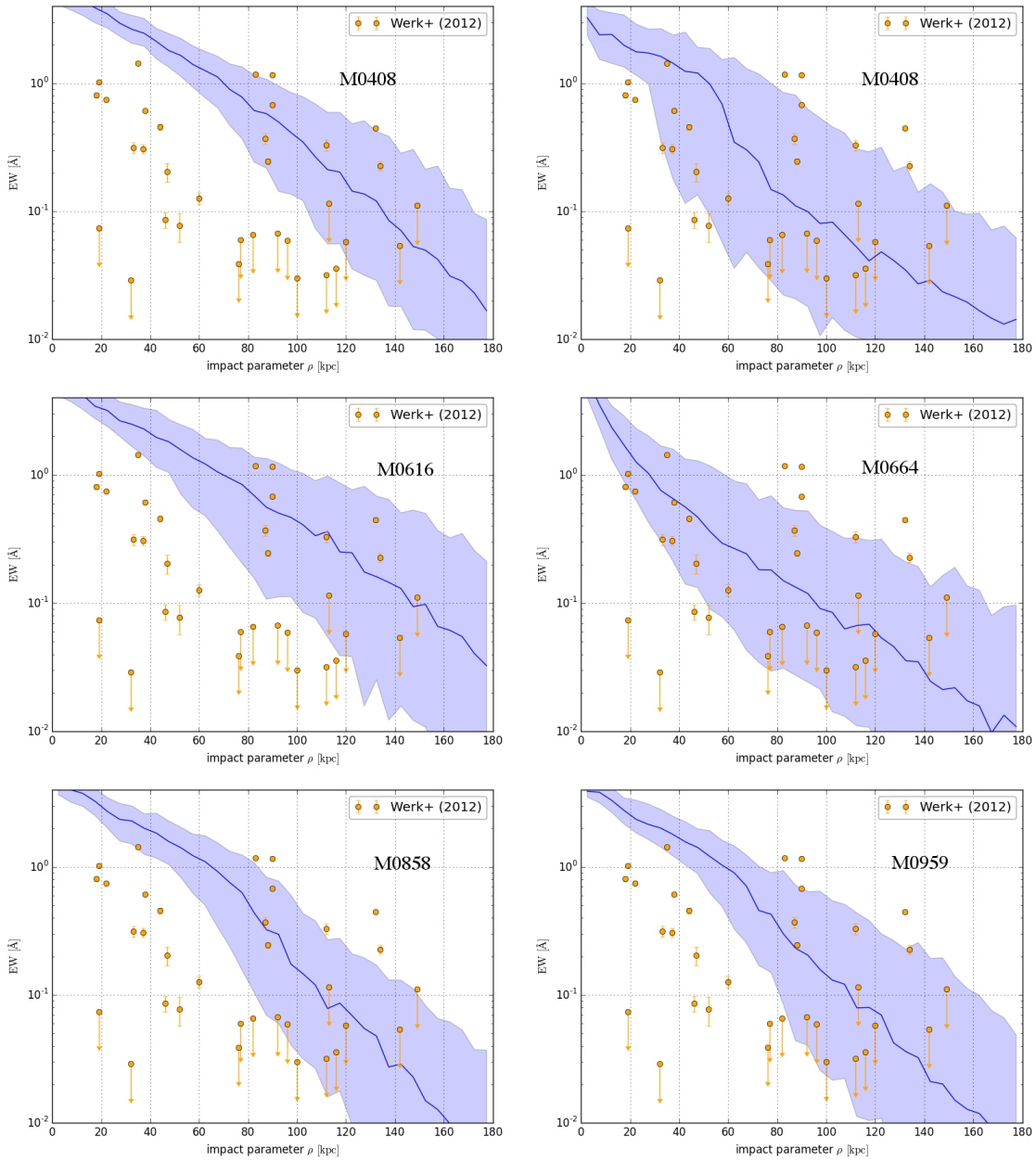

Figure 6.7: Mg II λ2796Å EW profiles for halos M0408, M0501, M0616, M0664, M0858, and M0959 (from top left to bottom right) at redshift $z = 0.22$ as generated from 20 random orientations for each halo. The blue line is the median EW for each radial bin of 5 kpc width and the light-blue band indicated the 10%ile and 90%ile in these bins. For comparison the observations as presented in Werk et al. (2012) (restricted to $0.14 < z < 0.27$, median $z = 0.22$) are plotted in orange.

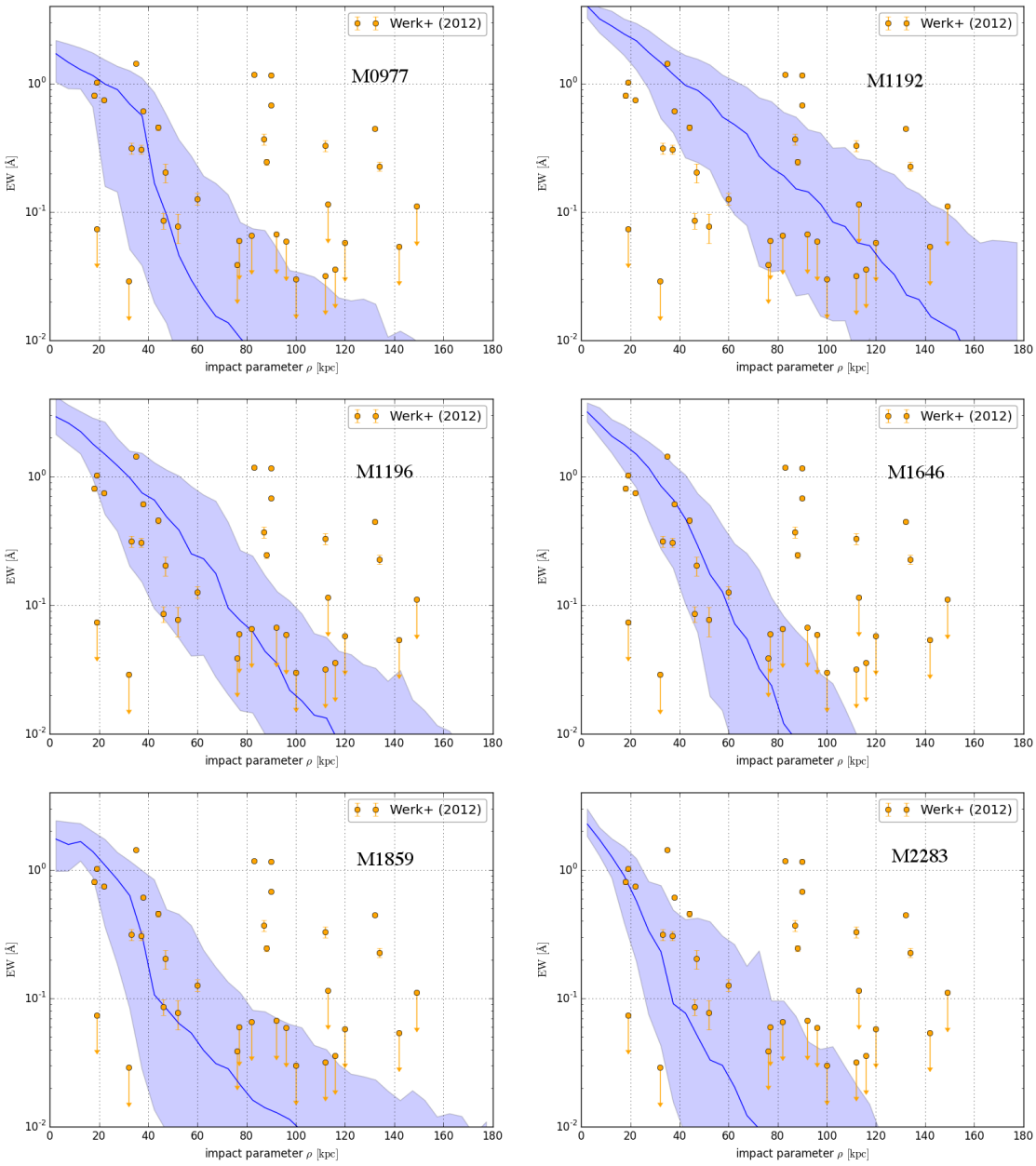

Figure 6.8: Mg IIλ2796Å EW profiles for halos M0977, M01192, M1196, M1646, M1859, and M2283 (from top left to bottom right) at redshift $z = 0.22$ as generated from many random orientations for each halo analogue to Fig. 6.7. The blue line is the median EW for each radial bin of 5 kpc width and the light-blue band indicated the 10%ile and 90%ile in these bins. For comparison the observations as presented in Werk et al. (2012) (restricted to $0.14 < z < 0.27$, median $z = 0.22$) are plotted in orange.

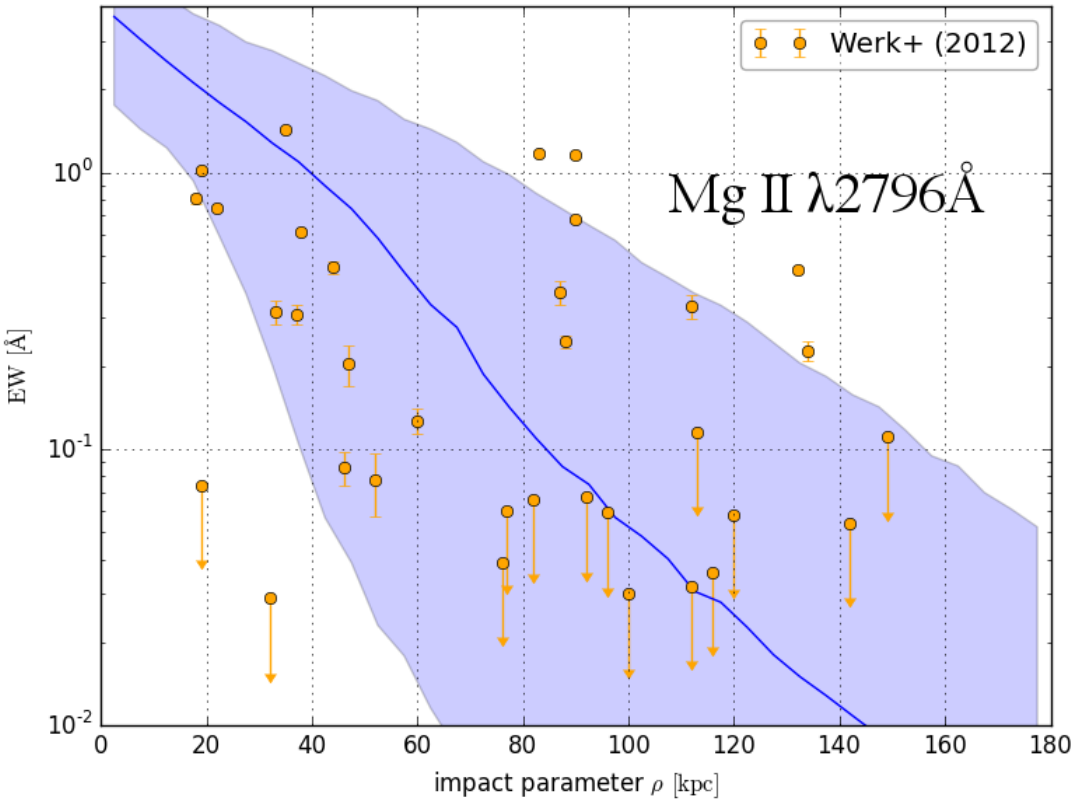

Figure 6.9: The same plots as in Fig. 6.7 and 6.8 but now for all 12 simulations combined. For comparison the observations from Werk et al. (2012) (restricted to $0.14 < z < 0.27$) are again plotted in orange.

6.4 O VI Lines

The O VI lines are typically under-predicted by roughly 0.7 dex (see e.g. Ford et al., 2016, Gutcke et al., 2017, Hummels et al., 2013, Suresh et al., 2015) in simulations. In Fig. 6.10 and 6.11 the simulated EWs profiles for O VI λ1031Å are presented similar to what was done for Ly$_\alpha$ and Mg II λ2796Å above. The results are again compared to the data from Werk et al. (2012) (restricted to $0.14 < z < 0.27$).

One can right away see that my simulations do not under-predict the EWs and the more massive galaxies actually tend to over-predict them. Their median EWs are higher than for all measured O VI lines. However, there are always at least a few observed lines that fall between the 10%ile and the 90%ile of the simulations. The less massive halos (Fig. 6.11) all lie in the range of the detected O VI lines. Still, they all fail to explain the six non-detections. This might well be due to the relatively low spatial resolution the simulations have in the CGM. Typical smoothing lengths for particles with higher amounts of O VI are $15 - 20$ kpc (actually the O VI mass weighted median) and can even reach $\sim$100 kpc.

Fig. 6.12 finally shows the combined profile from all 12 simulated halos analogue to what was done for Ly$_\alpha$ and Mg II λ2796Å above. Like the individual profile already pointed to, the overall profile has the right shape but is at somewhat higher values than the observed EWs. This is again about 0.2 dex as for Ly$_\alpha$ (see subsection 5.2.4 and Fig. 5.11) and Mg II λ2796Å (see section 6.3 and Fig. 6.9) and also the H I when set into relation to the stellar masses (cf. Fig. 3.4).

Contrary to all simulations that I am aware of, however, my simulations do not under-predict but over-predict the O VI EWs and are closer to the observed values (+0.2 dex instead of −0.7 dex). For this agreement, it was also not necessary to artificially add large sub-resolution scale turbulent broadening as done by Oppenheimer & Davé (2009), Oppenheimer et al. (2012) (for O VI only) in order to match the observations. A plausible explanation is the multiphase hydrodynamics that somewhat counteracts the low resolution in the CGM, which also can explain the missing of extremely low EWs that would correspond to the non-detections of O VI.

6.5 Individual Lines and their Relations

I have shown that Ly$_\alpha$ lines are often too saturated to take information about the gas solely from them as the line width and shape arises from a degenerated mix of column density, temperature, and velocity structure. This then requires additional information which can almost only come from other lines. If one is not lucky enough to have other Lyman lines (Ly$_\beta$, Ly$_\gamma$, ...) that are not saturated, it requires metal

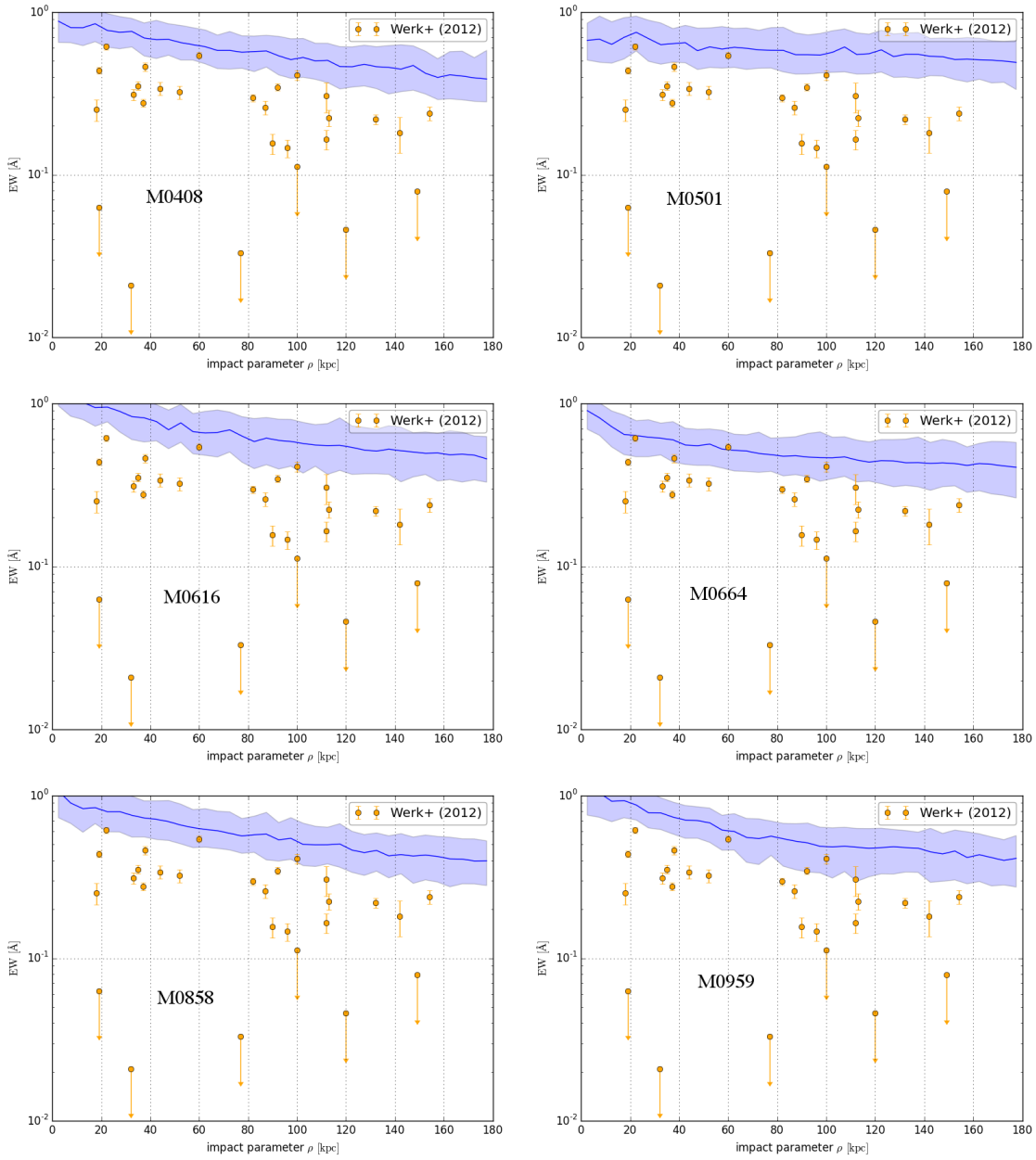

Figure 6.10: O VI λ1031Å EW profiles shown for halos M0408, M0501, M0616, M0664, M0858, and M0959 (from top left to bottom right) at redshift $z = 0.22$ as generated from many random orientations for each halo. The blue line is the median EW for each radial bin of 5 kpc width and the light-blue band indicated the 10%ile and 90%ile in these bins. For comparison the observations as presented in Werk et al. (2012) (restricted to $0.14 < z < 0.27$, median $z = 0.22$) are plotted in orange.

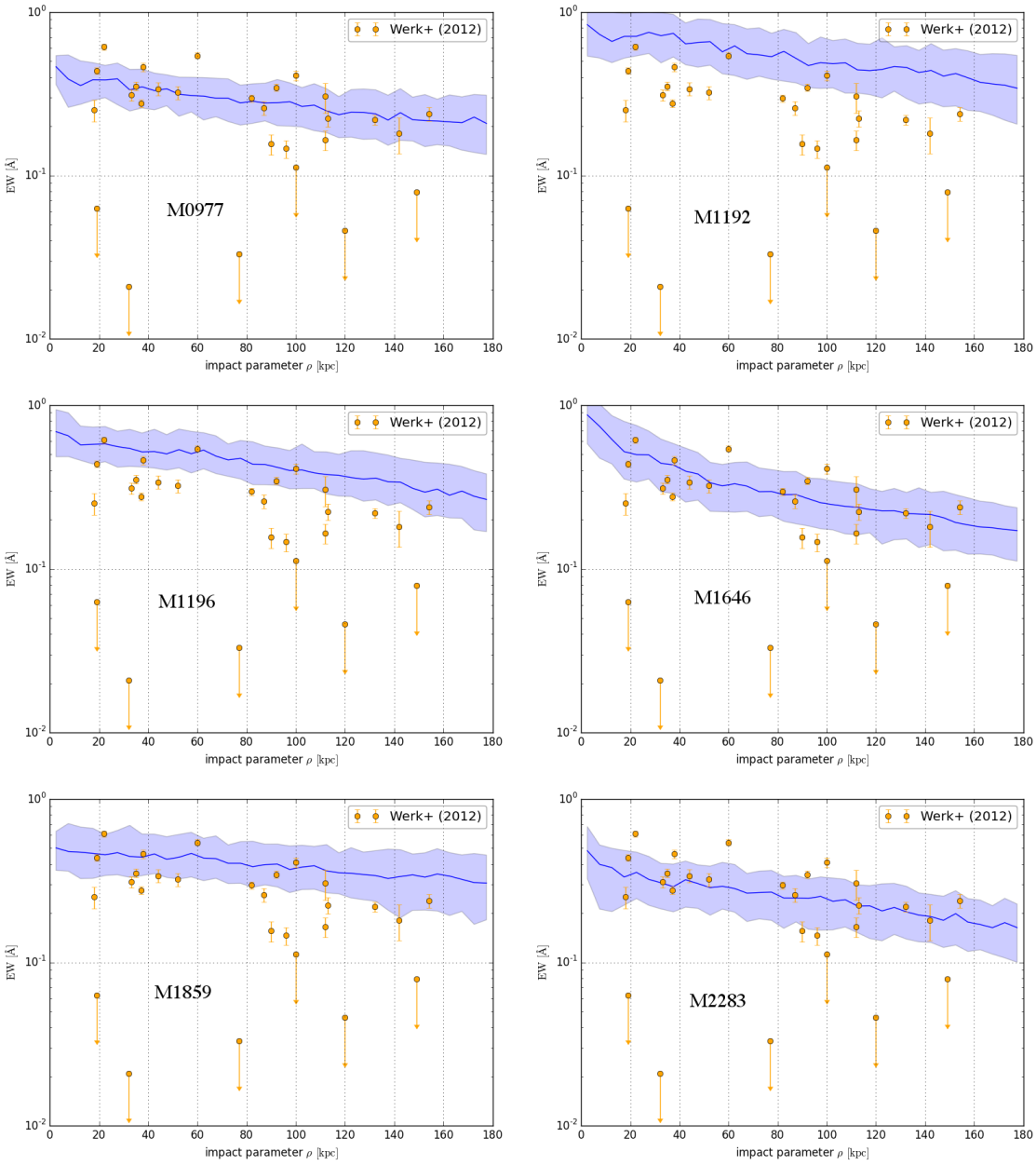

Figure 6.11: O VI λ1031Å EW profiles shown for halos M0977, M01192, M1196, M1646, M1859, and M2283 (from top left to bottom right) at redshift $z = 0.22$ as generated from many random orientations for each halo. The blue line is the median EW for each radial bin of 5 kpc width and the light-blue band indicated the 10%ile and 90%ile in these bins. For comparison the observations as presented in Werk et al. (2012) (restricted to $0.14 < z < 0.27$, median $z = 0.22$) are plotted in orange.

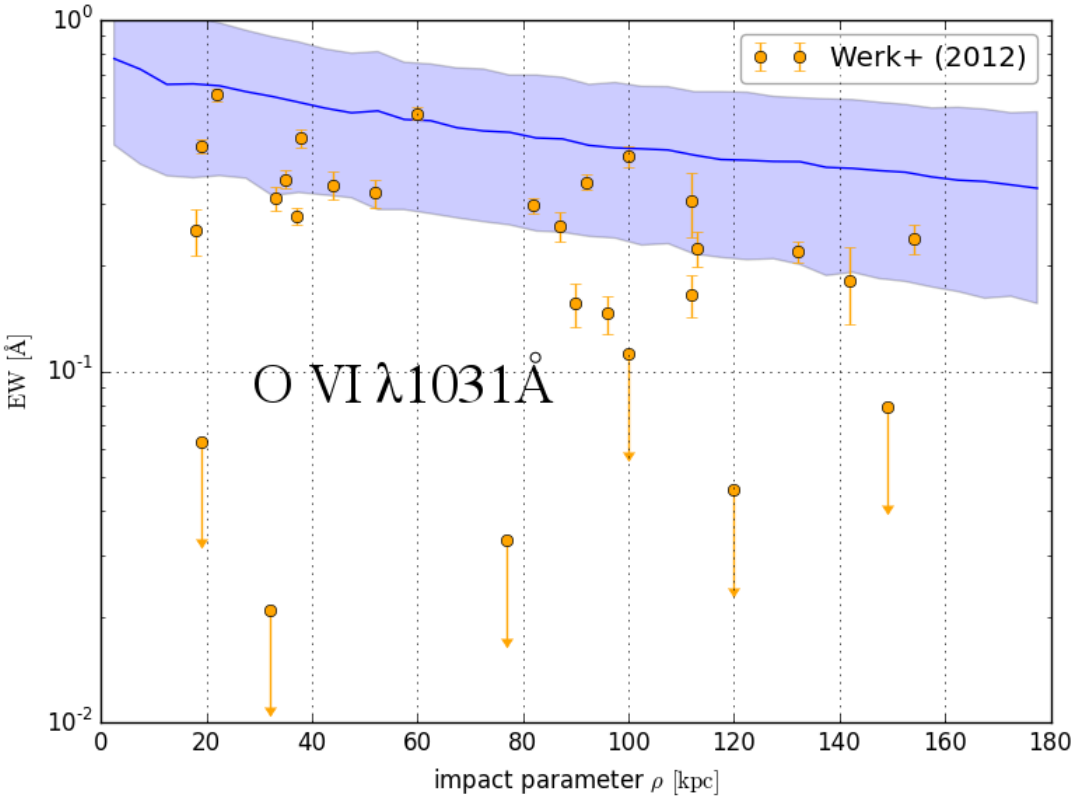

Figure 6.12: The combined O VI λ1031Å EW profile for all 12 simulations analogue to Fig. 6.9. For comparison the observations from Werk et al. (2012) (restricted to $0.14 < z < 0.27$) are again plotted in orange.

lines. However, different ions live in different parts in the density-temperature space and thus do not necessarily trace each other. A good tracer of H I, however, is Mg II as they occupy very similar density and temperature regimes (see Fig. 6.1). Higher ions have no (or very little) overlap with H I and Mg II. Hence, they trace very different gas. One can, therefore, expect their lines to be largely different from those of the lower ions. That is in terms of their shape and position in the spectrum, due to differences in the positions and distributions of the gas that give rise to the line itself.

In Fig. 6.13, I show one example sight-line from halo M0858 that was chosen to have most of the typical features. It is a line at an impact parameter of $\rho = 65\,\mathrm{kpc}$ in the same projection as the maps in Fig. 5.3 (right next to line #5), it has a H I column density of $1.5 \times 10^{16}\,\mathrm{cm}^{-2}$ and $EW_{\mathrm{Ly}\alpha} = 1.23\,\text{Å}$, i.e. well within the flat part of the curve of growth.

It shall be noted, that these lines have—in contrast to the rest of the line in this thesis—a sub-resolution scale turbulence of 10 km/s. This smoothed their spectra somewhat, but only marginally affected their EWs. It is not physically unsound to assume some unresolved turbulence for the gas particles of $\sim 7.4 \times 10^5\,M_\odot$ and smoothing lengths of order 20 kpc, justifying this measure.

In the upper panel, the spectra for Ly_α, Mg II λ2796 Å, Si III λ1206 Å, C IV λ1548 Å, and O VI λ1031 Å are plotted. The row below shows the column densities in velocity bins of 12 km/s width. Here, one can already see that Mg II indeed traces the H I gas as at each local maximum of the H I column densities (at ~ -40 km/s, $\sim$ 20 km/s, and $\sim$70 km/s) also Mg II has a local maximum. Since the column densities of Mg II are about two and a half order of magnitude smaller, the individual lines are resolved in the Mg II spectrum, even though they are not in the Ly_α spectrum.

Fitting the Ly_α line with three Voigt profiles at the positions of the Mg II lines is still improper, because the wings (at $\lesssim -180$ km/s and $\gtrsim 180$ km/s) might be mistaken as damping wings (especially when convolved with noise). They are, however, a result of small column densities at high velocities, which are improperly traced by Mg II as its column densities are too small—even the total H I column density of $1.5 \times 10^{16}\,\mathrm{cm}^{-2}$ is too small to exhibit damping wings. The Si III λ1206Å spectrum might help a bit as the Si III column densities are typically one order of magnitude larger than those of Mg II. The wings in Ly_α ($\gtrsim 180$ km/s) have still no correspondence, though.

Moving on to the spectra of the higher ions C IV and O VI, it can be noticed that they are broader than those of the low metal ions (Mg II and Si III), however, the O VI does not attenuate the flux as much as the other lines at all wavelengths. This can be attributed to the flat column density distribution in velocity space. Even

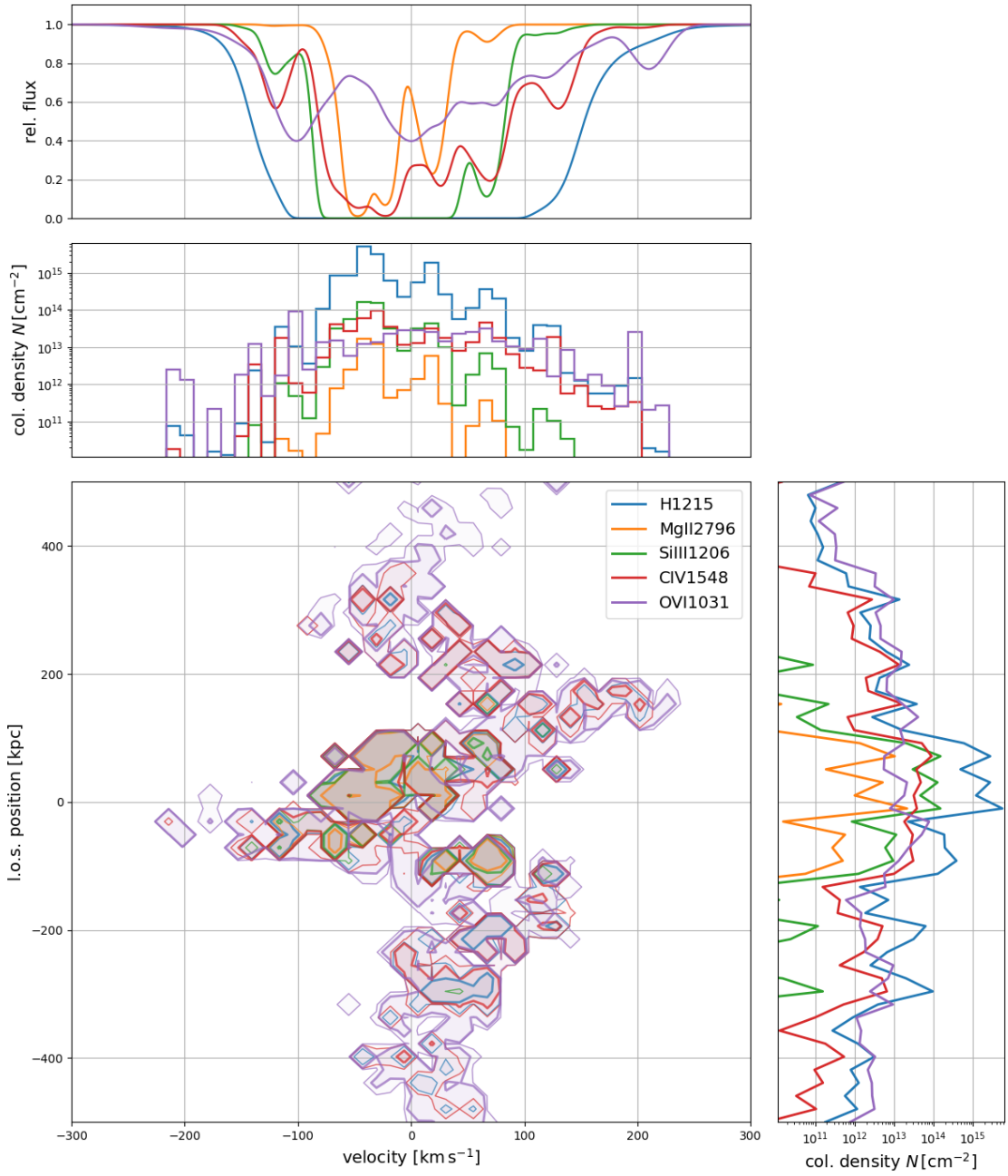

Figure 6.13: The top panel shows the spectra of Ly$_\alpha$, Mg II $\lambda = 2796$ Å, Si III $\lambda = 1206$ Å, C IV $\lambda = 1548$ Å, and O VI $\lambda = 1031$ Å for a l.o.s. at $(-42.7, 48.6)$ kpc in the same projection as in Fig. 5.3. The large panel at the bottom shows the column density distribution along the l.o.s. in position and velocity. The contours enclose 99% (thick lines) and 99.9% (thin lines) of the column density. The histograms to the top and to the right are created by projection and show the distributions in velocity space (underneath the spectra) and along the l.o.s..

though O VI occupies a totally different part of the phase-diagram, its spectrum has a line at $\sim 210\,\mathrm{km/s}$, indicating that there is some H I column density at these velocities that causes the damping wing-like edge in the Lyman-α spectrum. That the absorption of both lines also originates from gas at the same position can be seen in the large panel at the bottom.

The bottom left panel of Fig 6.13 shows the column density distribution of the gas of the different ions along the line of sight of the spectra plotted in the top panel (similar to what was done in e.g. Fig. 5.7). The histograms of the projections of this 2D distribution are plotted in the panels to the top (already discussed above) and to the right (the column density distribution along the line of sight). The only gas that has velocities close to $+200\,\mathrm{km/s}$ concentrates on a single physical position between 100 kpc and 200 kpc. This gas causes both, the small O VI line to the right and the damping wing-like edge of the Ly_α line. As O VI and H I live in totally distinct conditions in terms of density and temperature, the coexistence of such large amounts of these two ions at the same position is also partly (there are always very small fractions of H I in each particle) a feature of the multiphase hydrodynamic model of my simulations.

It can also be seen in the l.o.s. phase-space distribution of Fig 6.13 that O VI spreads widest in all directions, i.e. in l.o.s. position and l.o.s. velocity. It does not peak in the centre as H I, but its profile and velocity distribution are much flatter. Also C IV occupies most of the space O VI does, but spreads not quite as far. The low ions strongly peak in the centre position-wise, and also do not extend to large velocities. The reason for that is that further out from the galaxy into the CGM the temperatures rise and the densities drop, and hence we move from the low ions to the higher ionisation states in the phase-diagram (cf. Fig. 6.1).

Chapter 7

Summary

7.1 The Setting

In this thesis I presented a multiphase hydrodynamics SPH galaxy formation model with a two-phase feedback that was amongst the first ones that has proven to be successful in producing realistic spiral galaxies (Aumer et al., 2013). It is unique in its multiphase approach that was designed to represent the unresolved phases in the ISM, which is known to have at least a hot phase with a large volume filling factor and a dense, cold phase that can essentially move freely though the hot phase. The same context was the motivation to split the stellar feedback (the model does not include AGN feedback) into a 'hot' and a cold, dense phase. Here, in contrast to the multiphase hydrodynamics which is a continuum of phases, one had to introduce a threshold differentiating the 'hot' and the 'cold' phase ($< 8 \times 10^4\,\mathrm{K}$ and $> 4 \times 10^{-5}\,\mathrm{cm}^{-3}$). Another crucial building block for the model is the radiative pressure from massive stars that prevents the gas from forming too many stars early on in the cosmic history.

The original version had the mass and metal input into the ISM from AGB stars coupled with the feedback from SN type Ia with the argumentation that the energy input from AGB stars is negligible. This, however, pushed the metals from AGB stars with an initial velocity of 3000 km/s away from the location of production, letting their cooling act elsewhere. I decoupled the AGB winds from the SNe and gave them a more physical velocity of 30 km/s. This did not compromise the model's success, but often made the disc sizes smaller.

As there is little publicly available, powerful code out there for analysing SPH galaxy formation simulations[1], I developed my own Python framework for that pur-

[1]The only one found (PYNBODY) did not work well together with GADGET simulations.

pose, called PYGAD which consists of $\sim 25,000$ lines of code including 'docstring' documentation. It was written with usability in mind and is publicly available by now[2]. First and foremost, it serves as a modularised framework for loading and working with SPH galaxy formation simulations. It simplifies task as such as reading snapshots, masking them to any part of interest (such as a given temperature range), or calculating stellar luminosities and gas ion fractions (by using CLOUDY tables). This Python framework does not only save time in writing analysis scripts, sparing time for physical questions, but also reduces the probability of bugs considerably due to the proper re-usage of often-used parts of the code.

On top of this framework, PYGAD provides modules for many purposes. Amongst them are a simple phase-space friends-of-friends (FoF) finder, functions for calculating key properties such as virial radii and virial masses or effective luminosity radii, and a central part are binning and plotting routines that not only take SPH smoothing fully into account but also ensure to conserve the integrals of the binned quantities (such as total mass when binning density). This thesis, however, mainly builds on PYGAD's capability of generating mock QSO absorption spectra.

The spectra are generated on a particle-by-particle basis, i.e. combining the Voigt spectra of all the SPH particles along the chosen line of sight. This approach is much more suited to the multiphase hydrodynamics of the simulations than existing codes (such as SNAPEXBIN/SPECEXSNAP, see Davé et al., 2010, Oppenheimer & Davé, 2006) that first bin SPH quantities such as the ion density and temperature along the sightline. As phases of different temperatures can co-exist at the same location in the multiphase model, this would result in an in-appropriate averaging of the temperatures (and other gas properties) in the binning, preferentially towards high temperatures. If one would calculate the ion fractions for the averaged densities and temperatures on the l.o.s., this would result in very different fractions than what is obtained when doing this on a particle-by-particle basis (and hence, within the co-existing phases). Additionally, the temperatures affect the broadening in the Voigt profiles and thus the line shape and EW. Note, at this point, that most modern galaxy formation models for simulations effectively include a sort of multiphase hydrodynamics by the way they implement feedback from stars and AGNs as well as galactic winds. Hence, the considerations about the implementation are not solely a problem of the unique simulation model I use.

Finally, I conducted simulations with the multiphase model for a dozen of zoomed-in halos. They have present-day virial masses (actually M_{200}) in the range from $4 \times 10^{11}\,M_\odot$ to $3 \times 10^{12}\,M_\odot$. Their central galaxies have stellar masses of $7 \times 10^{9}\,M_\odot$

[2] PYGAD is open source and available as a git repository at `https://bitbucket.org/broett/pygad`.

to $1 \times 10^{11}\,M_\odot$ (for more details see Table 3.1) with which the simulations fall into the uncertainties of abundance matching results. The galaxies have high stellar disc-to-total mass ratios like the simulations by Aumer et al. (2013) and they are within the uncertainties for the observed H I mass to stellar mass ratios. This is with a slight tendency towards too much H I gas, though. I then applied the absorption spectra generation module of PYGAD to these simulations and investigated the results in itself and in comparison to observations.

7.2 Results on the Lyman-α Absorption in the CGM

In a first step I created mock Lyman-α spectra from the simulations with the absorption line generation module of PYGAD. I indeed found significant differences of the different approaches to generate spectra from the simulations (SPAGE: on a particle-by-particle basis; GriCAGE: binning along the l.o.s.) with their EWs often differing by up to 30%. Due to the aforementioned reasons (consistency with ionisation fraction calculation and multiphase SPH), I used the SPAGE approach throughout my work.

As a test of the models, I compared the simulated EW profiles with observations from Borthakur et al. (2015) at redshift zero. The agreement is generally fairly good as most observations can well be explained with the findings from the simulations. That is true independent of whether the impact parameter are taken physically or whether they are scaled to R_{200}. The scatter, however, is large and the median values of the simulations is about 0.2 dex higher than the observed ones. Furthermore, the lowest observed EWs are not frequent enough in the simulations.

The reason for the large simulated EWs can be attributed to the heavier galaxies as the normalisation of the Lyman-α EW profiles correlates with the stellar mass. Furthermore, Borthakur et al. (2015) found the EWs to also correlate with the H I disc size and the simulated galaxies have larger ones than the observational sample. That can explain the tension of the medians of the simulated and observed EWs. The smallest observed EWs might also be connected to the resolution in the CGM of the simulations. As the H I weighted smoothing lengths—and thus the spatial resolution—are typically of order $2 - 5\,\mathrm{kpc}$ and are seldom significantly smaller, it is possible that the H I distribution is more clumpy in the CGM than it can be resolved in the simulations. This would result in smaller covering fractions and, hence, in more very low EWs.

The simulations also open the possibility to compare the EW maps with the column densities for an entire projection of a halo and are not bound to the existence of an actual QSO in the background. Comparing these two maps at large scales

(around R_{200} and beyond), I find good agreement of them as the column densities and EWs are in the linear regime of the curve of growth. At smaller scales and in the CGM, however, the picture changes drastically and the correlation of EWs and column densities breaks down almost completely.

In the CGM, the column densities are typically in the flat part of the curve of growth, where the relation between column densities and EWs is not as strong as elsewhere and the temperatures broaden the lines via the now relevant b-parameter. Gas temperatures in the CGM anti-correlate with the densities as the gas roughly behaves adiabatically. This implies that with higher density, which generally increases the EW, the temperature usually drops, creasing the b-parameter and by that decreasing the EWs.

That alone, however, is not sufficient to explain the breakdown of the correlation of column densities and EWs. The velocity dispersion along a l.o.s. also vary between typically $\sim 10\,\mathrm{km/s}$ and $\sim 100\,\mathrm{km/s}$, also largely influencing the line shape and its EW. It cannot be simply added to the classical b-parameter (temperature broadening is also due to a Doppler shift by thermal motion), because the actual velocity distribution varies much from line to line. Nevertheless, there is a clear positive correlation between the velocity dispersion and the EW of the line. As a result, the EWs are a degenerated effect of column density, temperature, and velocity dispersion in the flat regime of the curve of growth. It is common practice to fit absorption lines with Voigt profiles. As the column density is in general distributed very irregularly over the velocities and not concentrated in cloudlets at a few given positions, these fits are not appropriate. Some lines even have damping wing like features that are, in fact, caused by small column densities.

Although the EWs are only very weakly correlated with the column densities and the velocity structure in the CGM largely destroys it, some halos show a dependence of the EWs with the azimuthal angle of the l.o.s. that originates from a structure in the column densities. This is true for about half (three out of seven) of the currently not merging simulations. These had no recent merger that disturbed the CGM and have a 'smooth' halo gas, i.e. no significant structure in their l.o.s. velocity dispersion maps. For these galaxies, the H I column densities are elevated in the plane of the disc, where gas accretes onto the galaxies' gas disc. This angular dependence of the column densities is mimicked in the EWs as the velocity structures is relatively smooth. The other half of the non-merging galaxies had either no angular dependence in the column densities or it was destroyed by the velocity structure (both typically are an aftermath of a long-ago major merger or fly-bys). Only in one case (out of seven) there was a slight dependence opposite to the one in the galaxies with a 'smooth' halo.

Finally, I compared the findings of one halo with one simulation[3] of the same halo at higher resolution and one with weak feedback. The higher resolution simulation was remarkably similar (cf. Scannapieco et al., 2012) to the reference simulation in almost all matters, which includes the EWs map and the correlation of the EWs with column density, temperature, and velocity dispersion. The weak feedback simulations had very low column densities as the weak feedback did not eject much gas from the galaxy (in comparison to the reference model). As a result most of the sight-lines in the CGM were in the linear part of the curve of growth. However, some were at high enough column densities to enter the flat regime and I also found the velocity dispersion to have a major impact on the column densities in the fashion it has in the reference simulation.

7.3 Results on Metal Ions and Lines in the CGM

Since different ions trace different phases of the CGM, I find them also to trace in- and outflows to different extent. Low ions and H I very seldom are outflowing at all radii: from radii of 20 kpc to 300 kpc less than 10% of H I are outflowing. Typically, large fractions of the low ions and H I are inflowing with radial velocities of less than -50 km/s from about 50 kpc on outward. Higher ions have both, inflowing and outflowing fractions, to a significant extent and the 'static' fraction ($|v_{\rm rad}| < 50$ km/s) usually is the largest. For the instance of O VI the 'static' fraction increases from about 30% at 50 kpc to more than 50% at 300 kpc. The outflowing component, however, dominates over the other two components for radii $\lesssim 100$ kpc and often 10% of the O VI has radial velocities larger than the escape velocity, whereas this is usually true for only $\sim$1% of the total gas.

The different ions and H I do not only largely differ in their velocity structure, but also are spatially distributed differently. So are the higher ions (as C IV and O VI) much more evenly distributed in the halo, not tracing the dense (and cold) structures. Owed to the temperatures in the CGM and beyond R_{200} as well as the fact that I find $\sim$50% of the metals within $2R_{200}$ at radii larger than R_{200}, the profiles for these ions extend almost flat well beyond the virial radius. The lower ions and H I are much more concentrated towards the center of the halo, and in the CGM they preferentially live in cold dense substructures. Although, Mg II extents further into low density structures than H I does, they trace each other fairly well, which can become handy when analysing observed, saturated Lyman-α lines.

The absorption spectra by Mg II are found to be mirrored by much stronger

[3]Restrictions in the code prevented me from simulating all halos at higher resolution.

absorption from H I. This can help to disentangle the contribution of density and temperature to the EWs from those of Doppler shifts from gas motion of the saturated Lyman-α lines (especially if no higher Lyman lines are observed). The limitation of that approach, however, is that at lower column densities, where there is still significant absorption from H I, the flux is almost not attenuated at the Mg II lines. This can be particularly important in weak wings in the Lyman-α lines that could be misinterpreted as damping wings. Here, the column densities in Mg II are too low to cause significant absorption. The high ions like C IV and O VI do not reach as high column densities as H I and do not produce saturated lines in the CGM. However, they are distributed much more uniformly, causing significant absorption far beyond the virial radius. As those ions also trace the heated galactic outflows that tend to have larger velocities than the H I and low ion gas, the line of e.g. O VI can be wider than the saturated Lyman-α spectrum of the same l.o.s..

Both, for the studied Mg II λ2796Å and the O VI λ1031Å lines, the agreement of their EW profiles to observations is similarly good as the one of Ly_α (for Mg II λ2796Å even somewhat better). Both over-predict the median EWs by about 0.2 dex, but follow the observed profiles' shape well and most observed data points are within the middle 80%ile. Again, the simulations have difficulties explaining the lowest EWs, which could improve with better resolution. To my knowledge this is the best agreement in O VI for all simulations done up to date without having to artificially add sub-resolution turbulence. Typically, simulations under-predict the O VI column densities by about 0.7 dex and never over-predict them. As the multiphase hydrodynamic models allows for the coexistence of hot and cold phases (also in the CGM, see Appendix A), this might be the key in getting the O VI column densities next to the others right.

Appendix A

Large Smoothing Lengths in the Cold Phase

A often raised concern about the multiphase model in context of the two-phase feedback is the cold phase (in the sense of subsection 3.3.1) can have large smoothing lengths than span the entire galaxy. That would let cold gas from one end of the galaxy communicate hydrodynamically with gas from the other end, which is obviously unphysical. This concern is fuelled by the histogram in Fig. A.1, showing the amount of particles with given smoothing lengths in the halo (within R_{200}). And indeed, most particles in the cold phase ($T < 8 \times 10^4\, K$ and $n > 4 \times 10^{-5}\,\mathrm{cm}^{-3}$) have smoothing lengths larger than 4 kpc.

However, the cold particles with large smoothing lengths ($> 4\,\mathrm{kpc}$) are not located in the ISM as Fig. A.2 shows. In fact, the region of the disc is less populated by these particles than the rest of the CGM, despite that most mass is located in the disc. Particle of the cold phase with large smoothing lengths are where there are denser structures in the CGM. It shall also be mentioned that for other halos, the amount of cold dense gas in the CGM is often less than for M0858 and, hence, the shaded reagion of Fig. A.2, i.e. the amount of 'cold' particles with large smoothing lengths decreases with respect to M0858, too.

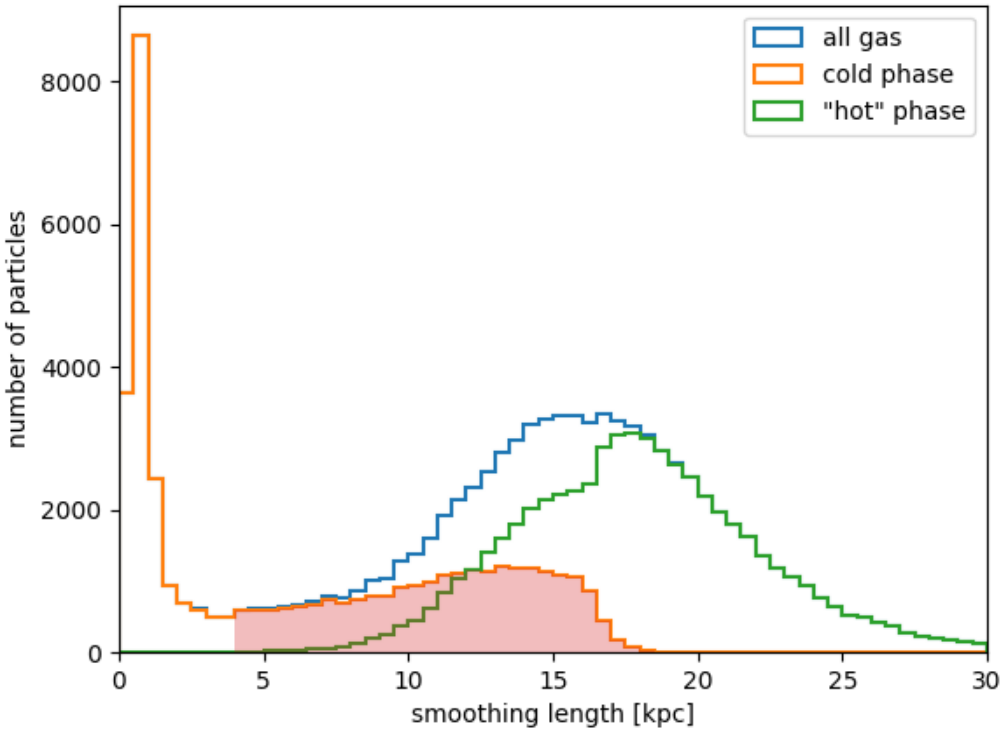

Figure A.1: Smoothing length distribution in the halo (within R_{200}) M0858. The blue histogram shows the smoothing lengths of all gas particles, the orange histogram those of the cold phase in the sense of subsection 3.3.1, and the green one from the remaining gas, which is referred to as the 'hot phase'. The red shaded region is cold gas with smoothing lengths larger than 4 kpc (cf. Fig. A.2).

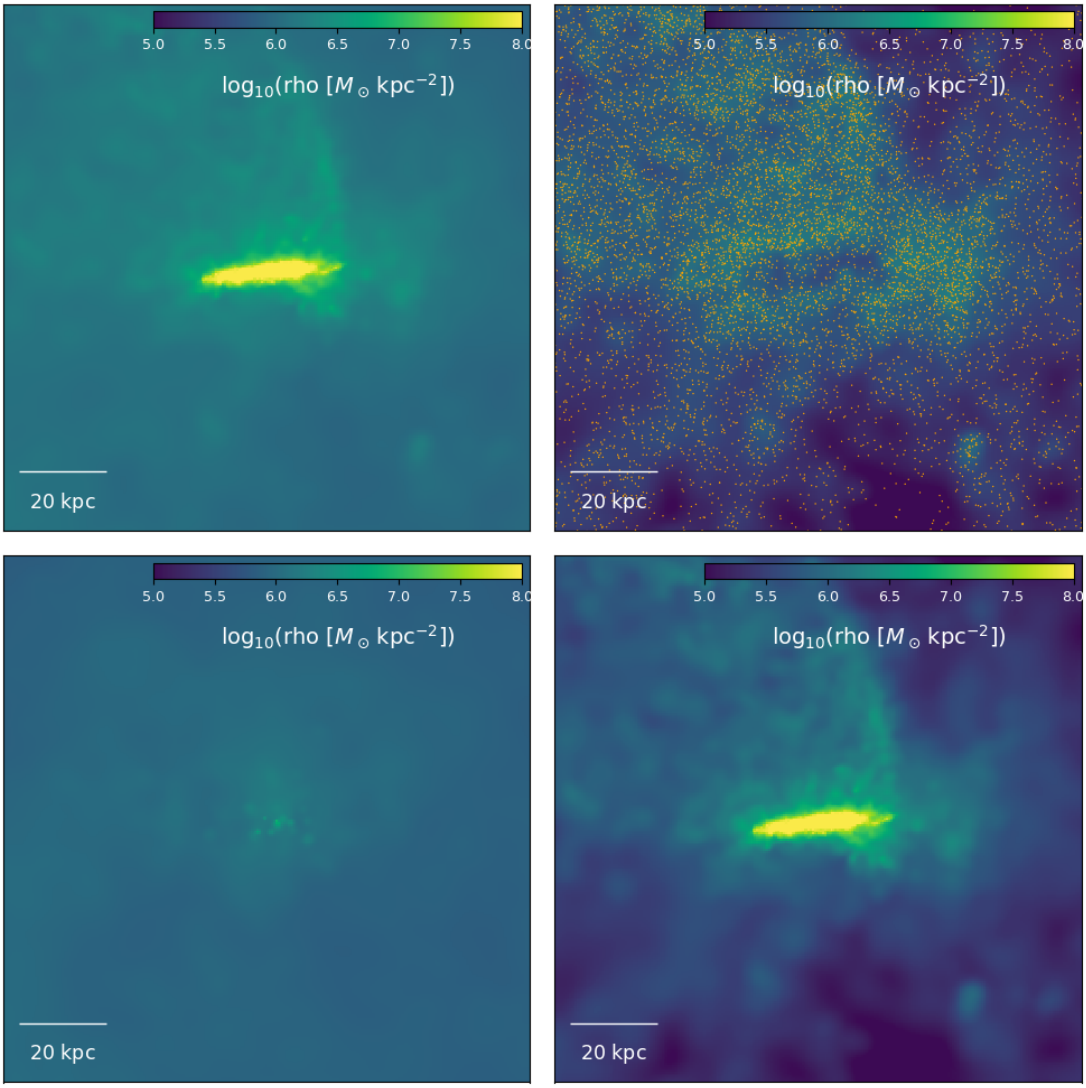

Figure A.2: The column density maps of halo M0858 with a side length of the panels of 120 kpc in a side-on projection of the gas disc. The upper left panel shows all gas, the bottom left panel just the gas in the 'hot' phase, the bottom right panel all gas in the cold phase, and the upper right panel, finally, the gas in the cold phase with smoothing lengths larger than 4 kpc (cf. Fig. A.1). The latter panel has the positions of the particles overplotted by orange points. The hot and cold phase shall be understood in the sense of subsection 3.3.1.

Appendix B

Phase Space Distribution for Chosen Lines

Fig.B.1 shows the phase-space distribution of the H I along the l.o.s. of the marked ones in Fig. 5.3 analogue to Fig. 5.7. The spectra of these sight lines are presented in 5.6, Fig. 4.3, and 5.5.

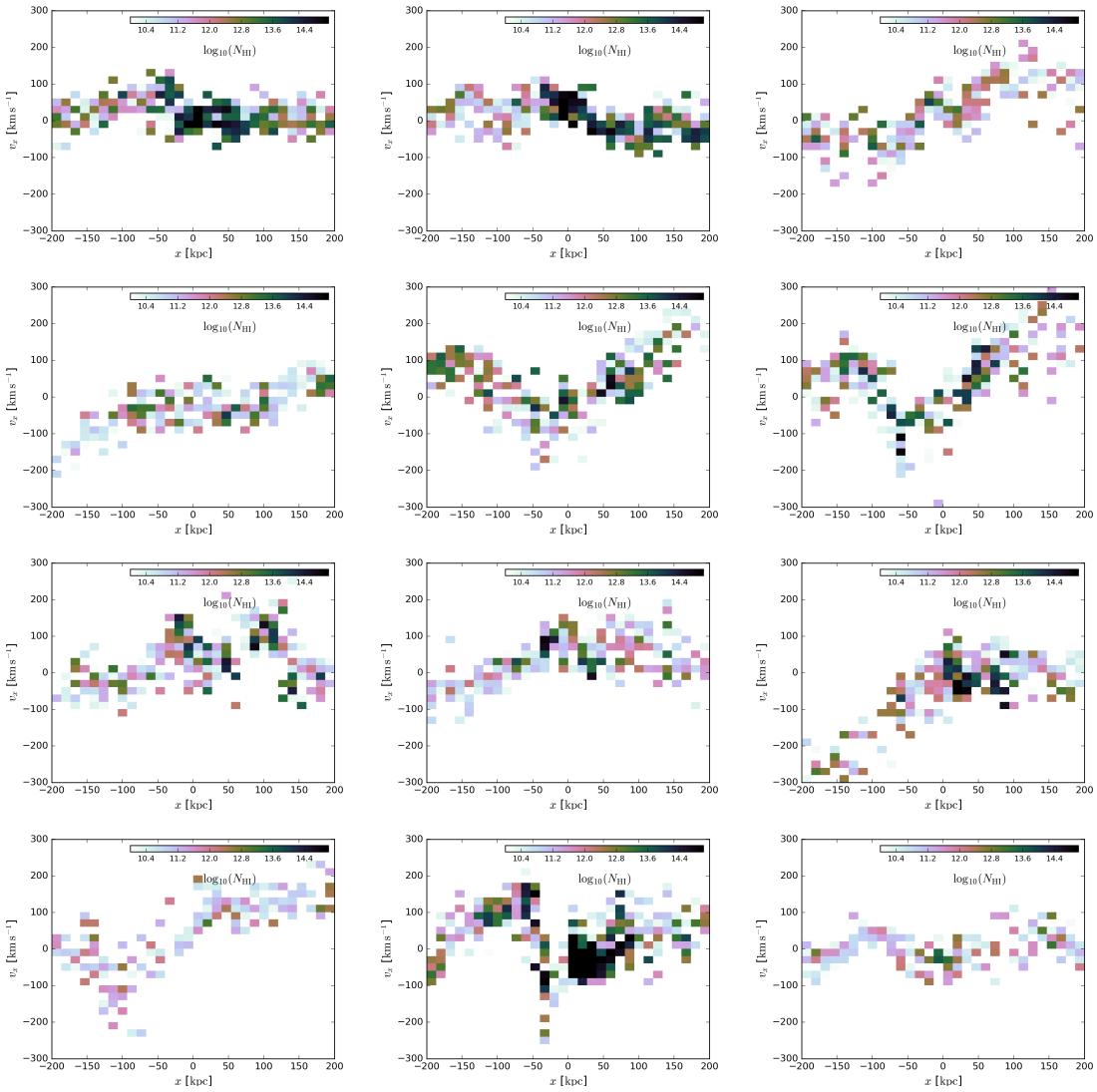

Figure B.1: Similar to Fig. 5.7 we show the column density distribution along the lines of sight and as a function of its velocity and l.o.s. position. Colour coded is the amount of column density in each pixel. Shown are the distribution of all 12 lines that are marked in Fig. 5.3 with their spectra shown in 5.6, Fig. 4.3, and 5.5. The panels are ordered by line numbers in western reading order, i.e. from top left to bottom right.

Bibliography

Abadi M. G., Navarro J. F., Steinmetz M., Eke V. R., 2003, ApJ, 597, 21

Abel T., 2011, MNRAS, 413, 271

Agertz O., et al., 2007, MNRAS, 380, 963

Agertz O., Teyssier R., Moore B., 2011, MNRAS, 410, 1391

Aumer M., White S. D. M., Naab T., Scannapieco C., 2013, MNRAS, 434, 3142

Aumer M., White S. D. M., Naab T., 2014, MNRAS, 441, 3679

Bailin J., Steinmetz M., 2005, ApJ, 627, 647

Bauer A., Springel V., 2012, MNRAS, 423, 2558

Behroozi P. S., Wechsler R. H., Conroy C., 2013, ApJ, 770, 57

Bennett C. L., et al., 2013, ApJS, 208, 20

Bordoloi R., et al., 2011, ApJ, 743, 10

Borland D., Ii R. M. T., 2007, IEEE computer graphics and applications, 27

Borthakur S., et al., 2015, ApJ, 813, 46

Bouché N., Hohensee W., Vargas R., Kacprzak G. G., Martin C. L., Cooke J., Churchill C. W., 2012, MNRAS, 426, 801

Bowen D. V., Blades J. C., Pettini M., 1995, ApJ, 448, 634

Buneman O., 1973, Journal of Computational Physics, 11, 250

Cappellari M., 2016, ARA&A, 54, 597

Cardelli J. A., Federman S. R., 1997, Nuclear Physics A, 621, 31

Catinella B., et al., 2010, MNRAS, 403, 683

Cen R., Fang T., 2006, ApJ, 650, 573

Cen R., Ostriker J. P., 1999, ApJ, 514, 1

Chen H.-W., Mulchaey J. S., 2009, ApJ, 701, 1219

Chieffi A., Limongi M., 2004, ApJ, 608, 405

Christensen C. R., Davé R., Governato F., Pontzen A., Brooks A., Munshi F., Quinn T., Wadsley J., 2016, ApJ, 824, 57

Churchill C. W., Steidel C. C., Vogt S. S., 1996, ApJ, 471, 164

Churchill C. W., Vander Vliet J. R., Trujillo-Gomez S., Kacprzak G. G., Klypin A., 2015, ApJ, 802, 10

Crain R. A., et al., 2017, MNRAS, 464, 4204

Crighton N. H. M., et al., 2011, MNRAS, 414, 28

Croton D. J., et al., 2006, MNRAS, 365, 11

Curtis H. D., 1988, PASP, 100, 6

Danforth C. W., Shull J. M., 2008, ApJ, 679, 194

Davé R., et al., 2001, ApJ, 552, 473

Davé R., Oppenheimer B. D., Katz N., Kollmeier J. A., Weinberg D. H., 2010, MNRAS, 408, 2051

Davé R., Katz N., Oppenheimer B. D., Kollmeier J. A., Weinberg D. H., 2013, MNRAS, 434, 2645

Davé R., Thompson R., Hopkins P. F., 2016, MNRAS, 462, 3265

Dekel A., Silk J., 1986, ApJ, 303, 39

Dolag K., Reinecke M., Gheller C., Imboden S., 2008, New Journal of Physics, 10, 125006

Faber S. M., et al., 2007, ApJ, 665, 265

Fall S. M., Efstathiou G., 1980, MNRAS, 193, 189

Fan X., et al., 2006, AJ, 132, 117

Ferland G. J., Korista K. T., Verner D. A., Ferguson J. W., Kingdon J. B., Verner E. M., 1998, PASP, 110, 761

Ferland G. J., et al., 2013, Rev. Mex. Astron. Astrofis., 49, 137

Ford A. B., et al., 2016, MNRAS, 459, 1745

Friedman A., 1999, General Relativity and Gravitation, 31, 31

Galilei G., 1610, Sidereus nuncius magna, longeque admirabilia spectacula pandens lunae facie, fixis innumeris, lacteo circulo, stellis nebulosis, ... Galileo Galileo : nuper a se reperti beneficio sunt observata in apprime vero in quatuor planetis circa Iovis stellam disparibus intervallis, atque periodis, celeritate mirabili circumvolutis ... atque Medicea sidera nuncupandos decrevit, doi:10.3931/e-rara-695.

Gatto A., et al., 2015, MNRAS, 449, 1057

Gerhard O. E., 1983, MNRAS, 202, 1159

Gingold R. A., Monaghan J. J., 1977, MNRAS, 181, 375

Girardi L., et al., 2010, ApJ, 724, 1030

Greif T. H., Glover S. C. O., Bromm V., Klessen R. S., 2009, MNRAS, 392, 1381

Guedes J., Callegari S., Madau P., Mayer L., 2011, ApJ, 742, 76

Gutcke T. A., Stinson G. S., Macciò A. V., Wang L., Dutton A. A., 2017, MNRAS, 464, 2796

Haardt F., Madau P., 2001, in Neumann D. M., Tran J. T. V., eds, Clusters of Galaxies and the High Redshift Universe Observed in X-rays. p. 64 (`arXiv:astro-ph/0106018`)

Haehnelt M. G., Steinmetz M., Rauch M., 1998, ApJ, 495, 647

Hafen Z., et al., 2016, preprint, (`arXiv:1608.05712`)

Hockney R. W., Eastwood J. W., 1981, Computer Simulation Using Particles

Hopkins P. F., 2013, MNRAS, 428, 2840

Hopkins P. F., 2014, GIZMO: Multi-method magneto-hydrodynamics+gravity code, Astrophysics Source Code Library (ascl:1410.003)

Hopkins P. F., 2015, MNRAS, 450, 53

Hopkins P. F., Quataert E., Murray N., 2011, MNRAS, 417, 950

Hu C.-Y., Naab T., Walch S., Moster B. P., Oser L., 2014, MNRAS, 443, 1173

Hubble E. P., 1926, ApJ, 64

Hubble E., 1929a, Proceedings of the National Academy of Science, 15, 168

Hubble E. P., 1929b, ApJ, 69

Hui L., Gnedin N. Y., 1997, MNRAS, 292, 27

Hummels C. B., Bryan G. L., Smith B. D., Turk M. J., 2013, MNRAS, 430, 1548

Ivezić Ž., et al., 2008, ApJ, 684, 287

Iwamoto K., Brachwitz F., Nomoto K., Kishimoto N., Umeda H., Hix W. R., Thielemann F.-K., 1999, ApJS, 125, 439

Kacprzak G. G., Churchill C. W., Nielsen N. M., 2012, ApJL, 760, L7

Kacprzak G. G., Muzahid S., Churchill C. W., Nielsen N. M., Charlton J. C., 2015, ApJ, 815, 22

Karachentsev I. D., Karachentseva V. E., Huchtmeier W. K., Makarov D. I., 2004, AJ, 127, 2031

Karakas A. I., 2010, MNRAS, 403, 1413

Katz N., 1992, ApJ, 391, 502

Kennicutt Jr. R. C., 1998, ApJ, 498, 541

Kepple G., 1998, The night sky observers guide. Willmann-Bell, Richmond, Va

Kravtsov A., Vikhlinin A., Meshscheryakov A., 2014, preprint, (`arXiv:1401.7329`)

Kroupa P., 2001, MNRAS, 322, 231

Lanzetta K. M., Wolfe A. M., Turnshek D. A., Lu L., McMahon R. G., Hazard C., 1991, ApJS, 77, 1

Lanzetta K. M., Bowen D. V., Tytler D., Webb J. K., 1995, ApJ, 442, 538

Larson R. B., 1974, MNRAS, 169, 229

Liang C. J., Chen H.-W., 2014, MNRAS, 445, 2061

Licquia T., Newman J., 2013, in American Astronomical Society Meeting Abstracts #221. p. 254.11

Lucy L. B., 1977, AJ, 82, 1013

Lynds R., 1971, ApJL, 164, L73

Maller A. H., Bullock J. S., 2004, MNRAS, 355, 694

Marigo P., Girardi L., Bressan A., Groenewegen M. A. T., Silva L., Granato G. L., 2008, A&A, 482, 883

Marri S., White S. D. M., 2003, MNRAS, 345, 561

Mathes N. L., Churchill C. W., Kacprzak G. G., Nielsen N. M., Trujillo-Gomez S., Charlton J., Muzahid S., 2014, ApJ, 792, 128

Mo H. J., Miralda-Escude J., 1996, ApJ, 469, 589

Mo H., van den Bosch F. C., White S., 2010, Galaxy Formation and Evolution

Monaghan J. J., 1997, Journal of Computational Physics, 136, 298

Morris J. P., 1996, Publications Astronomical Society of Australia, 13, 97

Moster B. P., Macciò A. V., Somerville R. S., Naab T., Cox T. J., 2011, MNRAS, 415, 3750

Moster B. P., Naab T., White S. D. M., 2013, MNRAS, 428, 3121

Naab T., Ostriker J. P., 2016, preprint, (`arXiv:1612.06891`)

Navarro J. F., Benz W., 1991, ApJ, 380, 320

Navarro J. F., Frenk C. S., White S. D. M., 1995, MNRAS, 275, 56

Nestor D. B., Turnshek D. A., Rao S. M., 2005, ApJ, 628, 637

Nielsen N. M., Churchill C. W., Kacprzak G. G., Murphy M. T., 2013a, ApJ, 776, 114

Nielsen N. M., Churchill C. W., Kacprzak G. G., 2013b, ApJ, 776, 115

Nielsen N. M., Churchill C. W., Kacprzak G. G., Murphy M. T., Evans J. L., 2015, ApJ, 812, 83

Nielsen N. M., Kacprzak G. G., Muzahid S., Churchill C. W., Murphy M. T., Charlton J. C., 2017, ApJ, 834, 148

Norberg P., et al., 2002, MNRAS, 336, 907

Noterdaeme P., et al., 2012, A&A, 547, L1

Nulsen P. E. J., Barcons X., Fabian A. C., 1998, MNRAS, 301, 168

Öpik E., 1922, ApJ, 55

Oppenheimer B. D., Davé R., 2006, MNRAS, 373, 1265

Oppenheimer B. D., Davé R., 2009, MNRAS, 395, 1875

Oppenheimer B. D., Davé R., Kereš D., Fardal M., Katz N., Kollmeier J. A., Weinberg D. H., 2010, MNRAS, 406, 2325

Oppenheimer B. D., Davé R., Katz N., Kollmeier J. A., Weinberg D. H., 2012, MNRAS, 420, 829

Oppenheimer B. D., et al., 2016, MNRAS, 460, 2157

Oser L., Ostriker J. P., Naab T., Johansson P. H., Burkert A., 2010, ApJ, 725, 2312

Oser L., Naab T., Ostriker J. P., Johansson P. H., 2012, ApJ, 744, 63

Peebles P. J. E., 1980, The large-scale structure of the universe

Peeples M. S., Werk J. K., Tumlinson J., Oppenheimer B. D., Prochaska J. X., Katz N., Weinberg D. H., 2014, ApJ, 786, 54

Piontek F., Steinmetz M., 2011, MNRAS, 410, 2625

Planck Collaboration et al., 2016, A&A, 594, A1

Portinari L., Chiosi C., Bressan A., 1998, A&A, 334, 505

Power C., Navarro J. F., Jenkins A., Frenk C. S., White S. D. M., Springel V., Stadel J., Quinn T., 2003, MNRAS, 338, 14

Press W. H., Schechter P., 1974, ApJ, 187, 425

Price D. J., 2008, Journal of Computational Physics, 227, 10040

Price D. J., 2011, SPLASH: An Interactive Visualization Tool for Smoothed Particle Hydrodynamics Simulations, Astrophysics Source Code Library (ascl:1103.004)

Price D. J., 2012, Journal of Computational Physics, 231, 759

Price D. J., Federrath C., 2010, MNRAS, 406, 1659

Prochaska J. X., Wolfe A. M., 1997, ApJ, 487, 73

Prochaska J. X., Wolfe A. M., 1998, ApJ, 507, 113

Prochaska J. X., Weiner B., Chen H.-W., Mulchaey J., Cooksey K., 2011, ApJ, 740, 91

Prochaska J. X., et al., 2017, ApJ, 837, 169

Rahmati A., Pawlik A. H., Raicevic M., Schaye J., 2013, MNRAS, 430, 2427

Rahmati A., Schaye J., Crain R. A., Oppenheimer B. D., Schaller M., Theuns T., 2016, MNRAS, 459, 310

Read J. I., Hayfield T., 2012, MNRAS, 422, 3037

Read J. I., Hayfield T., Agertz O., 2010, MNRAS, 405, 1513

Reed D. S., Bower R., Frenk C. S., Jenkins A., Theuns T., 2007, MNRAS, 374, 2

Röttgers B., 2017, Astrophysics Source Code Library, record ascl:yymm.xxx

Sargent W. L. W., Steidel C. C., Boksenberg A., 1989, ApJS, 69, 703

Scannapieco C., Tissera P. B., White S. D. M., Springel V., 2005, MNRAS, 364, 552

Scannapieco C., Tissera P. B., White S. D. M., Springel V., 2006, MNRAS, 371, 1125

Scannapieco C., White S. D. M., Springel V., Tissera P. B., 2009, MNRAS, 396, 696

Scannapieco C., et al., 2012, MNRAS, 423, 1726

Schaye J., 2001, ApJ, 559, 507

Schaye J., Carswell R. F., Kim T.-S., 2007, MNRAS, 379, 1169

Schaye J., Crain R. A., Bower R. G. e. a., 2015, MNRAS, 446, 521

Schechter P., 1976, ApJ, 203, 297

Schmidt M., 1959, ApJ, 129, 243

Shen S., Wadsley J., Stinson G., 2010, MNRAS, 407, 1581

Simcoe R. A., Sargent W. L. W., Rauch M., Becker G., 2006, ApJ, 637, 648

Slipher V. M., 1913, Lowell Observatory Bulletin, 2, 56

Slipher V. M., 1915, Popular Astronomy, 23, 21

Somerville R. S., Davé R., 2015, ARA&A, 53, 51

Spergel D. N., et al., 2007, ApJS, 170, 377

Springel V., 2005, MNRAS, 364, 1105

Springel V., 2011, in Alves J., Elmegreen B. G., Girart J. M., Trimble V., eds, IAU Symposium Vol. 270, Computational Star Formation. pp 203–206, doi:10.1017/S1743921311000378

Springel V., Hernquist L., 2002, MNRAS, 333, 649

Steidel C. C., 1995, in Meylan G., ed., QSO Absorption Lines. p. 139 (arXiv:astro-ph/9509098)

Stern J., Hennawi J. F., Prochaska J. X., Werk J. K., 2016, ApJ, 830, 87

Stocke J. T., Penton S. V., Danforth C. W., Shull J. M., Tumlinson J., McLin K. M., 2006, ApJ, 641, 217

Stocke J. T., Keeney B. A., Danforth C. W., Shull J. M., Froning C. S., Green J. C., Penton S. V., Savage B. D., 2013, ApJ, 763, 148

Storrie-Lombardi L. J., McMahon R. G., Irwin M. J., 1996, MNRAS, 283, L79

Suresh J., Rubin K. H. R., Kannan R., Werk J. K., Hernquist L., Vogelsberger M., 2015, preprint, (arXiv:1511.00687)

Theuns T., Leonard A., Efstathiou G., Pearce F. R., Thomas P. A., 1998, MNRAS, 301, 478

Thom C., Chen H.-W., 2008, ApJS, 179, 37

Thom C., Werk J. K., Tumlinson J., Prochaska J. X., Meiring J. D., Tripp T. M., Sembach K. R., 2011, ApJ, 736, 1

Tremonti C. A., et al., 2004, ApJ, 613, 898

Tripp T. M., Bowen D. V., 2005, in Williams P., Shu C.-G., Menard B., eds, IAU Colloq. 199: Probing Galaxies through Quasar Absorption Lines. pp 5–23 (arXiv:astro-ph/0510312), doi:10.1017/S1743921305002395

Tripp T. M., Sembach K. R., Bowen D. V., Savage B. D., Jenkins E. B., Lehner N., Richter P., 2008, ApJS, 177, 39

Tumlinson J., et al., 2011, Science, 334, 948

Tumlinson J., et al., 2013, ApJ, 777, 59

Übler H., Naab T., Oser L., Aumer M., Sales L. V., White S. D. M., 2014, MNRAS, 443, 2092

Vogelsberger M., Genel S., Springel V. e. a., 2014, MNRAS, 444, 1518

Wadsley J. W., Veeravalli G., Couchman H. M. P., 2008, MNRAS, 387, 427

Wakker B. P., Savage B. D., 2009, ApJS, 182, 378

Walch S., et al., 2015, MNRAS, 454, 238

Wang J., et al., 2014, MNRAS, 441, 2159

Wang L., Dutton A. A., Stinson G. S., Macciò A. V., Gutcke T., Kang X., 2017, MNRAS,

Weil M. L., Eke V. R., Efstathiou G., 1998, MNRAS, 300, 773

Weinberg D. H., Miralda-Escudé J., Hernquist L., Katz N., 1997, ApJ, 490, 564

Werk J. K., Prochaska J. X., Thom C., Tumlinson J., Tripp T. M., O'Meara J. M., Meiring J. D., 2012, ApJS, 198, 3

Werk J. K., et al., 2014, ApJ, 792, 8

Werk J. K., et al., 2016, ApJ, 833, 54

White S. D. M., Rees M. J., 1978, MNRAS, 183, 341

Wiersma R. P. C., Schaye J., Smith B. D., 2009, MNRAS, 393, 99

Willman B., Strader J., 2012, AJ, 144, 76

Wilman R. J., Morris S. L., Jannuzi B. T., Davé R., Shone A. M., 2007, MNRAS, 375, 735

Woitke P., 2006, A&A, 452, 537

Wolfe A. M., 1988, in Blades J. C., Turnshek D. A., Norman C. A., eds, QSO Absorption Lines: Probing the Universe. p. 297

Wolfe A. M., Lanzetta K. M., Foltz C. B., Chaffee F. H., 1995, ApJ, 454, 698

Wright T., 1750, An original theory or new hypothesis of the universe : founded upon general phaenomena of the visible creation; and particularly the Via the laws of nature, and solving by mathematical principles : the Lactea ...compris'd in nine familiar letters from the author to his friendand : illustrated with upward of thirty graven and mezzotinto plates ..., doi:10.3931/e-rara-28672.

Zheng Y., Putman M. E., Peek J. E. G., Joung M. R., 2015, ApJ, 807, 103

de Vaucouleurs G., 1974, in Shakeshaft J. R., ed., IAU Symposium Vol. 58, The Formation and Dynamics of Galaxies. pp 1–52

Acknowledgements

First, I want to thank Prof. Dr. Simon M. D. White and the Max Planck Institute for Astrophysics for providing me the platform to persue my Ph.D. research. I thank Prof. Dr. Simon M. D. White and my supervisor Dr. Thorsten Naab for their support. I also thank Dr. Thorsten Naab, who allowed me to do exciting and educational research visits, gave me much intellectual freedom, and pushed me to use precise language.

Special thanks go to my family and in particular my girlfriend Johanna, who supported me, especially in the last and stressful weeks of my thesis.